UNSW
AUSTRALIA

INVESTIGATION OF SPOTTING AND INTRINSIC FIRE DYNAMICS USING A COUPLED ATMOSPHERE-FIRE MODELLING FRAMEWORK

A thesis submitted for the degree of

Doctor of Philosophy

By

Christopher Maurice Thomas

School of Science,

The University of New South Wales Canberra.

October 2019

Thesis/Dissertation Sheet

Surname/Family Name	:	**Thomas**
Given Name/s	:	**Christoper Maurice**
Abbreviation for degree as give in the University calendar	:	**PhD**
Faculty	:	**UNSW Canberra**
School	:	**School of Science**
Thesis Title	:	**Investigation of spotting and intrinsic fire dynamics using a coupled atmosphere-fire modelling framework**

Large plume-driven wildfires are among the most destructive and unpredictable of all natural hazards. A prerequisite for the development of the deep convection characteristic of these fires is the existence of a large area of active flaming, also known as deep flaming. There are a number of processes associated with the development of deep flaming; many involve some form of dynamic fire behaviour, in which dramatic changes in fire behaviour can occur with little or no change in ambient conditions. Another important driver of deep flaming is intense spotting and spot-fire coalescence, which itself involves dynamic fire behaviour. It is difficult to model dynamic fire behaviour in a computationally efficient way; it cannot be modelled with existing operational fire-spread models.

This thesis is concerned with the modelling of dynamic fire behaviour, and the modelling of ember transport in turbulent plumes. A coupled atmosphere-fire framework is used to model junction fires (the merging of two separate firelines at an acute angle), and the fundamental processes causing the asociated dynamic behaviour are identified. The idea that fireline curvature can act as a proxy for some of the processes underlying dynamic fire behaviour is critically examined, and rejected. A recently-developed simple coupled model, the pyrogenic-potential model, is discussed. It is found to produce results comparable with that of a coupled atmosphere-fire model in simple test cases involving the ignition of fires along circular arcs. The pyrogenic-potential model can capture some forms of dynamic behaviour, and is efficient enough to be used operationally.

To study ember transport in turbulent plumes, a large eddy model is used to simulate the plume from a static heat source, and the resulting wind field is used to model the transport of embers under various assumptions. It is shown that the terminal-velocity assumption, in which embers are assumed to always move at their terminal velocity with respect to the wind field, leads to an overestimate of ember-landing densities at medium to long ranges. This has important implications for the stochastic modelling of spot-fire development.

FOR OFFICE USE ONLY Date of completion of requirements for Award:

ORIGINALITY STATEMENT

‘I hereby declare that this submission is my own work and to the best of my knowledge it contains no materials previously published or written by another person, or substantial proportions of material which have been accepted for the award of any other degree or diploma at UNSW or any other educational institution, except where due acknowledgement is made in the thesis. Any contribution made to the research by others, with whom I have worked at UNSW or elsewhere, is explicitly acknowledged in the thesis. I also declare that the intellectual content of this thesis is the product of my own work, except to the extent that assistance from others in the project's design and conception or in style, presentation and linguistic expression is acknowledged.’

Signed …….....

Date …….....

INCLUSION OF PUBLICATIONS STATEMENT

UNSW is supportive of candidates publishing their research results during their candidature as detailed in the UNSW Thesis Examination Procedure.

Publications can be used in their thesis in lieu of a Chapter if:

- The student contributed greater than 50% of the content in the publication and is the "primary author", ie. the student was responsible primarily for the planning, execution and preparation of the work for publication
- The student has approval to include the publication in their thesis in lieu of a Chapter from their supervisor and Postgraduate Coordinator.
- The publication is not subject to any obligations or contractual agreements with a third party that would constrain its inclusion in the thesis

Please indicate whether this thesis contains published material or not.

☐ *This thesis contains no publications, either published or submitted for publication*

☒ *Some of the work described in this thesis has been published and it has been documented in the relevant Chapters with acknowledgement*

☐ *This thesis has publications (either published or submitted for publication) incorporated into it in lieu of a chapter and the details are presented below*

CANDIDATE'S DECLARATION

I declare that:

- I have complied with the Thesis Examination Procedure
- where I have used a publication in lieu of a Chapter, the listed publication(s) below meet(s) the requirements to be included in the thesis.

Name	**Signature**	**Date (dd/mm/yy)**
Christopher Thomas		

Abstract

Large plume-driven wildfires are among the most destructive and unpredictable of all natural hazards. A prerequisite for the development of the deep convection characteristic of these fires is the existence of a large area of active flaming, also known as deep flaming. There are a number of processes associated with the development of deep flaming; many involve some form of dynamic fire behaviour, in which dramatic changes in fire behaviour can occur with little or no change in ambient conditions. Another important driver of deep flaming is intense spotting and spot-fire coalescence, which itself involves dynamic fire behaviour. It is difficult to model dynamic fire behaviour in a computationally efficient way; it cannot be modelled with existing operational fire-spread models.

This thesis is concerned with the modelling of dynamic fire behaviour, and the modelling of ember transport in turbulent plumes. A coupled atmosphere-fire framework is used to model junction fires (the merging of two separate firelines at an acute angle), and the fundamental processes causing the asociated dynamic behaviour are identified. The idea that fireline curvature can act as a proxy for some of the processes underlying dynamic fire behaviour is critically examined, and rejected. A recently-developed simple coupled model, the pyrogenic-potential model, is discussed. It is found to produce results comparable with that of a coupled atmosphere-fire model in simple test cases involving the ignition of fires along circular arcs. The

pyrogenic-potential model can capture some forms of dynamic behaviour, and is efficient enough to be used operationally.

To study ember transport in turbulent plumes, a large eddy model is used to simulate the plume from a static heat source, and the resulting wind field is used to model the transport of embers under various assumptions. It is shown that the terminal-velocity assumption, in which embers are assumed to always move at their terminal velocity with respect to the wind field, leads to an overestimate of ember-landing densities at medium to long ranges. This has important implications for the stochastic modelling of spot-fire development.

Acknowledgements

I wish to thank my primary supervisor, Associate Professor Jason Sharples, for his help and support during my PhD candidature and the preparation of this thesis, and my secondary supervisors, Professor Jason Evans and Dr Isaac Towers, for many helpful discussions. I acknowledge the support of the Australian Federal Government (and ultimately the Australian taxpayers) for financial support in the form of an Australian Postgraduate Award, and the Bushfire and Natural Hazards Cooperative Research Centre for its financial support. I also acknowledge the resources and services provided to me by the National Computational Infrastructure (NCI), through the National Computational Merit Allocation Scheme, which is supported by the Australian Government (and again, ultimately by the taxpayers of Australia). Thanks to Bob. Above all, I am profoundly grateful to my wife Christine for her continued understanding, support and love.

Publications Arising from Research Undertaken in the Preparation of this Thesis

C. M. Thomas, J. J. Sharples, and J. P. Evans (2015). "Pyroconvective Interaction of Two Merged Fire Lines: Curvature Effects and Dynamic Fire Spread". In: *MODSIM2015, 21st International Congress on Modelling and Simulation.* Ed. by T. Weber, M. J. McPhee, and R. S. Anderssen. Gold Coast, Queensland, Australia: The Modelling and Simulation Society of Australia and New Zealand Inc., pp. 312–318.

C. M. Thomas, J. J. Sharples, and J. P. Evans (2017a). "Evaluating the Terminal-Velocity Assumption in Simulations of Long-Range Ember Transport". In: *MODSIM2017, 22nd International Congress on Modelling and Simulation.* Ed. by G. Syme, D. Hatton MacDonald, B. Fulton, and J. Piantadosi. Hobart, Tasmania, Australia: The Modelling and Simulation Society of Australia and New Zealand Inc., pp. 1187–1193.

C. M. Thomas, J. J. Sharples, and J. P. Evans (2017b). "Modelling the Dynamic Behaviour of Junction Fires with a Coupled Atmosphere–Fire Model". *International Journal of Wildland Fire* 26.4, pp. 331–344.

J. E. Hilton, A. L. Sullivan, W. Swedosh, J. Sharples, and C. Thomas (2018). "Incorporating Convective Feedback in Wildfire Simulations Using Pyrogenic Potential". *Environmental Modelling & Software* 107, pp. 12–24.

C. M. Thomas, J. J. Sharples, and J. P. Evans (in press). "The terminal velocity assumption in simulations of long-range ember transport". *Mathematics and Computers in Simulation.*

Contents

List of Figures

Chapter 1

Introduction

This thesis aims to improve the understanding of the modelling of some of the processes that lead to the development of very large wildfires. Here the term 'very large' is used to loosely encompass the 'very large' and 'extreme' categories of fires proposed by McRae and Sharples 2011. These are characterised by their interaction with higher levels of the atmosphere through the development of a deep convection column, with much of their behaviour being driven by this interaction; they are sometimes known as *plume-driven* fires. (Extensive, high-intensity fires do not necessarily produce deep convection, but may be driven predominantly by the ambient wind; these are known as *wind-driven* fires.) In addition to suitable atmospheric conditions, a prerequisite for the development of deep convection is the existence of a large area of active flaming, also known as *deep flaming* (Sharples et al. 2016b). This can be caused by very strong winds, or a sudden wind change. But deep flaming may also be caused by intense spotting; and by processes involving interactions between separate fires (including coalescing spot fires), between different parts of the same fire, or between the fire and the terrain. Such interactions can produce rapid changes in fire behaviour with little or no change in ambient conditions. This is known as *dynamic* or *intrinsic* fire behaviour. Thus the modelling of dynamic fire behaviour and of ember transport is important to the understanding of the

development of plume-driven fires. Dynamic fire behaviour is also of considerable interest to operational personnel because it may involve sudden, unforeseen changes in fire behaviour.

The modelling of dynamic fire behaviour is problematic. Current operational models cannot account for it, while more complex models may be able to capture it but are too expensive for operational use. This thesis aims to improve our understanding of dynamic fire behaviour, and how to model it, using a coupled atmosphere-fire framework. We investigate the dynamic behaviour resulting from the merging of two firelines (a *junction fire*), and study the mechanisms underlying this behaviour. We examine critically the idea that the incorporation of fireline curvature can lead to more useful operational models by functioning as a proxy for some of the processes underlying dynamic fire behaviour. These ideas have led naturally to the development of a simplified coupled model, the pyrogenic-potential model (Hilton et al. 2018), which can capture some forms of dynamic fire behaviour, and is efficient enough that it could be used operationally. We compare simulations of idealised fires using this model with those using a full coupled atmosphere-fire model.

Junction fires are associated with rapid acceleration of the fireline and very intense fire conditions. They are worthy of study in their own right, but they are also an integral part of the process of spot-fire coalescence (see Figure 1.1). This, and the role that spot-fire coalescence plays in the development of deep flaming, lead us to study the modelling of ember transport under various assumptions, using high-resolution wind fields. The results have implications for the stochastic modelling of spot-fire development.

1.1 Thesis outline

We use the remainder of Chapter 1 to provide a general overview of the concepts involved.

In Chapter 2 we review the previous literature relevant to the research presented in this thesis: dynamic fire behaviour, its modelling, and the transport of embers.

Chapter 3 contains details of the methods used in this research, including a summary of the WRF-Fire coupled atmosphere-fire model (Coen et al. 2013), and details of the modifications made to this model in order to carry out the current research. A description of the pyrogenic-potential model (Hilton et al. 2018) is also given.

Chapter 4 deals with the modelling of junction fires using a coupled atmosphere-fire model. We show that the model reproduces well the dynamic behaviour observed in experimental junction fires, and we use the coupled atmosphere-fire framework to examine in detail the underlying mechanism that produces the dynamic behaviour in this case.

In Chapter 5 we look at the relationship between rate of spread and fireline curvature in the output of the WRF-Fire coupled model. We also compare the results of simulations using WRF-Fire with those using the pyrogenic-potential model.

In Chapter 6 we study the modelling of ember transport at landscape scales using wind fields from high-resolution simulations of turbulent plumes. We examine the use of the terminal-velocity assumption in modelling long-range ember transport in the light of modern computational techniques.

Finally, in Chapter 7 the results of the thesis are discussed, and we indicate possible directions for future work.

1.2 Large wildfires

The behaviour of very large (plume-driven) wildfires is governed by a different set of principles than that of small fires (Countryman 1964; McRae and Sharples 2011). The behaviour of small wildfires is predominantly a function of surface conditions: terrain, fuel conditions, and the surface meteorology. However, the

larger and more intense a fire is, the more it interacts with higher levels of the atmosphere, and the more effect this interaction has on its behaviour, for example by the transport of embers lofted in the plume, or by the convective mixing into the surface flow of drier, faster-moving air from aloft (Countryman 1964). McRae and Sharples (2011) classified wildfires broadly into small/medium fires whose behaviour is determined by surface phenomena; and large, very large and extreme fires, which couple in increasingly strong ways with successively higher levels of the atmosphere. Extreme fires may precipitate a pyrocumulonimbus (pyroCb) event: essentially a thunderstorm with attendant extreme weather phenomena such as lightning, hail, and erratic wind conditions, including downbursts (Rothermel 1991) and tornadoes (McRae et al. 2013). In such cases the surface meteorological, fuel, and terrain conditions are much less significant, and fire behaviour is correspondingly more difficult to predict. These large, plume-driven fires have been responsible for a number of fire-fighter deaths (Lahaye et al. 2018; Rothermel 1991).

1.3 Deep flaming

It is a topic of current research as to what may cause a small fire to transition into a larger one. A number of pathways have been identified, including: atmospheric instability, very rapid rates of fire spread, a change in wind direction, a body of dry upper air passing over an active fire, wind-terrain interactions, and intense spot-fire development (McRae and Sharples 2011). One factor that is considered to be important, and which can result from many of these processes, is the development of an areal flaming zone (or, *deep flaming*) in which a large area of fuel is concurrently actively burning (McRae et al. 2015; Sharples et al. 2016b). This is in contrast to the flaming zone being confined to a perhaps long but relatively shallow front. Intense fire, burning over a large area, can produce strong convective activity and may precipitate a 'fire storm' (Arnold and Buck 1954; Countryman 1964).

1.4 Ember transport, spot-fire ignition, and deep flaming

Much of the early work on the development of spot fires focused on ember transport and maximum spotting distances (Tarifa et al. 1962; 1963; 1964; 1965b; 1966; 1967), and cases of very long-range spotting have been recorded; for example, a maximum spotting distances of 35 kilometres was reported for the Kilmore fire in February 2009 (Tolhurst 2009).

While medium- and long-range spotting may result in new heads of fire, and can cause obvious problems for fire suppression, short-range spotting can be a very significant driver of fire behaviour, and in certain conditions it may become the dominant mode of fire spread in wildland fires (Cheney and Bary 1969; Koo et al. 2010). Short-range intensive spotting can increase the rate of spread by a factor of three to five, and the interaction between large numbers of individual spot fires can lead to their rapid coalescence, resulting in deep flaming and possible extreme fire behaviour (Cheney and Bary 1969). For example, in an analysis of the Air Force Bomb Range fire, Wade and Ward (1973) reported that short-range spotting (up to 800 metres) was partly responsible for the fire travelling more than seven kilometres in less than an hour, with the development of a convection column to about 4,600 metres during that period.

Spotting is also associated with another mode of non-steady fire spread: *vorticity-driven lateral spread* (Sharples et al. 2012; Simpson et al. 2013) in which, through its interaction with the wind and terrain, a fire may spread quickly in a direction lateral to the prevailing wind. This not only causes a rapid broadening of the head fire, but it is typically accompanied by vigorous spotting and the development of a large flaming zone (Sharples et al. 2012). Several instances of this mechanism have been identified in the Australian Alpine fires of 2003 (Sharples et al. 2012), and it has been pointed to as a factor driving pyroCb development in the Grose Valley fire of 2006 (McRae et al. 2015).

1.5 Fire-fire interactions and dynamic fire behaviour

When a large number of fires develop near one another, for example during spotting, these fires can interact with each other to produce violent fire behaviour (Arnold and Buck 1954). This phenomenon, often called a *mass fire*, has been studied extensively, largely in the context of the aftermath of a nuclear attack (e.g. Weihs and Small 1986); see (Finney and McAllister 2011) for a survey of the research in this area. The interaction between multiple fires can produce more intense fire behaviour compared with that of an individual spot fire. In experimental prescribed burns using spot fires, Johansen (1984) observed flame heights increasing up to ten-fold when individual fires merged with each other. This interaction between individual fires may also cause their rapid coalescence (Section 1.3) to produce an extended areal flaming zone (Countryman 1964).

The interaction between different fires is not confined to spot-fire coalescence; separate firelines or different parts of the same fireline can interact to produce severe fire behaviour. McRae et al. (1989) reported spread rates of up to 10 times that of the equilibrium rate for interacting lines of fire during prescribed burns in Canada. An aerial-borne infrared camera was used to monitor burns in Siberian forests and found that unusually high rates of spread were in most cases associated with irregular areas of the fire front e.g. where fingering of the fireline had occurred (see Figure 2.1), or where parts of the fireline were converging (McRae et al. 2005). During the Canberra fire of 2003, the interaction between two merging firelines (the Bendora and the McIntyres Hut fires) resulted in extremely high rates of spread (20 $\mathrm{km\,h^{-1}}$), and convective activity resulting in a tornado with wind speeds estimated at 200 $\mathrm{km\,h^{-1}}$ (Doogan 2006). Motivated in part by this behaviour, Viegas et al. (2012) analysed, both experimentally and analytically, the merging of two straight lines of fire meeting at an acute angle (a *junction fire*), with no ambient wind and flat terrain. They found that the merged firelines initially underwent a very rapid

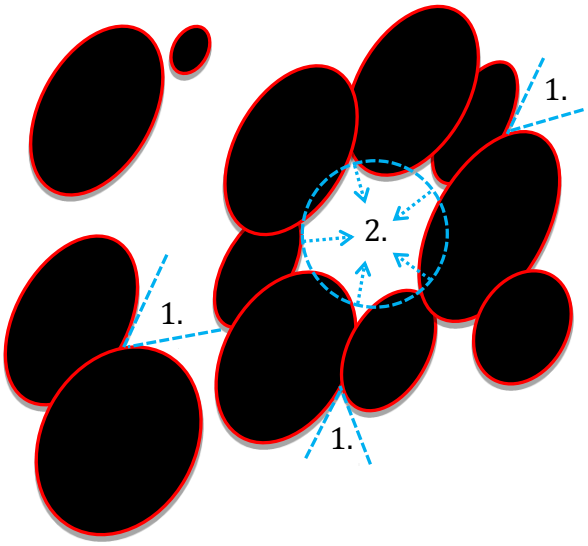

Figure 1.1: Schematic showing the role of junction fires (marked with '1') in spot-fire coalescence. (Figure reproduced from Sharples et al. (2016a)).

acceleration, and they characterised this as a form of extreme fire behaviour. Raposo et al. (2018) extended this work to include the effects of slope. Junction fires are also an important part of the process of spot-fire coalescence, as the schematic in Figure 1.1 shows.

The coalescence of spot fires, and the interaction of merging firelines or different parts of the same fireline (in the case of fingering) are examples of *dynamic fire behaviour* or *intrinsic fire behaviour*. In dynamic fire behaviour, the behaviour of the fire changes, perhaps rapidly, with little or no change in ambient conditions. Eruptive fires are another example of dynamic fire behaviour (Dold and Zinoviev 2009; Viegas and Simeoni 2011; Viegas 2005). Eruptive fires usually occur on steep slopes or canyons and involve a continuous and rapid increase in rate of spread.

Dynamic fire behaviour calls into question the basis on which a lot of fire-behaviour modelling is predicated; that under constant conditions, and perhaps after an initial accelerative phase, a fire will spread at a constant (or at least a quasi-constant) rate. Understanding dynamic fire behaviour and learning how to model it is very important, partly because of its role in the processes that lead to the development

of large fires. Moreover, the fact that dynamic fire behaviour may involve rapid and unheralded changes in fire conditions also makes it of considerable interest to operational personnel. Eruptive fire behaviour, for example, has been associated with a number of fire-fighter deaths (Viegas et al. 2005).

1.6 Wildfire models

1.6.1 Fundamental problem

The fundamental difficulties associated with the modelling of wildfire behaviour result from the complexity of the phenomena involved, the large disparity in scales at which these phenomena occur, and the quantity and quality of data required to accurately specify the condition of the fuel, topography and atmosphere, all of which affect the behaviour of the fire. The size of fuel elements involved in a wildfire may be as small as 10^{-3}–10^{-2} metres, topographical features are typically described at scales of 10^{1}–10^{3} metres, the atmospheric processes involved occur at scales of the order of 10^{0}–10^{4} metres, and the extent of a large fire can be as great as 10^{4}–10^{5} metres. This disparity in scales makes the physical modelling of wildfire behaviour encompassing all these scales prohibitively computationally expensive. Furthermore, even if it were possible to model these phenomena over the full range of scales at which they occur, it is not possible to specify the necessary data (initial and boundary conditions) with sufficient fidelity over this range.

1.6.2 Empirical models

The difficulties of model complexity, scale disparity, and data requirements have led to a number of simplifying approaches. The wildfire characteristic of most interest to operational personnel is the rate of spread of the fire in the direction of the wind (the *heading* rate of spread). Simple fire-spread models therefore reduce the problem to the estimation of a one-dimensional rate of spread (Sullivan 2009b).

Instead of trying to describe and model the processes involved, the estimation of rate of spread may be based on laboratory or field experiments under more or less controlled conditions, with observed rates of spread being correlated with factors such as fuel conditions (fuel types, fuel loads, moisture content), wind speed and topographic slope to produce simple empirical models. Examples include the models of McArthur (1966, 1967), as expressed in equation form by Noble et al. (1980). In some cases, fundamental physical principles might be used in the development of the models, resulting in the so-called semi-empirical (also known as quasi-empirical) models; for example Rothermel (1972). Empirical models (henceforth we use the term 'empirical' to encompass both empirical and semi-empirical models) are essentially scale-free; the fuel bed is treated as amorphous and locally homogeneous, although phenomena at the scale of a fuel element may play a role in the derivation of a semi-empirical model. Consequently, empirical models are not subject to the same computational constraints as physical models, discussed in Section 1.6.4. However, when used in isolation, empirical models can at best predict the mean behaviour of a fire under steady-state conditions. While they may perform well in some circumstances, they do not incorporate the influence of the fire on the atmosphere, they do not explicitly include short-range radiative and convective heat transfer, and they ignore the geometry of the fireline (in the Rothermel model it is assumed to be straight and infinitely long). Thus they are not able to represent dynamic fire behaviour which arises through atmosphere-fire interactions and intrinsic fire dynamics.

1.6.3 Simulation models

Most of the operational fire-spread models in use today are simulation models (Sullivan 2009c) which use fully parametrised empirical or quasi-empirical fire-spread models. Simulation models extend these one-dimensional rate of spread models by employing various spatial propagation methods to compute the evolution of the

fire front across a landscape. Examples of simulation models include FARSITE (Finney 2004) and PHEONIX Rapidfire (Tolhurst et al. 2008). Such models are computationally efficient and may perform well in many circumstances, however they are generally not able to model dynamic fire behaviour because they rely on an empirical model which assumes that the fire has reached a quasi-steady state and that the rate of spread is a function only of the ambient conditions. Dynamic fire behaviour is far from quasi-steady, and may occur without significant changes in the ambient conditions.

1.6.4 Physical models

In contrast to empirical models, physical and quasi-physical models (Sullivan 2009a) explicitly model the physical phenomena over a large range of spatial and temporal scales and they are able to capture a broader sweep of wildfire behaviour. Examples of these types of models include WFDS (Mell et al. 2007), and FIRETEC (Linn et al. 2002). While physical models are able to accurately resolve many aspects of fire behaviour, including some elements of dynamic fire spread, they are very expensive to run and generally unsuited to modelling wildfire at landscape scales. As such they are, for the most part, infeasible as operational tools.

1.6.5 Coupled atmosphere-fire models

Another class of wildfire models are the coupled atmosphere-fire models; examples include CAWFE (Coen 2013), WRF-Fire (Coen et al. 2013) and its offshoot WRF-SFire (Mandel et al. 2011), Méso-NH/ForeFire (Filippi et al. 2009), and ACCESS-Fire (Kepert et al. 2017). Such models couple a physical model of the atmosphere with a fire-spread model which is usually (semi-)empirical, and employ interface tracking methods to model the evolving fire front. Atmospheric conditions, principally wind, are provided to the fire-spread component, which in turn supplies heat and moisture fluxes to the atmospheric model. Coupled models have

a significant computational advantage over physical models because physical phenomena are explicitly modelled only down to scales of the order of hundreds or perhaps tens of metres; smaller-scale atmospheric processes and fire-spread phenomena are parametrised. Coupled models also have a conceptual advantage over uncoupled empirical models; because of the feedback from the fire-spread model to the atmospheric component, they have the potential to capture the pyroconvective atmosphere-fire interactions which appear to be the source of much dynamic fire behaviour and of many of the emergent features of fire spread, such as fireline geometry. For example, coupled models produce the characteristic bowed shape that a straight line fire evolves into under moderate wind speeds (Clark et al. 1996a,b; Coen et al. 2013; Jenkins et al. 2001). This is a feature that uncoupled simulation models typically seek to reproduce using an approach based on Huygen's principle with an elliptic or double-elliptic wavelet stencil (Sullivan 2009c).

Despite their advantages, coupled models are computationally expensive and it is only recently that they have evolved to a form that may be suitable for operational use. Mandel et al. (2014) report that WRF-SFire is being employed operationally in Israel, however they note that the relatively coarse horizontal grid resolution used (444 metres for the atmospheric grid and 44.4 metres for the fire grid) means that the feedback of the fire component to the atmospheric model is reduced. Jiménez et al. (2018) report that NCAR and the Colorado Center of Excellence for Advanced Technology Aerial Firefighting are currently developing an operational fire prediction system based on WRF-Fire. They present fire-spread predictions for an actual fire event using WRF-Fire run with a horizontal atmospheric resolution of 111 metres.

Another problem with coupled models is their use of an empirical fire-spread model. WRF-Fire and WRF-SFire use the Rothermel model which, as noted above, is derived assuming quasi-steady conditions and a straight fireline. It is conceptually

problematic to use this model with dynamic inputs from the atmospheric model, and in cases where the fireline is not straight and possibly quite convoluted. Further, empirical and quasi-empirical models like that of Rothermel are calibrated using ambient wind speeds, for example those that exist in a wind tunnel before a fire is ignited, whereas in a coupled model the wind that is input to the fire component is a combination of the ambient and fire-induced winds. Thus some convective effects are implicitly included in empirical fire-spread models, and some are explicitly represented in the atmospheric model, with the potential that in a coupled model some could be accounted for twice. However empirical fire-spread models are typically calibrated in wind-tunnel experiments which could account for only very small-scale convective effects, much smaller than could be captured by atmospheric models running at typical resolutions. In this thesis we use the WRF atmospheric model at horizontal resolutions no higher than 10 metres, and usually 20 metres or lower; at these resolutions the WRF model could not capture the convective effects implicitly included in the Rothermel fire-spread model and we believe that there is little chance they will have been included twice.

WFDS (Mell et al. 2007) and FIRETEC/HIGRAD (Linn et al. 2002) are examples of coupled models that use a physics-based fire spread model; as noted above they are unsuited to modelling fire at broader landscape scales.

1.7 Modelling dynamic fire behaviour

Dynamic fire behaviour is challenging to model in a computationally efficient way. As noted in Section 1.6.3, most operational fire-behaviour systems use an empirical fire-spread model, and implicitly assume that, under constant ambient conditions, a fire will spread at a quasi-steady rate. By its definition, intrinsic fire behaviour acts in violation of this assumption.

In Chapter 4 of this thesis a coupled atmosphere-fire model, WRF-Fire (Coen et al. 2013) will be used to model the behaviour of junction fires. While such modelling can provide insight into the mechanism underlying dynamic fire behaviour, at the present time coupled atmosphere-fire models are too computationally expensive for operational use. There is a need for simple models that can perhaps capture some aspects of intrinsic fire behaviour, or at least provide more accurate estimates of rates of spread, but still be efficient enough for operational use.

One technique that has been suggested is the introduction of a dependence on fireline curvature into simple fire-spread models. This has been shown (Sharples and Hilton 2017; Sharples et al. 2013) to reproduce qualitatively the behaviour seen in laboratory-scale junction fires (Viegas et al. 2012), and has been used to model field-scale grass fires (Hilton et al. 2016). This idea is critically examined in Chapter 5 of this thesis, where an analysis is made of the relationship between fireline curvature and rate of spread in the output of a coupled atmosphere-fire model.

Recently, Hilton et al. (2018) have developed a simple and very computationally efficient coupled model (the *pyrogenic-potential* model, Section 3.5). Because this model incorporates feedback from the fire to a model of the atmosphere (more precisely, a very simple representation of the surface wind flow) it has the potential to be able to simulate some forms of intrinsic fire behaviour, and has been used to investigate the speed, and intensity, of spot-fire coalescence (Hilton et al. 2017). In Chapter 5 of this thesis we compare the output of this model with that of a full coupled atmosphere-fire model in idealised simulations.

Chapter 2

Literature review

2.1 Dynamic fire behaviour

2.1.1 Introduction

In this section the literature on dynamic fire behaviour is reviewed. Three broad categories are considered: fire-fire interactions, in which separate firelines, or separate parts of the same fireline, interact with each other; fire-terrain interactions, in which the fire interacts with the terrain to produce dynamic fire behaviour (examples include vorticity-driven lateral spread, and eruptive fires); and spot-fire coalescence and mass fires, in which a large number of fires are burning in close proximity.

2.1.2 Fire-fire interactions and fireline geometry

Three large-scale prescribed burns of areas of logging slash in Ontario were studied by McRae et al. (1989), using a helicopter-mounted infrared camera to record fire behaviour. In each case they found elevated rates of spread in zones of interaction between firelines, with rates of spread of up to ten times the projected steady-state rate. Most, but not all, of these elevated rates of spread were found in the zone between a merging back fire and head fire. Two of the burns developed deep convection columns. (The interaction between a head fire and a back fire was

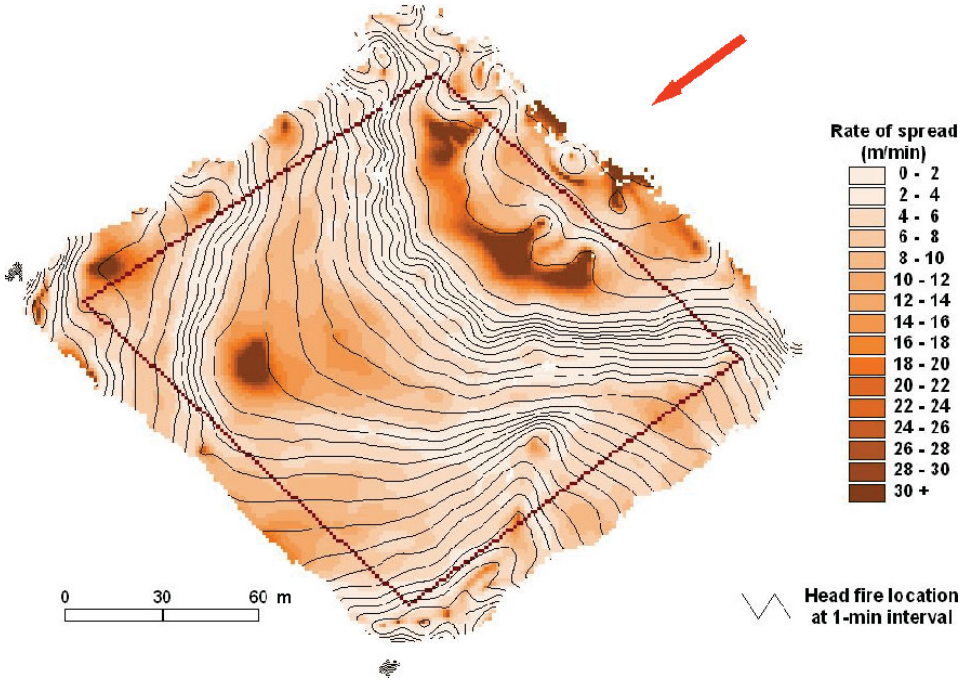

Figure 2.1: Composite map showing rate of spread in an experimental burn of a Siberian forest plot. The lines show the location of the fire front at 1 minute intervals, and the colours indicate rate of spread. The arrow indicates the direction of fire spread. Note the rapid rates of spread seen in the upper-left portion of the plot, in concave regions of the fireline. Reproduced from (McRae et al. 2005), © Canadian Science Publishing or its licensors.

modelled numerically by Morvan et al. (2011) and Dupuy et al. (2011) using coupled physical models. These papers are discussed in Section 2.2.)

McRae et al. (2005) used a helicopter-mounted infrared camera to measure rates of spread in experimental burns of Siberian boreal forest plots. Some abnormally high rates of spread were found, and in most cases these occurred in regions where the fireline had become irregular and developed fingers or convergence zones. High rates of spread were often associated with concave regions of the fireline; their Figure 3 is reproduced in Figure 2.1.

The merging of two firelines at an acute angle was studied experimentally by Viegas et al. (2012). Their experiments were conducted indoors under conditions of no wind and no slope, using included angles of 10°, 20°, 30°, and 45°. In all cases they observed a very rapid initial increase in the rate of spread of the merged fire line

near the intersection of the two fire lines, and a subsequent slowing of this rate of spread. They called this a 'jump fire' but later it became known as a *junction fire* (Raposo et al. 2018). Viegas et al. (2012) made an analytical study of the behaviour in terms of a rotation of the two fire lines and of the 'concentration of energy' near the intersection of the firelines, basing their analysis on radiative effects.

Raposo et al. (2018) extended the study of junction fires to include slope. They performed laboratory-scale and field-scale experiments and, using Rothermel's notion of a propagating flux I_p (Rothermel 1972), which is supposed to include both radiative and convective heat transfer to the unburnt fuel, they examined the hypothesis that the behaviour of junction fires is due only to radiative effects. According to Rothermel's model, the rate of spread R is given by $R = kI_\mathrm{p}$ where k is a constant that depends on fuel conditions. Under some simplifying assumptions, Raposo et al. (2018) used a geometric argument to estimate the radiative flux q from the firelines, and compared it with observed rates of spread. They found that R did not depend linearly on q and concluded that the radiative flux I_p must have a significant convective component. Based on the observed convective flow induced by the junction fire at laboratory scales, Raposo et al. (2018) concluded that convective processes are responsible for the very rapid initial acceleration of junction fires. A scale analysis indicated that the phenomena are similar at laboratory and field scales.

Sharples et al. (2013) and Sharples and Hilton (2017) modelled the behaviour of junction fires using a rate of spread dependent on the curvature of the fireline. These papers are discussed in Section 2.2.

2.1.3 Fire-terrain interactions

2.1.4 Vorticity-driven lateral spread

Using multispectral aerial imagery, Sharples et al. (2012) identified multiple instances of atypical fire spread in several large fires of the 2003 Canberra fire com-

plex, in which the fire spread in a direction approximately perpendicular to that of the prevailing wind. High rates of lateral spread were inferred from the imagery, and the events were accompanied by significant spotting and the development of a large areal flaming zone. Their analysis indicated that the incidents typically occurred on steep lee-facing slopes ($> \approx 25°$) whose aspect was within a critical tolerance ($\approx 40°$) of the downwind direction. They called this phenomenon 'fire channelling' but it has since become known as *vorticity-driven lateral spread*. Sharples et al. (2012) proposed that fire channelling was a result of the interaction of the fire with a separation eddy (or lee rotor) that had formed on the lee side of the ridge.

In combustion wind-tunnel experiments using a ridge with a triangular cross section, Sharples et al. (2010b) reproduced the observations of fire channelling reported in (Sharples et al. 2012), and measured lateral rates of spread 6 to 18 times faster than those observed in the absence of wind.

Simpson et al. (2013) performed two-dimensional and three-dimensional numerical simulations of flow over a triangular ridge using the WRF atmospheric model in large eddy simulation mode, using various wind speeds and atmospheric stability profiles. The two-dimensional simulations showed the formation of large-scale rotors on the lee side of the ridge, whereas these did not form in the three-dimensional simulations, contradicting the hypothesis put forward in (Sharples et al. 2012) to explain the fire channelling. Simulations using the WRF-Fire coupled model were carried out, using two fuel types, brush, and heavy logging slash, with the fire-to-atmosphere feedback turned both on and off. Intermittent episodes of lateral spread, resembling observed fire-channelling events, were obtained in the simulations using heavy logging slash, with the fire-to-atmosphere coupling turned on. These episodes were associated with 'updraft-downdraft interfaces' and accompanying strong vertically-oriented vorticity.

Raposo et al. (2015) elaborated on the experiments of (Sharples et al. 2010b), again using a ridge with a triangular cross section, but studying lateral spread on both the windward and lee faces of the ridge. They found that lateral fire growth on the windward face was small, and relatively independent of slope or wind speed, and that lateral fire growth on the lee face depended quadratically on wind speed. They performed an analysis of the vorticity equations which partially explains the observed lateral spread on the lee face.

Sharples et al. (2015) performed a somewhat simplified theoretical analysis of the vorticity equation to show how tilting and stretching of laterally-oriented vorticity can result in a counter-rotating pair of vertically-oriented vortices, oriented in such a way as to induce lateral spread.

2.1.4.1 Eruptive fires

Viegas (2004) critically examined the idea that with a given set of constant environmental parameters a fire will achieve a steady rate of spread. He made some heuristic arguments for why a fire burning in conditions of constant wind or slope may not achieve an equilibrium rate of spread, and he re-analysed previous experimental data and found that in most cases, with the exception of a line fire burning with no slope and no wind, an equilibrium state was not achieved. He did this experimentally by fitting linear and quadratic functions to the time-varying locations of the heads of experimental fires. These were small-scale experiments in wind tunnels and on inclined plates, including a canyon-shaped inclined plate. A linear fit corresponds to a constant rate of spread; a quadratic fit with a non-zero quadratic coefficient corresponds to a variable rate of spread. Apart from the case of a line-fire ignition in no wind and flat terrain, the best fit obtained was quadratic. The author concluded that the concept of the existence of a quasi-steady rate of spread is problematic. In the case of the canyon-shaped plate the rate of spread increased dramatically under constant conditions.

Viegas (2005) derived a mathematical model under which, with uniform conditions of slope or wind, a feedback between the fire-induced convection and the rate of spread could result in a non-steady, monotonically increasing rate of spread. He assumed simple functional forms, $R' = 1 + a_1 U'^{b1}$ and $dU'/dt = a_2 R'^{b2}$, for the relationship between non-dimensionalised rate of spread R' and non-dimensionalised wind velocity U'. From these, it is easy to derive the differential equation

$$\frac{\mathrm{d}R'}{\mathrm{d}t} = {a_1}^{1/b_1} b_1 a_2 (R' - 1)^{1-1/b_1} R'^{b_2}. \tag{2.1}$$

Depending on the values of the parameters b_1 and b_2, the solutions of Eqn. (2.1) can increase very rapidly. For example, if $b_1 = b_2 = 1$ then one obtains an exponential increase in R' with time. Viegas fitted this model to laboratory-scale experimental results using a model of an inclined canyon. The model agreed reasonably well with validation data from the same experiment. It was then applied to three real fires. It should be noted that Dold and Zinoviev (2009) criticised this model on the grounds that, among other things, the formula $dU'/dt = a_2 R'^{b2}$ implies that a fire burning at a steady rate induces a steadily accelerating wind field, contrary to observations. Viegas et al. (2005) applied this model to four past fires. The parameters appear to have been chosen to fit the model to the available data.

Viegas (2006) extended the study of (Viegas 2005) by relating the values of the parameters a_1, b_1, a_2 and b_2 to fuel-bed properties, considering their possible ranges of values, and relating these to the time evolution of the rate of spread R.

Byram's formula for fireline intensity for a straight-line fire is (Byram 1959), $I = QmR$, where Q is the energy of combustion (J kg^{-1}), m is the fuel load (kg m^{-2}) and R is the rate of spread (m s^{-1}). This formula does not hold for a non-steady rate of spread, in which case one must take into account flame depth and flame-residence time. Building on the work of Albini (1982), who considered fire spread

under non-steady winds, Dold and Zinoviev (2009) used a geometric argument with some simplifications to develop the model

$$\begin{aligned} d(t) &= \int_{t-\tau}^{t} R(t)dt \\ I &= Q\frac{m}{\tau}d \end{aligned} \tag{2.2}$$

where d is the flame depth and τ is the flame-residence time. To close the model they made the hypothesis that $R \propto I^{\nu}$ and showed that if $\nu < 1$ then $R(t)$ will approach a steady rate, whereas if $\nu \geq 1$ then eruptive fire spread can ensue. In the case of fire spread on a slope, Dold and Zinoviev (2009) made an argument that $\nu < 1$ relates to a flame that separates from the surface whereas, in the case of attached flow, $\nu \geq 1$. In (Dold 2010) a simple model of an attached plume was used to explore properties of the unknown relationship between R and I in this case.

Perhaps motivated by the arguments of Dold and Zinoviev (2009) relating eruptive fire behaviour to flame attachment, Sharples et al. (2010a) drew parallels between eruptive wildfire incidents and the King's Cross Underground fire (Crossland 1992), in which the flames attached to the bottom of an escalator trench, and spread rapidly up it. Experiments show that flames can attach to surfaces inclined at angles greater than a critical angle of 24°- 27° provided that the lateral entrainment of air is inhibited in some way, for example by the sides of a canyon; see the references cited in (Sharples et al. 2010a). Sharples et al. (2010a) discuss two incidents of fire eruption (Tuolomne, California, 2004, and Mansfield, Victoria, 2006) which appear to be attributable to flame attachment.

Edgar et al. (2015) performed computational fluid dynamics (CFD) simulations of the King's Cross Underground fire using a static heat source, and angles of 10°, 20°, and 30° for the escalator trench. They found that flame attachment occurred for the case of 30°, but not for the 10° and 20° cases, providing the first numerical

evidence for a critical angle for flame attachment of somewhere between 20° and 30°. Edgar et al. (2016) extended this work by simulating trench angles of 20°, 22°, 24°, 26°, 28°, and 30°, and heat sources with strengths 20, 200, and 2000 kW. They found that for trench angles of 24° or less, flames did not attach to the floor of the escalator trench, but that they did attach for angles of 26° or more, thus determining the critical angle to be between 24° and 26°, in agreement with the experimental work cited in (Sharples et al. 2010a).

2.1.5 Spot-fire coalescence and mass fires

Arnold and Buck (1954) defined 'blow-up' fires as 'those which exhibit violent build-up in fire intensity or rate of spread sufficient to prevent direct control by efficient application of conventional fire fighting methods.' They discussed four main classes of conditions leading to blow-up fires: atmospheric conditions; topography; surface burning conditions; and ignition and burning patterns. It is the last of these that relates most to our definition of dynamic fire behaviour. They note that a number of individual fires burning in an area, such as might result from spot fire ignition, can interact and coalesce, leading to 'area-ignition' and a 'fire-storm'. They also describe how two or more fires burning in close proximity can interact to produce violent fire behaviour.

Johansen (1984) reported on an experimental prescribed burn in a pine forest in Georgia. Plots were ignited using a pattern of spot ignition, and flame heights were observed during the burn, with scorch heights being measured two weeks later. They noted a rapid increase in flame heights, of up to ten-fold, as individual spot fires merged. The merging of flank fires caused a rapid increase in the width of individual fire fronts and a corresponding increase in flame height, but maximum flame heights occurred where back fires merged with head fires.

Hilton et al. (2017) used the pyrogenic-potential model (Section 3.5) to simulate the coalescence of spot fires. The model was the same as that used in (Hilton et al. 2018), as described in Sections 2.2 and 3.5. The model domain was 10×10 metres, spot fires were initialised in the central 2×2 metre region, and an ambient wind of $\mathbf{w_a} = 0.1\ \mathrm{m\,s^{-1}}$ was imposed. The parameters u_0, u_1 and k (see Eqn. (2.4)) were chosen for illustrative purposes, and do not necessarily correspond to any physical reality. Simulations were run with $k = 0$, corresponding to no convective feedback, and with a range of values of $k > 0$. The number N of spot fires was also varied. The simulations showed that the convective feedback caused the fires to coalesce more rapidly, and that for $N > 5$ spots, there was a higher peak in total fireline intensity than if convective feedback was ignored. This latter effect became more marked with increasing N.

2.2 Modelling dynamic fire behaviour

One of the earliest models of dynamic fire behaviour was the coupled atmosphere-fire model of Clark et al. (1996a,b). They coupled a non-hydrostatic mesoscale atmospheric model to the McArthur empirical fire spread model (McArthur 1967; Noble et al. 1980). A tracer-type front-tracking algorithm was used to track ignition of the fuel, and sensible and latent heat fluxes, computed from the burning fuel, were returned to the lower levels of the atmospheric model using a simple extinction depth formulation. Clark et al. (1996b) defined the convective Froude number F_c by

$$F_\mathrm{c}{}^2 = \frac{(|\mathbf{w}_\mathrm{a}| - R_\mathrm{f})^2}{g(\langle \Delta\theta \rangle / \theta) W_\mathrm{f}},$$

where $\mathbf{w}_\mathrm{a}$ is the ambient wind, R_f is the rate of spread, $\langle \Delta\theta \rangle$ is the mean value of the potential temperature anomaly $\Delta\theta$ over the flaming region, and W_f is the width of this region in the downwind direction. F_c measures the degree of coupling between the atmosphere and the fire. If $F_\mathrm{c} \gg 1$ then the atmosphere is not strongly affected

by the heat from the fire, if $F_c \approx 1$ then both the ambient flow and the fire are important in determining the dynamics, and if $F_c \ll 1$ then the dynamics are dominated by the heat supplied by the fire. Clark et al. (1996b) performed a number of numerical experiments with this coupled model and, because they were performed with homogeneous fuel conditions and no topography, the dynamic effects observed were solely a result of the convective interaction between the atmospheric and fire models. They estimated ${F_c}^2 \approx 0.3$ for these experiments. Simulated fires were ignited in straight lines of lengths 420 and 1500 metres, with varying background wind strengths. Short (420 metre) firelines under moderate wind conditions developed the characteristic bow shape, which Clark et al. attributed to a low-level convergence pattern induced by the convective column, shifted ahead of the fireline by the ambient wind. Under low-wind conditions, the convective column remained above the fire, strong buoyancy gradients produced horizontal vortices which were tilted by the vertical motion, and the resulting vertical vorticity broke up the fireline. The longer (1500 metre) firelines could not sustain the single convection column that causes the bow-shaped fireline; the convection column became unstable and broke into two parts, each creating their own convergence zones in the low-level winds and causing what Clark et al. called 'convective fingering'. This fireline structure has been observed in real fires, for example the 1985 Onion sagebrush fire (Clark et al. 1996b). In (Clark et al. 1996a), more simulations were performed, using the same model, to investigate further the fire-induced dynamics over a range of values of F_c, using wind speeds of 1, 3, 4, 5, 10, and 15 $\mathrm{m\,s^{-1}}$. For high ambient wind speeds ($\geq 10\ \mathrm{m\,s^{-1}}$) they found no noticeable effects of feedback from the fire. For moderate wind speeds they identified three types of fire-induced dynamics: the bow-shaped firelines discussed above; a vertically-oriented vortex pair situated at the front of the fireline, caused by the bow shape of the fireline, and oriented so as to blow wind back into the fire; and an instance of *dynamic fingering*. The last of these is a small-scale, short-lived phenomenon involving a vertically-oriented vortex

pair, oriented so as to increase the rate of spread of the fire. Clark et al. attributed this to the tilting of horizontal vorticity created by negative vertical wind shear (i.e. the near-surface wind is greater than that just aloft). They conjectured that dynamic fingering may be an important mechanism of fire spread at small scales.

Dynamic fingering appears to be very similar to behaviour reported in Chapter 4 of this thesis: vertically-oriented vortex pairs cause rapid jumps in the advance of the fireline in coupled atmosphere-fire simulations of junction fires. In Section 4.3.4 it will be shown that the vertical vorticity is a result of the tilting of buoyancy-induced horizontal vorticity, and it will be argued that this is a major mechanism in the rapid acceleration of junction-fires.

Morvan et al. (2011) simulated the interactions between a head fire and a suppression back fire in Australian grasslands and Mediterranean shrublands, using a two-dimensional (x–z) physical model FIRESTAR (Morvan et al. 2009), and a three-dimensional physical model WFDS (Mell et al. 2007). They observed three distinct phases: the fires propagate independently in opposite directions, the fires interact, and the fires merge. During the third phase merging, a sudden increase in fire intensity and flame height can occur. This has often been reported in real fires, e.g. (McRae et al. 1989).

(Dupuy et al. 2011) also modelled the interaction between head fires and back fires, using the FIRETEC (Linn et al. 2002) coupled physical model. They performed both two-dimensional and three-dimensional simulations. When simulating a single fire they found that the two-dimensional model underestimated wind velocities downwind of the fire, and overestimated the downwind indraft, because the ambient wind cannot penetrate the plume in a two-dimensional model. They concluded that accurate modelling of the interaction between a head fire and a back fire required three-dimensional modelling.

Several authors have discussed the idea that firelines might evolve with a rate of spread dependent on curvature; examples include Weber (1989), Wheeler et al. (2013), Sharples et al. (2013), Hilton et al. (2016), Sharples and Hilton (2017), and Fendell and Wolff (2001) (who made a critical assessment). Intuitively, this is an attractive notion: in regions of negative curvature one might expect an increased rate of radiative and convective transfer of heat to the unburnt fuel. Note the areas with abnormally high rates of spread in the upper-left region of Figure 2.1.

Sharples et al. (2013) used a very simple model with a curvature-dependent rate of spread to reproduce qualitatively the work of Viegas et al. (2012). Instead of considering a junction fire as two separate lines of fire, they focussed on the geometry of the merged fireline. They modelled junction fires assuming a rate of spread in the normal direction of the front of the form $R(\kappa) = 1 - \varepsilon\kappa$ where R is the normalised rate of spread (equal to 1 for a straight fireline), κ is the signed curvature of the front (see Section 5.1.1) and $\varepsilon > 0$ is a fitting parameter. They were able to reproduce, qualitatively, the 'jump fire' phenomena reported by Viegas et al. (2012). Sharples and Hilton (2017) refined this modelling by tracking the evolving fire front using a level-set method (Section 3.3.3), which allows for more appropriate boundary conditions to be imposed than those in (Sharples et al. 2013). They defined the normal speed of the front as $\beta - \alpha\kappa$, where $\alpha, \beta > 0$ are free parameters, and were able to reproduce reasonably well the experimental results of Viegas et al. (2012). However they noted that the model parameters that provided the best fit to the experimental data were dependent on the size of the angle between the initial firelines.

Hilton et al. (2016) have incorporated curvature dependence into a simple model of wind-driven fire spread. Their model uses the level set technique discussed in

Section 3.3.3. In their formulation, the level-set equation, Eqn. (3.1), is

$$\frac{\partial \varphi}{\partial t} + \left(-\alpha\kappa + \beta + \gamma \max\left(\hat{\mathbf{w}} \cdot \hat{\mathbf{n}}, 0\right)\right) |\boldsymbol{\nabla}\varphi| = 0, \tag{2.3}$$

where α, β and γ are parameters, κ is the signed curvature, $\hat{\mathbf{w}}$ is the wind direction, and $\hat{\mathbf{n}} = \boldsymbol{\nabla}\varphi/|\boldsymbol{\nabla}\varphi|$ is the outward unit normal. Note that γ is not a wind multiplier, it is the wind-induced rate of spread of the fireline in the direction $\hat{\mathbf{w}}$ of the wind and has units $\mathrm{m\,s^{-1}}$. The parameter α, with units $\mathrm{m^2\,s^{-1}}$, controls the curvature-induced rate of spread, and β is the rate of spread of a straight fireline with no wind ($\mathrm{m\,s^{-1}}$). The model was tested on laboratory-scale fires ignited in a wind tunnel, with parameters α, β and γ selected manually, and it reproduced well the evolving fireline shape. It was also tested on two field-scale experimental grass fires (Cruz et al. 2015). In this case a simple metric was used to evaluate the difference between experimental and modelled results at any particular time step; it amounts to $m = \sqrt{\mu\left((B_\mathrm{e} \setminus B_\mathrm{m}) \cup (B_\mathrm{m} \setminus B_\mathrm{e})\right)}$, where B_e and B_m are respectively the experimental and modelled burnt regions, and $\mu(R)$ represents the area of any region R. The smaller the value of m, the better the regions match, although it should be noted that this metric is not invariant under scaling. Parameters were selected by a brute-force search of the parameter space to minimise the average of m at a number of time steps. The inclusion of the curvature term ($\alpha > 0$) led to a much better fit between experimental and modelled results than if α was constrained to be zero.

Hilton et al. (2018) developed a new model which couples a simple representation of the near-surface atmospheric flow with a fire-spread model to give a very efficient coupled model. This model is capable of simulating dynamic fire behaviour because of the two-way coupling between the surface flow and the fire-spread. Details of the generic model are given in Section 3.5. Various formulations of it's implementation

in (Hilton et al. 2018) are possible, but it in essence it can be summarised as:

$$\left.\begin{aligned} \frac{\partial \varphi}{\partial t} + (u_0 + u_1 \max((\mathbf{w_a} + \mathbf{w}) \cdot \hat{\mathbf{n}}, 0))|\boldsymbol{\nabla}\varphi| = 0 \\ \mathbf{w} = \boldsymbol{\nabla}\psi \\ \boldsymbol{\nabla}^2\psi = kI_\varepsilon \end{aligned}\right\} \tag{2.4}$$

where φ is the level-set function, $\mathbf{w_a}$ is the ambient wind, $\mathbf{w}$ is the fire-induced wind, ψ is the pyrogenic potential, and I_ε is the two-dimensional smoothed version of Byram's fireline intensity given by Eqn. (3.6). There are three parameters: u_0 is the rate of spread in still conditions, u_1 is a dimensionless parameter controlling the wind-aided rate of spread, and k controls the strength of the source term in the Poisson equation.

In simulations of wind-driven fires ignited initially along a straight line, the model naturally produces the characteristic parabolic-shaped fireline that is seen in experiments and in coupled atmosphere-fire simulations; it is the only two-dimensional fire-spread model that does this. The model results matched well with experimental fires ignited in a wind tunnel, though the authors note that it is difficult to define precisely the flame zone in small-scale fires. The model was tested on the same field-scale grass fires as in Hilton et al. (2016). A different index to that of (Hilton et al. 2016) was used to quantify the differences in experimental and simulated burnt areas: $S = 2\mu(B_\mathrm{e} \cap B_\mathrm{m})/(\mu(B_\mathrm{e}) + \mu(B_\mathrm{m}))$ which is scale invariant, and varies between 0 and 1, with 1 corresponding to a perfect match. A brute-force search of the parameter space was used to maximise the average of S over all time steps. Using these parameters the model results matched well with experimental results.

2.3 Transport of embers

2.3.1 Introduction

In this section much of the literature on ember transport published up to 2017 is reviewed. Section 2.3.2 contains some preliminary material consisting of an overview of the equations governing the motion of embers, and a discussion of some of the simplifying assumptions that are commonly made.

2.3.2 Equations of motion

The forces acting on an ember are gravity, the buoyancy force, and the drag and lift forces, $\mathbf{F}_\mathrm{d}$ and $\mathbf{F}_\mathrm{l}$, associated with the motion of the ember relative to the atmosphere. For the sake of clarity of exposition it will be assumed that all forces act through the centre of inertia of the ember, and rotational motion will not be considered. Furthermore, because the density of an ember is much greater than that of the atmosphere, the buoyancy force can be neglected. The momentum equation therefore becomes

$$\frac{\mathrm{d}\mathbf{M}}{\mathrm{d}t} = \mathbf{F}_\mathrm{d} + \mathbf{F}_\mathrm{l} + m_\mathrm{e}\mathbf{g}, \tag{2.5}$$

where m_e is the mass of the ember, and $\mathbf{g} = -g\mathbf{k}$ is the acceleration due to gravity. During pyrolysis, part of the mass of the ember is ejected as gas through the surface Σ of the ember. The time rate of this ejection of mass is $\int_\Sigma \rho_g \mathbf{v}_\mathrm{g} \cdot \mathbf{n}\, d\sigma$, where $\mathbf{v}_\mathrm{g}$ is the velocity of the escaping gas in the reference frame of the ember, and ρ_g its density. Following Tarifa et al. (1967),

$$\frac{\mathrm{d}\mathbf{M}}{\mathrm{d}t} = m_\mathrm{e}\frac{\mathrm{d}\mathbf{u}}{\mathrm{d}t} + \mathbf{u}\frac{\mathrm{d}m_\mathrm{e}}{\mathrm{d}t} + \int_\Sigma (\mathbf{u} + \mathbf{v}_\mathrm{g})\rho_\mathrm{g}\mathbf{v}_\mathrm{g} \cdot \mathbf{n}\, d\sigma, \tag{2.6}$$

where $\mathbf{u}$ is the velocity of the ember and the third term on the right hand side of Eqn. (2.6) represents the rate of change of momentum due to the ejection of

pyrolysis products through the ember's surface Σ. The change of mass of the ember is entirely due to this ejection, so that

$$\frac{\mathrm{d}m_\mathrm{e}}{\mathrm{d}t} + \int_\Sigma \rho_\mathrm{g} \mathbf{v}_\mathrm{g} \cdot \mathbf{n} \, d\sigma = 0.$$

Substituting this into Eqn. (2.6) gives

$$\begin{aligned} \frac{\mathrm{d}\mathbf{M}}{\mathrm{d}t} &= m_\mathrm{e} \frac{\mathrm{d}\mathbf{u}}{\mathrm{d}t} + \int_\Sigma \rho_\mathrm{g} \mathbf{v}_\mathrm{g} \mathbf{v}_\mathrm{g} \cdot \mathbf{n} \, d\sigma \\ &\approx m_\mathrm{e} \frac{\mathrm{d}\mathbf{u}}{\mathrm{d}t}. \end{aligned} \tag{2.7}$$

The approximation is justified because the integral term represents the self-propulsion of the ember due to the differential ejection of gases, and can usually be neglected; gas densities are virtually constant over the ember surface, and ejection velocities are essentially constant, and in any case are small (Tarifa et al. 1967). In rare cases, and for short periods, self-propulsion of embers has been observed, for example in pine cones (Tarifa et al. 1967).

If $\mathbf{w}$ is the wind field then, according to the quadratic drag law for high Reynolds number flows (Batchelor 1967), the drag force is parallel to $\mathbf{w} - \mathbf{u}$ and is given by

$$\mathbf{F}_\mathrm{d} = \frac{C_\mathrm{d} A_\mathrm{p} \rho}{2} |\mathbf{w} - \mathbf{u}| (\mathbf{w} - \mathbf{u}) = \alpha m_\mathrm{e} |\mathbf{w} - \mathbf{u}| (\mathbf{w} - \mathbf{u}) \tag{2.8}$$

where C_d is the drag coefficient, A_p is the projected area of the ember in the direction of $\mathbf{w} - \mathbf{u}$, ρ is the atmospheric density, and

$$\alpha = \frac{C_\mathrm{d} A_\mathrm{p} \rho}{2 m_\mathrm{e}}. \tag{2.9}$$

The lift force is perpendicular to $\mathbf{F}_\mathrm{d}$ and has magnitude

$$|\mathbf{F}_\mathrm{l}| = \frac{C_\mathrm{l} A_\mathrm{p} \rho}{2} |\mathbf{w} - \mathbf{u}|^2$$

where C_l is the coefficient of lift. $\mathbf{F}_\mathrm{l}$ is neglected in many treatments of ember transport, in which case (2.5), (2.7) and (2.8) give

$$\frac{\mathrm{d}\mathbf{u}}{\mathrm{d}t} = \alpha |\mathbf{w} - \mathbf{u}| (\mathbf{w} - \mathbf{u}) + \mathbf{g}. \tag{2.10}$$

Setting $\mathbf{u}_\mathrm{r} = \mathbf{u} - \mathbf{w}$, the relative velocity of the ember with respect to the wind $\mathbf{w}$, Eqn. (2.10) can be rewritten as

$$\frac{\mathrm{d}\mathbf{u}_\mathrm{r}}{\mathrm{d}t} + \alpha |\mathbf{u}_\mathrm{r}| \mathbf{u}_\mathrm{r} = \mathbf{g} - \frac{\mathrm{d}\mathbf{w}}{\mathrm{d}t}. \tag{2.11}$$

Note that α varies with $\mathbf{u}_\mathrm{r}$, ρ, m_e and the size, shape, and orientation of the ember. Equation (2.11) represents a Lagrangian approach to particle modelling. There is an extensive modern literature on Lagrangian transport (e.g. Weil et al. 2004, Lin et al. 2011).

2.3.3 The transport problem

The solution of Equation (2.11) presents several problems: the wind field $\mathbf{w}$ above a fire is complicated and poorly understood; the burning characteristics of an ember must be known because they influence α and the likelihood of an ember causing ignition when it reaches the ground; and Eqn. (2.11) is not closed unless α is assumed to be constant or a function of t and $\mathbf{u}_\mathrm{r}$ only.

Without easy access to computing power, early work on the transport of embers was a combination of experiments and analytical techniques with appropriate simplifying assumptions; the work of Tarifa and del Notario (1962) and Tarifa et al. (1965a, 1963, 1964, 1967, 1966, 1965b), and Albini (1979, 1981a,b, 1982, 1983a,b,c) are examples. More recently, it has become possible to perform high resolution numerical simulations of atmospheric processes (large eddy simulations, or LES) and combustion processes, both separately and in coupled models; for example Himoto and Tanaka (2005), Koo et al. (2012) and Thurston et al. (2013) and Thurston et al. (2017). This improvement in computational techniques has allowed some simplifying assumptions to be relaxed and problems of greater complexity to be tackled. On the other hand it is often the case that greater insight into the nature of the phenomena can be gained from an analytical approach, despite the simplifications that have to be made.

2.3.4 The literature on ember transport

Tarifa and his various collaborators made the first systematic study of ember transport in a series of reports (Tarifa and del Notario 1962; Tarifa et al. 1965a, 1963, 1964, 1967, 1966, 1965b). Tarifa and del Notario (1962) wrote Equation (2.11) as a system of two equations, by choosing the x-direction parallel to $\mathbf{u}_\mathrm{r}$, and obtained an analytical solution under the assumptions of constant wind velocity ($\mathrm{d}\mathbf{w}/\mathrm{d}t = 0$) and constant α. They found that for reasonable values of α the solution $\mathbf{u}_\mathrm{r}$ quickly converges to a terminal velocity, relative to the wind field $\mathbf{w}$, of $\mathbf{u}_\infty = (0, -u_\infty)$ where

$$u_\infty = \sqrt{\frac{g}{\alpha}} = \sqrt{\frac{2m_\mathrm{e}g}{C_\mathrm{d}A_\mathrm{p}\rho}} \tag{2.12}$$

is the terminal fall speed of the ember. They concluded that for their purposes there was little error in assuming that, with respect to the surrounding atmosphere, an ember always flies at terminal velocity, that is $\mathbf{u}_\mathrm{r} = \mathbf{u}_\infty$, and in (Tarifa et al. 1963)

they made an analysis of the maximum errors introduced by making this so called *terminal-velocity assumption*. This assumption greatly simplifies the computation of ember trajectories and has been used in many subsequent investigations of ember transport. However, it is based on the assumption that the wind field varies slowly in comparison to the time taken for an ember to attain terminal velocity. More recent work by Koo et al. (2012) has shown that making the terminal-velocity assumption results in an underestimate of ember travel distances in high-resolution modelling of short-range ember transport from surface fires. The validity of the terminal-velocity assumption for the modelling of long-range ember transport in turbulent plumes is examined in Section 6 of this thesis.

Under the terminal-velocity assumption the ember velocity is given by

$$\mathbf{u} = \mathbf{w} - u_\infty \mathbf{k} \tag{2.13}$$

where the wind field $\mathbf{w}$ is taken as known. Two simple models of $\mathbf{w}$ were used in the work of Tarifa et al.: a vertical convection column, and an inclined column of fixed width. Vertical wind velocities in both columns were assumed constant and both were superimposed on a constant ambient horizontal wind. It was assumed that embers were randomly ejected by turbulence from the vertical column, whereas the height that an ember achieved in the inclined column depended on its initial position.

With $\mathbf{w}$ known, once the time dependence of u_∞ has been determined it is possible to integrate Equation (2.13) and determine ember trajectories, and hence determine the maximum distances that embers could be transported and still be burning when they reached the ground. Thus most of the subsequent work of Tarifa et al. consisted of elucidating the time dependence of u_∞.

The change in α, and hence u_∞, arise in two ways: changes in the orientation of the ember with respect to $\mathbf{w} - \mathbf{u}$ which, unless the ember is a sphere, alters A_p and C_d; and ember combustion, which alters m_e, C_d, and A_p.

When wooden cylinders and square plates were dropped from a balloon and allowed to fall freely, drop times did not differ appreciably from those calculated as if the cylinder or plate had fallen the entire distance in an orientation of maximum drag (Tarifa et al. 1964, 1967). Consequently all experimental and theoretical work was done assuming that the ember was oriented in its position of maximum drag.

Some of the experimental work on combustion was done at terminal velocity, which changes as the ember burns, but much of it was done using a constant relative wind speed because the experimental apparatus is simpler.

Tarifa et al. (1963, 1964) used a wind tunnel to directly determine $u_\infty(t)$ and burn-out times for burning embers at terminal velocity. Spheres, cylinders and square plates of various species and sizes were studied.

To provide some general results, Tarifa et al. (1964, 1965b) introduced the dimensionless quantities

$$u^* := \frac{u_\infty}{u_{\infty,0}}$$
$$t^* := \frac{t}{t_\mathrm{b}}$$

where $u_{\infty,0} := u_\infty(0)$ is the initial (unburnt) terminal fall speed of the ember and t_b is time to burn out. They developed a simple empirical expression relating u^* and t^* under conditions of flight at terminal velocity:

$$u^* = \frac{1}{1 + \eta \left(\frac{t^*}{1-t^*}\right)^\gamma} \tag{2.14}$$

where the parameters η and γ are determined empirically and depend on the shape and species of the ember. They also developed some simple empirical expressions for t_b as a function of initial (i.e. unburnt) ember density $\rho_{\mathrm{e},0}$. These, together with Equation (2.14), allow $u_\infty(t)$ to be computed since $u_{\infty,0}$ can be determined from the intial characteristics of the ember.

Finally, in (Tarifa et al. 1967, 1966) experimental work and dimensional analysis was used to provide very general formulae for various characteristics of wood particles burning with forced convection. For combustion at *constant* relative wind speed w_r, for which the experimental setup is simpler than combustion at terminal velocity, they define the dimensionless quantities:

$$\chi := \frac{w_\mathrm{r} t}{D_0}, \quad \mathrm{Re} := \frac{w_\mathrm{r} D_0 \rho}{\mu_\mathrm{a}}, \quad \zeta := \frac{\rho}{\rho_{\mathrm{e},0}}, \quad \lambda_1 := \frac{L_{\mathrm{f},0}}{D_0}, \quad \lambda_2 := \frac{l_{\mathrm{f},0}}{D_0},$$

where the subscript 0 indicates the initial (unburnt) values of the respective quantities. Here w_r is the relative wind speed, D_0, L_0 and l_0 are characteristic lengths of the ember, μ_a is the viscosity of air, and ρ and ρ_e are the density of the atmosphere and the ember respectively. The parameter χ characterises the combustion process, Re is the Reynolds number, ζ characterises the ember material, and λ_1 and λ_2 are representative of the ember's shape. According to dimensional analysis, any property ξ of the ember, when non-dimensionalised as ξ/ξ_0, can be expressed as

$$\frac{\xi}{\xi_0} = \Phi(\chi, \mathrm{Re}, \zeta, \lambda_1, \lambda_2)$$

for some function Φ. As an example, from their experimental data on combustion at constant windspeed Tarifa et al. (1967) found that, for spherical and cylindrical

embers, the quantity $u_\infty^{\mathrm{c}}/u_{\infty,0}$ correlated well with

$$U = \chi \mathrm{Re}^{-0.4} \zeta^{1.3} {\lambda_1}^{-0.4}.$$

Here u_∞^{c} is the (time-dependent) terminal velocity of the ember whose combustion is occurring at constant relative wind speed w_{r}.

For combustion at terminal velocity they provided a similar analysis but replaced χ and Re with

$$\chi_\infty := \frac{u_{\infty,0}\, t}{D_0}, \quad \mathrm{Re}_\infty := \frac{u_{\infty,0}\, D_0\, \rho}{\mu_{\mathrm{a}}}.$$

They found that, for example, $u_\infty/u_{\infty,0}$ correlated well with

$$U_\infty = \chi_\infty \mathrm{Re}_\infty^{-0.4} \zeta^{1.3} {\lambda_1}^{-0.4} K \lambda_2 \tag{2.15}$$

where K is a shape factor.

The work of Tarifa et al. on combustion at constant wind speed was motivated by the fact that the experimental set-up is simpler than for combustion at terminal velocity. However real embers do fly at their terminal velocity, which is not constant. Tarifa et al. (1967) showed how to determine $u_\infty(t)$ from $u_\infty^c(t)$ under the reasonable simplifying assumption:

$$\frac{\mathrm{d}u_\infty}{\mathrm{d}t} = \left.\frac{\mathrm{d}u_\infty^c}{\mathrm{d}t}\right|_{u_\infty^{\mathrm{c}}=u_\infty}.$$

Lee and Hellman (1969) considered spherical embers burning in a rotating convection plume, a wind field model somewhat more complex than the simple two-dimensional plumes studied by Tarifa et al. They used an empirical formula developed by Tarifa et al. (1965a, 1964) for the diameter D of a spherical particle

burning at a constant relative wind speed v_r, ${D}^2 = {D_0}^2 - (\beta + \delta v_\mathrm{r})t$, and made the assumption that the burning rate is independent of the relative wind speed, i.e. that $\delta = 0$, so that

$$D = \left({D_0}^2 - \beta t\right)^{1/2} \tag{2.16}$$

where the parameter β depends on the ember material. They further assumed that the ember density ρ_e and drag coefficient C_d are constant. With these assumptions, and using Eqns. (2.16) and 2.9, the quantity α in Eqn. (2.11) becomes a known function of time. They did not use the terminal velocity assumption, but numerically integrated Eqn. (2.11), which they wrote in cylindrical coordinates because of the nature of the wind field $\mathbf{w}$. Ember trajectories were computed for a number of choices of the model parameter values, and the general behaviour predicted by the numerical results was verified by experiments in a plume generator. Lee and Hellman (1970) refined and extended this work by using a modified burning rate which depends on the relative wind speed, and by computing ember trajectories for both a rotating convection plume and an inclined convection column.

Muraszew (1974) developed a simple end-to-end model of spot fire hazard, including ember transport, a model of the convection regime above a line fire, and ignition of spot fires by falling embers. Under the terminal velocity assumption, the computation of ember trajectories only requires knowledge of the time evolution of the terminal velocity of the ember. However, to assess the hazard posed by an ember that has landed, an estimate of it's size and mass is required. Muraszew (1974) used data from Tarifa et al. (1965a,b) to develop an empirical model for the evolution of density ρ_e of burning wooden spheres:

$$\frac{\rho_\mathrm{e}}{\rho_{\mathrm{e},0}} = \exp\left(-\frac{t}{57 D_0}\right). \tag{2.17}$$

Using Equation (2.12) and assuming a constant drag coefficient C_{d} this gives an expression for the size of a falling ember:

$$\frac{D}{D_0} = \left(\frac{u_\infty}{u_{\infty,0}}\right)^2 \frac{\rho_{\mathrm{e},0}}{\rho_{\mathrm{e}}}$$

which, together with Eqn. (2.17) and some empirical correlations made by Tarifa et al. (1967) with the quantity $\tilde{U}$ given (2.15), provides an empirical determination for $m_{\mathrm{e}}(t)$. Muraszew (1974) developed a simple two dimensional analytic model of a convection plume above a line fire, consisting of a two zones: a high buoyancy zone, where combustion is occurring, topped by a low buoyancy zone of constant vertical wind velocity. The convection column is tilted by the wind. Muraszew noted that this convection plume was probably not strong enough, even in the largest fires, to lift any but the smallest embers.

Muraszew et al. (1975) studied wooden cylinders burning in a wind tunnel and refined Equation (2.17) to obtain

$$\frac{\rho_{\mathrm{e}} - \rho_{\mathrm{c}}}{\rho_{\mathrm{e},0} - \rho_{\mathrm{c}}} = \exp\left(\frac{-t}{KD_0}\right)$$

where ρ_{c} is the final density after complete burning; K was given the value 45 for burning in quiescent air and 76 for any relative windspeed greater than 8 $\mathrm{km\,h^{-1}}$. It was found that this gave values of $u_\infty/u_{\infty,0}$ that agreed reasonably well with Tarifa's experimental data and with values derived using Tarifa's dimensional analysis (Tarifa et al. 1967). In the same report Muraszew et al. (1975) developed an analytic model of a fire whirl, which couples boundary layer atmospheric conditions, the physics of the fire and the flow of the vortex core, and tested the model in an

apparatus that burns acetone and produces rotating columns of air using tangential air inlets.

Albini (1979) developed a model to predict the maximum distance that an ember can travel when released from a tree or a small group of trees. The model assumes a vertical plume structure within which the particle is lofted, before being advected by the ambient horizontal wind which is assumed to have a logarithmic velocity profile. A simple model of wind in non-flat terrain is also developed. The terminal velocity assumption is used. The model includes sub-models for the structure of the flame, the bouyant plume above the flame (matched with the flame sub-model at the flame tip), the burning rate of the ember, and the vertical transport of the ember within the three regions: the flame, the plume, and a transition region between these. The plume is assumed to exist until such time as the tree burns out, at which time it collapses. The author treats cylindrical embers only and a simple ember burning rate model is derived by assuming that the rate of mass loss is proportional to the rate of supply of air. A constant drag coefficient $C_{\mathrm{d}} = 1.2$ is assumed. Albini's model was developed for the field, using hand-held calculators and nomograms, but it has since been incorporated into the US Department of Agriculture's FARSITE wildfire modeling system.

Albini (1981b) extended the model of (Albini 1979) so that it applied to embers lofted by a continuous flame, such as a burning woodpile, rather than by a torching tree which burns out. The model was also extended to apply to the transport of embers over terrain not covered by forests, for example cut grass, bare ground or even water, where the friction length is small enough that the logarithmic velocity profile is not valid at the heights to which embers might be lofted, and where a 1/7 power law profile is more appropriate.

Albini further extended the work of (Albini 1979) to line fires: firstly by making an analytical study of the transport of embers lofted by line thermals (Albini 1983c),

in which it was found that the maximum ember lofting height was proportional to the square root of the *strength* (energy per unit length) of the thermal; and then by modelling the strength of thermals that can be produced by a line fire (Albini 1983a) based on work he did on the response of line fires to variability in wind speed (Albini 1982, 1983b).

Tse and Fernandez-Pello (1998) studied the trajectories of spherical metal particles and wooden embers released when high-voltage power lines arc or come into contact with nearby trees. They used the usual quadratic drag law (Equation (2.11)) with a drag coefficient dependent on Re,

$$C_{\mathrm{d}} = \begin{cases} \dfrac{24}{\mathrm{Re}}\left(1+\dfrac{3\mathrm{Re}}{16}\right)^{\frac{1}{2}} & \mathrm{Re} \leq 680 \\ 0.4 & 680 \leq \mathrm{Re} \leq 3\times 10^5, \end{cases} \tag{2.18}$$

and they assumed a horizontal wind field with a logarithmic vertical profile. Properties of the air, for example its density ρ (which arises in the computation of Re), are computed using the arithmetic mean of the particle temperature and the ambient air temperature. The justification for this is not clear. In the case of wooden embers they modeled the combustion of the embers as a pyrolysis front with an effective diameter, which represents the location of the front, given by

$$\frac{\mathrm{d}({D_{\mathrm{eff}}}^2)}{\mathrm{d}t} = -\beta \tag{2.19}$$

where $\beta = \beta_0(1+0.276\mathrm{Re}^{1/2}\,\mathrm{Pr}^{1/3})$, and Pr is the Prandtl number (Williams 1965). The constant β_0 was chosen to fit the data of Tarifa et al. (1967). The mass of the particle is then determined as $m_{\mathrm{e}} = \rho_{\mathrm{e},0}\pi {D_{\mathrm{eff}}}^3/6$. The numbers Re and C_{d} are not calculated from D_{eff} but from the actual particle diameter D, and this was modeled

by matching the expression

$$D_0{}^4 - D^4 = C\beta^2(t^2 - t_0^2) \tag{2.20}$$

with the data of Tarifa et al. (1967) by tuning the parameter C; a value of $C = \sqrt{3}$ was chosen. It is unclear how the form of Equation (2.20) was arrived at (cf. Eqn. (2.16)). Together, Equations (2.18), (2.19) and (2.20) give α as a function of t and enable Eqn. (2.11) to be numerically integrated, thus determining the trajectories of the embers. Note that the time scales here are smaller than in the case where embers are lofted by convection and the terminal velocity assumption is not appropriate, and was not used.

Woycheese et al. (1998) studied the lofting of spherical embers in a modified Baum and McCaffrey plume model (Baum and McCaffrey 1989), representing a house fire. They assumed that the plume velocity is vertical and everywhere equal to the centreline velocity, and that the horizontal wind is zero. They considered two cases: non-burning embers, and a burning droplet model of ember combustion that implies mass loss through reduction in the diameter of the ember only, i.e., density was assumed constant. They obtained formulae for the minimum height from which an ember could be lofted, and the maximum height that embers could attain depending on initial diameter and the intensity of the fire. They noted the existence of a critical particle diameter D_{crit} with all particles of diameter $D \geq D_{\text{crit}}$ achieving the same height before burnout. Woycheese et al. (1999) extended this work to include a non-zero horizontal wind which is assumed constant with height.

Anthenien et al. (2006) considered spherical, cylindrical and disc-shaped embers released at a given height, as in (Tse and Fernandez-Pello 1998), or lofted in a buoyant plume. Embers are assumed to burn until extinction, with mass at extinction denoted m_{ext}. Two values of m_{ext} are considered, 0 and 0.24, the latter being taken

from the data of Tarifa et al. (1967). After extinction the ember is assumed to cool by convection and radiative transfer. The combustion and aerodynamic properties of spheres were treated as in (Tse and Fernandez-Pello 1998) but using a slightly different expression for the spherical drag coeficient. The combustion of cylinders, with length l and diameter D, was treated in a similar fashion to that of spheres. Eqn. (2.19) was used for $D_{\rm eff}$, with the same value of β_0. However, the authors use heuristic reasoning to argue that, for cylinders, the constant $C = \sqrt{3}$ in Eqn. (2.20) should be $\sqrt{3}/(l/D)$, where l/D is the aspect ratio of the cylinder. This provides a good fit to the data of Tarifa et al. (1967), in which $l/D = 3$, but no real theoretical justification was offered. Although cylinders tumble in flight, the drag coefficient $C_{\rm d}$ is calculated as if they fall with their axis perpendicular to the relative velocity of the wind with respect to the ember, $\mathbf{w} - \mathbf{u}$, in line with other studies including that of Tarifa et al. (1965a). Burning discs are treated as cylinders with thickness l and diameter D, with a very low aspect ratio $l/D = O(10^{-2})$. It is assumed that they burn inward from the edges, so that

$$\frac{{\rm d}m_{\rm e}}{{\rm d}t} = \frac{\pi \rho_{\rm e} l}{4} \frac{{\rm d}({D_{\rm eff}}^2)}{{\rm d}t}.$$

By analogy with the cases of spheres and cylinders, Eqn. (2.19) is substituted leading to

$$\frac{{\rm d}m_{\rm e}}{{\rm d}t} = -\beta_0 (1 + 0.276 {\rm Re}^{1/2} {\rm Pr}^{1/3}) \frac{\pi \rho_{\rm e} l}{4}, \tag{2.21}$$

but the authors note that Eqn. (2.21) does not agree well with preliminary experimental data. Disc trajectories are calculated assuming the disc is in steady motion with its axis parallel to $\mathbf{u}_{\rm r}$, and $C_{\rm d}$ is calculated acordingly. The ambient wind is assumed to have a logarithmic vertical profile, and in the case of lofting they use a buoyancy dominated plume model tilted by the ambient horizontal wind. As in (Tse and Fernandez-Pello 1998), the properties of the air in the particle boundary

layer are calculated using the arithmetic mean of the particle surface temperature and the ambient air temperature. Two surface temperatures were used: 853K and 993K. The authors report that modeled travel distances do depend on the surface temperature of the particle because this effects both the density and the kinematic viscosity of the particle surface layer. They note an approximately 10% decrease in distance travelled when the temperature is increased from 853K to 993K for particles greater than 1mm in size.

Himoto and Tanaka (2005) used a LES to simulate the plume above a square heat source of characteristic size Δ in a turbulent boundary layer. The computational domain was sized $31\Delta \times 12.5\Delta \times 12.5\Delta$ with $124 \times 50 \times 50$ cells, not a very high resolution simulation. The upwind boundary conditions consisted of a time-dependent, pre-computed turbulent flow. Unlike the development in Section 2.3.2, the rotational motion of embers was considered, as was the lift force experienced by an ember. Square disc-shaped embers with side lengths D and thickness l were studied. The combustion of the embers was not modeled; they were considered to have constant mass and shape. Only one numerical simulation of the flow field was made, and this was used to compute the transport of embers of a number of sizes and aspect ratios. Embers were released at height Δ above the leeward edge of the heat source, randomly oriented but with the initial velocity and spin of the fluid at the point of release. Himoto and Tanaka derived the dimensionless parameter

$$B^* := \frac{v_\infty}{(g\Delta)^{\frac{1}{2}}} \left(\frac{\rho_\mathrm{e}}{\rho}\right)^{-\frac{3}{4}} \left(\frac{l}{\Delta}\right)^{-\frac{3}{4}} \left(\frac{\dot{Q}}{\rho c_\mathrm{p} T_\mathrm{a} g^{\frac{1}{2}} \Delta^{\frac{5}{2}}}\right)^{\frac{1}{2}} \tag{2.22}$$

where v_∞ is the mean inflow velocity above the surface layer, $\dot{Q}$ is the rate of release of heat, T_a is the ambient atmospheric temperature, c_p is the specific heat of air, and all other quantities are defined elsewhere. They found that the travel distance

of the embers was described by a log-normal distribution with

$$\frac{\mu}{\Delta} = 0.47B^{*2/3}, \quad \frac{\sigma}{\Delta} = 0.88B^{*1/3}. \tag{2.23}$$

Note the absence of the side length D of the embers in these expressions.

Sardoy et al. (2007) used a physics-based model to investigate the propagation of disc-shaped embers from crown fires. The fire model was run on a domain of $1000 \times 400 \times 500$ metres (l × w × h), with fuel beds of size $5 \times 5 \times 10$ metres and $5 \times 20 \times 10$ metres, based 3 metres above ground level, representing the canopies of fires with intensities 10 and 40 $\mathrm{MW\,m^{-1}}$ respectively. A logarithmic wind profile at the upwind boundary was assumed, with various wind speeds. The rate of pyrolysis in the fuel bed was adjusted to obtain the desired fire intensity and the model was run until a steady state was achieved. The output from the model, which includes plume velocities and temperatures, was then used to compute ember trajectories. The combustion of the embers was modeled as pyrolysis (leading to density loss) and char oxidation (which causes volume loss) using a physical model which was solved with an adaptive-mesh finite-volume method. As well as discs, the combustion model was applied to cylinders in order to compare results with available experimental data. In computing ember motion both lift and drag forces were considered, with the embers assumed to fly at an incidence angle of 145° to the relative wind velocity. For disc-shaped embers with thickness l the authors found the approximate relationship

$$d \propto I^{0.1}|\mathbf{w}|^{0.9}(\rho_{\mathrm{e},0} \times l)^{-0.2} \tag{2.24}$$

where d is ember travel distance and I is fire intensity, the other terms having

been defined earlier. The travel distance was reported to be insensitive to the initial diameter of the disc, which is in line with the findings of Himoto and Tanaka (2005).

Sardoy et al. (2008) studied the properties and landing distribution of disc-shaped embers generated by a line fire. They used an integral model of a line plume, the properties of which have a Gaussian distribution transverse to the plume. A 1/7-th power law was assumed for the vertical profile of the horizontal wind. Plumes were computed for a number of fire intensities and horizontal wind speeds. Embers were modeled as circular discs and their size, aspect ratio and initial position were generated randomly. The combustion of the embers was modeled as in Sardoy et al. (2007). Ember motion was considered to be two dimensional, and both rotation and lift were taken into account. Using dimensional analysis the authors derived a 'burning parameter' $\chi_0 = \rho_{e,0} {D_0}^{5/3} l_0^{-1/6}$ and based on their numerical results they reported the existence of a critical value of χ_0 above which an ember will land before burning out. This critical value depends also on the char content of the unburnt wood, the fire intensity and the wind speed. The authors found a bimodal distribution of landing distances for embers in which both pyrolysis and charring oxidation occurred, with the short-distance embers landing while pyrolysis was still occurring, and the long-distance embers landing during char oxidation. The parameter $\rho_{e,0}\, l_0$ controls whether the ember falls within the short or long-distance group.

Koo et al. (2012) performed very detailed modeling of ember transport using a computational fluid dynamics model coupled with a physical fire model, HIGRAD/ FIRETEC (Linn 1997). The simulations were performed on a $640 \times 320 \times 615$ metre domain with a horizontal grid spacing of 2 metres and a vertical grid size ranging from about 1.5 metres near the ground to about 30 metres at the model top. Both surface and canopy fires were simulated, and both were started as line fires 100

metres long and 2 metres deep. The study was performed with cylindrical ($l/D = 3$) and disc-shaped ($l/D = 1/9$) embers. While burning the embers were assumed to have a constant density, that of dried and charred wood. Their burning was modeled as flaming combustion only, and four types of size regression were studied: discs with radial regression, cylinders with axial regression, discs with axial regression and cylinders with radial regression. These were considered limiting cases; in the first two the change in size should have minimal effect on ember trajectories because the mass and all forces depend linearly on the dimension that is changing. Embers were launched from cells if the solid temperature and fuel densities exceeded certain critical values. The size of embers launched was the maximum loftable size based on the wind velocities prevailing at the cell, and a minimum size was set to eliminate embers too small to cause spotting. In the surface fire simulations, for comparison purposes, ember trajectories were computed with and without the terminal velocity assumption. There was a marked increase in travel distances without the terminal velocity assumption; average travel distances for the four types of size regression were 1.07 to 1.7 metres using the terminal velocity assumption, and these increased to 6.4 to 7.4 metres without that assumption. The authors attribute this to the embers being 'thrown by locally strong winds'. Because of the results from surface fires, the terminal velocity assumption was not used in the case of crown fires. For crown fires they noted that the largest and greatest number of embers were launched at the edges of the fireline, where the buoyant vertices are stronger than in the centre, but that the embers launched from the centre had the greatest travel distances.

Oliveira et al. (2014) investigated the transport of combusting cylindrical embers. They accounted for the rotational motion of the embers resulting from the centres of mass and pressure not coinciding, and calculated the lift and drag forces on the embers as they rotated. They found good qualitative agreement between their model and observations of non-combusting embers falling in still air. To model

ember combustion they used the semi-empirical models of Tse and Fernandez-Pello (1998) and Anthenien et al. (2006), based on the empirical data of Tarifa et al. (1965a, 1967), but they retuned the model parameters. They then modelled the short-range ($\sim$ 25 to 75 metre) transport of burning embers in a constant wind field with a logarithmic vertical profile; the embers were supposed to have previously been lofted by a bouyant plume. They found that the initial orientation of the embers had a significant effect on their travel distances.

Thurston et al. (2017) computed trajectories of non combusting 'embers' using the wind fields output from a LES of a plume generated by a static heat source in a turbulent boundary layer (Thurston et al. 2013). The model domain was $38.4 \times 19.2 \times 10$ kilometres with a 50 metre horizontal grid size and 256 vertical levels spaced from 10 metres at the surface to 50 metres higher up. Model runs were made using ambient horizontal wind speeds ranging from 5 to 15 $\mathrm{m\,s^{-1}}$. The model was spun up to a quasi-steady state before adding a static uniform circular heat source with flux 10^5 $\mathrm{W\,m^{-2}}$ and radius 250 metres at the bottom boundary. When the resulting plume was quasi-steady the model was run for a further 60 minutes, outputting wind field data every 5 seconds. These wind field data were used to compute the trajectories of particles released in a uniform distribution at heights of 50 to 100 metres above the heat source. The trajectories were computed under the terminal velocity assumption, with constant terminal fall speeds ranging from 5.0 to 9.0 $\mathrm{m\,s^{-1}}$. The terminal fall speed was the only characteristic of the embers that was used in the study. Mean travel distances distances were somewhat insensitive to increasing wind speeds, but maximum travel distances increased almost linearly with increases in wind speed, in accordance with the findings of Himoto and Tanaka (2005) and Sardoy et al. (2007); see Equations (2.22), (2.23) and (2.24). Thurston et al. (2017) found that, using a wind speed of 15 $\mathrm{m\,s^{-1}}$, particle travel distances of up to about 17 kilometres were obtained. The spatial distribution of particle landings decreased in width (transverse to the wind direction) as wind speed increased.

Chapter 3

Methods

3.1 Introduction

In this thesis extensive use has been made of the Weather Research and Forecasting (WRF) model (Skamarock et al. 2008) and the WRF-Fire coupled atmosphere-fire model (Coen et al. 2013; Mandel et al. 2011). They have been used to perform idealised simulations of fire-spread using flat topography, simple fuels maps with a single fuel type, simple atmospheric stability profiles, and with most physics options turned off in the model. This allows the main features under study to be isolated: dynamic fire behaviour, particularly in relation to fire-line geometry (Chapters 4 and 5). We also use WRF as a large eddy model (LEM) to simulate turbulent plumes, which are then used to study ember transport (Chapter 6). It was necessary to make some modifications to the standard WRF-Fire model; these are discussed in Section 3.4.

The WRF code is parallelised; intensive computational tasks, including all WRF and WRF-Fire simulations, were performed on the Raijin cluster at the National Computational Infrastructure (NCI). Pre- and post-processing of WRF and WRF-Fire data were handled with ad-hoc programs written in either Fortran or R (R Core Team 2017). R was used where possible, because of the ease of development,

the large library of packages that are available, and its excellent data-handling capabilities, including a very good netCDF interface (ncdf4, Pierce 2017). Most of the plots in this thesis were produced using the R package ggplot2 (Wickham 2009).

3.2 The Weather Research and Forecasting model

The WRF model is an open source atmospheric simulation model developed collaboratively by the National Center for Atmospheric Research (NCAR), National Oceanic and Atmospheric Administration (NOAA), the US Department of Defense, University of Oklahoma, and the Federal Aviation Administration. Its applications include numerical weather prediction (NWP), regional climate simulations, planetary atmospheric simulations, air quality modelling and idealised atmospheric simulations. WRF can be used at a range of scales, including as a large eddy model (LEM).

At the heart of WRF is the Advanced Research WRF (ARW) solver which solves the fully compressible Euler equations with moisture. It is a nonhydrostatic model with a hydrostatic option. The horizontal discretisation uses a staggered Arakawa C-grid, and the vertical discretisation uses a terrain-following hydrostatic-pressure-based coordinate (Section 3.4.3) which may be stretched to allow higher resolution near the surface. Full details of the model are available in (Skamarock et al. 2008).

The WRF model contains a full suite of physics sub-models including microphysics, cumulus parameterisations, surface layer and surface physics models, planetary boundary layer schemes and radiation physics.

WRF may be run in *real* or *idealised* mode. In real mode, the model uses the WRF preprocessing system (WPS) to ingest meteorological, topographic, and land-use data. In idealised mode, the user supplies an initial one-dimensional sounding which is assumed, by the WRF initialisation system, to represents an atmosphere in hydrostatic balance and which is used to compute the initial state of the atmosphere.

Simple topography may be introduced into an idealised simulation, but only by editing one of the Fortran files. See also (Section 3.4.3). After initialisation, the operation of WRF is controlled by a Fortran namelist file, `namelist.input`.

3.3 The WRF-Fire model

3.3.1 Overview

The WRF-Fire model is a fire module that has been added to the WRF package. WRF-Fire implements a two-way coupling between the WRF atmospheric model and a semi-empirical fire-spread model. The fire is represented on a two-dimensional grid (the *fire grid*) on which the distribution of fuel is defined and the location of the fire front maintained. The wind from the atmospheric model is interpolated to a user-defined height on the fire grid; this *fire wind* is the only input into the fire-spread model from the atmospheric model. A level-set method (Sethian 1999) is used to track the fire front using the one-dimensional fire-spread rates provided by the fire-spread model. A fuel map is supplied by the user, and assumptions about the burning rate of ignited fuel are used to calculate sensible- and latent-heat fluxes, which are input into the atmospheric model. These heat and moisture fluxes are how the fire-spread model influences the atmospheric model. The fire grid has a higher resolution than the horizontal resolution of the WRF atmospheric grid. This is desirable for two reasons: the horizontal resolution of the atmospheric grid is typically of the order of 10^1 - 10^2 metres which is too coarse to adequately represent variations in fuel or the evolution of the fire front; and a fire grid with too low a resolution causes large discontinuities in the heat fluxes input into the atmospheric model (Clark et al. 1996b). In the simulations presented in this thesis the resolution of the fire grid has been set at 10 times higher than the horizontal resolution of the atmospheric grid.

For the preparation of this thesis WRF-Fire was run in idealised mode; most physics options were turned off, and the topography was flat.

3.3.2 Fire-spread model

In theory, any (semi-)empirical fire-spread model could be used with WRF-Fire, provided that the WRF model can output the data required by the fire-spread model. In this study we used WRF-Fire configured to use the Rothermel semi-empirical fire-spread model (Frandsen 1971; Rothermel 1972). WRF-Fire uses a 13-category fuel-classification system (Albini 1976; Anderson 1982); fuel-dependent parameters required by the Rothermel model are determined by the applicable fuel category, as read from the supplied fuel map.

3.3.3 Tracking the evolution of the fireline

The Rothermel fire spread model is a one-dimensional model, providing an estimate of the heading rate of spread (the rate of spread in the direction of the wind). A front-tracking technique must be used to to track the two-dimensional evolution of the fireline. WRF-Fire uses a level-set method (Sethian 1999): a level-set function φ is used to represent the burnt area as $\{(x, y) : \varphi(x, y) \leq 0\}$. The fire front itself is given by $\{(x, y) : \varphi(x, y) = 0\}$. The evolution of φ is given by the equation

$$\frac{\partial \varphi}{\partial t} + S|\boldsymbol{\nabla}\varphi| = 0 \tag{3.1}$$

where S is the speed of propagation of a level set in the direction of its outward unit normal $\hat{\mathbf{n}} = \boldsymbol{\nabla}\varphi/|\boldsymbol{\nabla}\varphi|$. Eqn. (3.1) is often referred to as the *level-set equation*. (In practice, WRF-Fire uses the equation $\partial\varphi/\partial t + S(|\boldsymbol{\nabla}\varphi| - \varepsilon\Delta\varphi) = 0$, where $\Delta\varphi = \delta x\, \partial^2\varphi/\partial x^2 + \delta y\, \partial^2\varphi/\partial y^2$. The term $\varepsilon\Delta\varphi$ is an artificial viscosity included

for numerical stability; δx and δy are the grid resolutions, and $\varepsilon > 0$ is a small, grid-independent constant.) S is obtained from the Rothermel model by inputing the component of the fire wind in the direction of $\hat{\mathbf{n}}$. This is the only input into the fire-spread model from the atmospheric model. The level-set function φ is maintained on the fire grid and is available as an output. For full details see (Mandel et al. 2011). The level-set formulation is convenient because it easily handles topological difficulties such as those arising from the merging of separate fire fronts and the creation of islands of unburnt fuel. It also enables the easy computation of the fire-line curvature directly from φ; see Eqn. (5.1).

3.3.4 Feedback to the atmospheric model

WRF-Fire assumes an exponential decrease in fuel mass after ignition. It computes the fraction of fuel remaining in a fire-grid cell at time t by making an estimate of

$$F(t) = 1 - \frac{1}{\text{cell area}} \iint\limits_{\text{cell},\varphi(x,y,t)\le 0} 1 - \exp\left(\frac{-T(x,y,t)}{\tau}\right)\, dxdy \tag{3.2}$$

where $T(x, y, t)$ is the time since ignition of the point (x, y), and τ is a constant that characterises the burn-down time of the fuel. At each time step WRF-Fire computes the fraction of fuel that was consumed, and the resulting sensible heat and latent heat (moisture) fluxes. The fluxes from each fire cell are summed to the horizontal grid of the atmospheric model, and the sensible and latent heat is distributed into the lower part of the atmosphere via the potential-temperature and water-vapour prognostic equations. These sensible and latent heat fluxes are the only ways in which the fire model influences the atmospheric model.

3.4 Modifications to WRF-Fire made for this research

3.4.1 Unlimited number of ignition lines

A fire is initialised (ignited) in WRF-Fire on a straight line segment, which may be degenerate (i.e. a point). At the time of writing, the standard version of WRF-Fire released by NCAR had a limit of five ignition segments, specified in the file `namelist.input`. For this research it was necessary to be able to specify an unlimited (but finite) number of ignition segments. Modifications were made to the code to facilitate this, and to allow the ignition segments to be read from a user-specified ignition file. This allowed the simulation of fires ignited along a curved initial fireline by specifying a large number of short chords. It also facilitates the easy generation of randomly oriented initial firelines by the automatic generation of ignition files.

3.4.2 Defining a static heat source

This modification allows a user to specify a static heat source. The extent of the heat source is determined by the region of fuel specified in the fuel map file `input_fc`. The values of the sensible and latent heat fluxes are specified by new namelist variables in the `fire` namelist, in the file `namelist.input`. The modification involves changes to the subroutine `heat_fluxes` in the file `module_fr_fire_phys.F`; the sensible and latent heat fluxes for each cell of the fire grid are set according to the values of the new namelist variables, rather than being computed using the procedure outlined in Section 3.3.4. This modified code was used in Section 5.5 to simulate in WRF the radial wind field produced by a static circular heat source, and to produce a turbulent plume in the ember transport studies described in Chapter 6. This code has also been used by Badlan et al. (2017) to study pyroconvection. It should be noted that when WRF-Fire is run with this modification there is only a one-way coupling between the 'fire' and the atmosphere; the heat source is static and is not

affected by the state of the atmosphere. The full machinery of the WRF-Fire code is not being used, and this modification is really only a convenient way of introducing sensible and latent heat flux anomalies into the WRF atmospheric model using the WRF-Fire code.

3.4.3 Specification of vertical coordinates in terms of height AGL

The vertical coordinate system used in WRF is a terrain-following pressure-based coordinate system defined by

$$\eta = \frac{p_{\mathrm{h}} - p_{\mathrm{ht}}}{p_{\mathrm{hs}} - p_{\mathrm{ht}}}$$

where p_{h} is hydrostatic pressure, and p_{hs} and p_{ht} are the hydrostatic pressure at the surface and the model top respectively (Skamarock et al. 2008). Thus η varies from 1 at the surface to 0 at the model top. To set up an idealised simulation, the user specifies the number of vertical levels in `namelist.input` and supplies WRF with a sounding file, `input_sounding`, which specifies the pressure, potential temperature and moisture mixing ratios at the surface, and a sequence of values, at specified heights, for potential temperature, vapour mixing ratio, and horizontal components of wind velocity. This can be any set of values at levels extending to at least the model top. The standard WRF initialisation routine defines a convenient set of η-levels and, in each column of the computational domain, computes an initial atmospheric state based on values interpolated from those specified in `input_sounding`. However, it is often convenient to control the vertical resolution of the model by specifying the (initial) heights of the vertical coordinate levels. Modifications were made to the code so that the η-levels were computed from the sequence of heights given in `input_sounding`. This requires `input_sounding` to contain the same number of levels as that specified in `namelist.input`. Initially, the vertical coordinate surfaces will be located at the heights given in `input_sounding`, but because the

vertical coordinate is based on pressure, the exact heights of the coordinate surfaces will vary with time and horizontal location during a simulation.

3.5 The pyrogenic-potential model

In this thesis we will present some results comparing the simulation output of WRF-Fire with the pyrogenic-potential model recently developed by Hilton et al. (2018). This model represents the near-surface wind field as a two-dimensional potential flow. Based on the idea that surface air is entrained into the plume, the flaming regions represent sinks in the horizontal near-surface flow. In the form of the model described here, the wind field $\mathbf{w} = (u, v, w)$ is assumed to be irrotational ($\boldsymbol{\nabla} \times \mathbf{w} = \mathbf{0}$) and incompressible ($\boldsymbol{\nabla} \cdot \mathbf{w} = 0$). This implies that $\mathbf{w} = \boldsymbol{\nabla}\psi$ where ψ solves Laplace's equation $\boldsymbol{\nabla}^2\psi = 0$. It is assumed that the near-surface wind field is horizontal (i.e. $w = 0$) away from the burning area. Since $\partial_x u + \partial_y v + \partial_z w = 0$, we may write

$$\partial_x u + \partial_y v = \begin{cases} -\partial_z w \text{ above the burning area,} \\ \qquad 0 \text{ elsewhere,} \end{cases}$$

or, $\mathbf{w}_h = \boldsymbol{\nabla}\psi_{\mathrm{h}}$, where $\boldsymbol{\nabla}^2_{\mathrm{h}}\psi_{\mathrm{h}} = \nu$, $\nu = -\partial_z\psi$, and the subscript h indicates an operation or variable restricted to the near-surface horizontal plane. Thus, in this plane, ψ_{h} solves a two-dimensional Poisson equation where the source (actually, sink) term ν is non-zero only in the burning region. For convenience we will drop the subscript h and write

$$\boldsymbol{\nabla}^2\psi = \nu \tag{3.3}$$

and $\mathbf{w} = \boldsymbol{\nabla}\psi$, where it is understood that we are now working in the near-surface plane. There exist very efficient numerical methods for solving Eqn. (3.3). The sink term ν represents the movement of buoyant air away from ground, and is assumed to be related in some way to the intensity I of the fire.

This is a linear model, so that a spatially-homogeneous ambient wind field $\mathbf{w}_a = (u_a, v_a)$ can simply be added to the solution $\mathbf{w}$ of Eqn. (3.3); if ψ solves Eqn. (3.3) then so does $\psi + u_a x + v_a y$, and $\boldsymbol{\nabla}(\psi + u_a x + v_a y) = \mathbf{w} + \mathbf{w}_a$.

Assume that the relationship $\nu = f(I)$ is known. If $I(t)$ is known at any particular time t during the evolution of the fire then the equation $\boldsymbol{\nabla}^2\psi = f(I(t))$ can be solved, and the induced wind field, $\mathbf{w} = \boldsymbol{\nabla}\psi$, may be input into a one-dimensional fire-spread model to compute the rate of spread in the normal direction to the fire front. A front-tracking method can be used to compute the location of the front at time $t+\delta t$, whereupon $I(t+\delta t)$ can be calculated, and the process may be iterated. This provides a simple and very computationally efficient coupled model. The pyrogenic-potential method is agnostic as to the particular front-tracking technique employed, and to the fire-spread model used, although the wind field is the only atmospheric variable that will be available to the fire-spread model. It should be noted that if an empirical or quasi-empirical fire-spread model is used then the coupled model has the same shortcoming discussed in Section 1.6.5: such fire-spread models are calibrated using ambient wind speeds, for example those that exist in a wind tunnel before a fire is ignited, whereas in a coupled model, the wind that is input to the fire component is a combination of the ambient and fire-induced winds.

The pyrogenic-potential model has been implemented in the Spark framework (Miller et al. 2015), which uses a level-set method for front tracking. In (Hilton et al. 2018) a simple fire spread model of the form

$$S = u_0 + u_1 \max(\mathbf{w} \cdot \hat{\mathbf{n}}, 0) \tag{3.4}$$

was coupled to the pyrogenic-potential model, where $\hat{\mathbf{n}}$ is the outward unit normal to the front, u_0 and u_1 are model parameters, and S is the speed of the front in the normal direction (see Eqn. (3.1)). However in this thesis, to provide a direct

comparison with WRF-Fire, we use the Rothermel model, (Rothermel 1972) as implemented in WRF-Fire.

Fire intensity is calculated assuming an exponential decay of fuel mass once an element of fuel is ignited. Thus if M_0 is the initial fuel load ($\mathrm{kg\,m^{-2}}$) then it is assumed that the fuel load M at time t is

$$M = M_0 e^{-(t-t_\mathrm{i})/\tau}$$

where $t_\mathrm{i} \leq t$ is the time of ignition, and τ characterises the rate of burning of the fuel (cf. Eqn. (3.2)). The fire intensity I is then given by

$$I = -H\frac{\partial M}{\partial t} = \frac{HM_0}{\tau} e^{-(t-t_\mathrm{i})/\tau} \tag{3.5}$$

where H is the heat released per unit mass of fuel burnt. This is essentially the same as the computation of the heat fluxes in WRF-Fire (Section 3.3.4). It differs from the calculation of I in (Hilton et al. 2017; 2018), which use a smeared, two-dimensional version of the one-dimensional Byram fireline intensity I_B (Byram 1959):

$$I_\varepsilon(\mathbf{x}) = \int_{\text{fireline}} \delta_\varepsilon(|\mathbf{x} - \mathbf{x'}|) I_\mathrm{B}(\mathbf{x'}) d\mathbf{x'} \tag{3.6}$$

where $\delta_\varepsilon(r) = 2\varepsilon/(e^{\varepsilon r} + e^{-\varepsilon r})^2$ is a smoothed Dirac delta function.

The assumption that the flow is irrotational is a significant one, and the model could be extended to accommodate vorticity but, according to Hilton et al. (2018), irrotational flow seems sufficient to approximate the dynamic behaviour seen in experiments.

One critical component of the model lies in specifying the relationship between the sink term ν and the intensity I. In (Hilton et al. 2017; 2018) it was assumed that $\nu = kI_\varepsilon$ (see Eqn. (3.6)) with k a free parameter. This should only be considered as a first approximation, and research into developing a useful form for $\nu = f(I)$ is ongoing.

The linearity of the model may also prove to be a difficulty; the phenomena themselves are almost certainly highly non-linear. However it is hoped that the model can provide a significant improvement over the current empirical fire-spread models, and a useful first-order approximation to more complex and computationally-expensive coupled atmosphere-fire models.

Chapter 4

Modelling of junction fires

4.1 Introduction

The dynamic fire behaviour resulting from the interaction between two merging straight-line fires (called a 'jump fire' or 'junction fire') has been studied by Viegas et al. (2012), Sharples et al. (2013), Thomas et al. (2015, 2017b), Sharples and Hilton (2017), and Raposo et al. (2018). It involves an initial very rapid increase in rate of spread, with a subsequent slowing; this is an example in which rapid changes in fire behaviour occur without any change in ambient conditions. Viegas et al. (2012) and Raposo et al. (2018) studied this behaviour both analytically and using laboratory-scale experiments. Sharples et al. (2013) and Sharples and Hilton (2017) were able to reproduce qualitative aspects of this behaviour using a simple fire spread model in which the rate of spread depended on the curvature of the fireline. In this chapter we present a study of the junction fire phenomena using the WRF-Fire coupled atmosphere-fire model. The study of the behaviour of junction fires is of interest for at least two reasons: it gives insight into the way separate fires merge, for example in spot-fire coalescence; and the rapid acceleration of the region of a fireline between tow merging fronts is of interest to operational personnel.

Much of the material presented in the chapter was published in (Thomas et al. 2015, 2017b).

4.2 Model setup

For the study of junction fires, WRF-Fire was used in idealised mode in a domain of $6400 \times 6400 \times 3000$ metres (length $\times$ width $\times$ height), with a horizontal resolution of 20 metres (atmospheric grid) and 2 metres (fire grid). A stretched vertical coordinate was used with 61 levels, initially spaced at approximately 4 metres at the surface, increasing to about 70 metres at 1 kilometre above ground level (AGL), and 140 metres at the model top. WRF uses a vertical coordinate based on pressure (Skamarock et al. 2008) and, when expressed in terms of length, vertical resolution varies during a model run. However, in practice, the vertical spatial resolution did not vary significantly in this study: for all simulations, vertical coordinate surfaces, and time steps, the maximum variation in height of a coordinate surface from its initial value was on average 1.7%, and never exceeded 13.1%. The lowest level at which horizontal winds were computed was located approximately 2 metres AGL. For input into the fire spread model, horizontal winds were extrapolated to 1 metre AGL and interpolated horizontally to the finer fire grid; they were used at points on the fireline to compute the local rate of spread.

The model was initialised with no moisture and with a vertical temperature profile consisting of a 1000-metre-deep dry-adiabatic layer at a constant potential temperature of 300 K, topped by a stable layer with potential temperature increasing at 4.5 K per kilometre to the model top at 3 kilometres. A surface roughness length of 0.1 metres was assumed, corresponding to very long grass or low crops (Wieringa 1992). (The surface roughness indicates the depth of the atmosphere that is affected directly by surface drag.) The model does not capture the effect that changes in the vegetation (after combustion) will have on the surface winds input into the

fire-spread model. While this is a shortcoming of the model, in this thesis we are interested in the effect of larger-scale convective processes.

Four ignition configurations were studied, corresponding to those used in the experiments of Viegas et al. (2012): two oblique firelines forming a 'V' shape (the junction) with included angles of 10°, 20°, 30° and 45°. Each fireline was 1000 metres long, in contrast to less than 10 metres in the experimental work of Viegas et al. (2012), and the firelines were positioned in the centre of the computational grid. The fuel type was taken to be 'long grass' which is Category 3 of the fuel classification system of Albini (1976) and Anderson (1982). The fuel parameters used by the Rothermel fire-spread model were the standard ones specified in the parameter files supplied with WRF-Fire. Fuel was confined to the triangular region formed by the junction of the initial firelines, and an additional 10 metre buffer region. This value of 10 metres is the same as that specified for the fire ignition radius in the WRF-Fire parameter list; every pixel of the fire grid within this distance is ignited during the fire initialisation.

Most of the simulations were made with no wind, in keeping with the experiments of Viegas et al. (2012). However a limited number of simulations were made with an initial ambient wind, which in each case was aligned with the axis of the junction and directed away from the apex of the junction, towards its open end. All numerical experiments were performed with flat topography.

In each case the atmospheric model was run for 20 minutes of model time (an arbitrary period), before the arms of the junction were ignited at once over their entire length, which is how the experiments of Viegas et al. (2012) were conducted. After ignition, the model was run for a further 45 minutes. Based on results from a preliminary study (Thomas et al. 2015), the study of Thomas et al. (2017b) was performed with a high horizontal resolution (20 metres), using small five-member

ensembles in which the orientations of the initial firelines have been determined randomly. Separate ensemble members were considered because the effects of domain discretisation cause the results of the simulations to vary slightly, depending on the orientation of the initial firelines with respect to the horizontal grid alignment. For each random orientation, three simulations were performed: one with both firelines (i.e. arms of the junction) ignited simultaneously; and two in which just one of the firelines was ignited. We interpret the composite results of the latter two runs as an indication of how the junction fires would evolve if neither fireline had an influence on the behaviour of the other.

WRF-Fire uses a level-set method (Section 3.3.3) to follow the evolution of the fire front, and it outputs the values of the level-set function φ on the high-resolution fire grid. These data were used in post processing to determine the location of the fire front, which is given at time t by $\{(x, y) : \varphi(x, y, t) = 0\}$, the zero contour of $\varphi(\cdot, \cdot, t)$. The rate of spread, which at a point on the front is the rate of spread in the direction normal to the front, is output by the WRF-Fire model at each point of the fire grid; it was estimated on the zero contour by linear interpolation.

4.3 Results

4.3.1 Experiments with no ambient wind

Figure 4.1 depicts isochrones at two-minute intervals, showing the first 44 minutes of the evolution of the fireline of one ensemble member for each configuration angle; approximate rates of spread can be inferred from the distances between successive isochrones. While these are just four of twenty similar model runs (four included angles $\times$ five ensemble members), they represent the typical behaviour seen in all the simulations: there is a rapid initial acceleration of the fire front in the region where the two firelines intersect, followed by a subsequent slowing, consistent with the behaviour reported by Viegas et al. (2012). In Figure 4.1 there are random

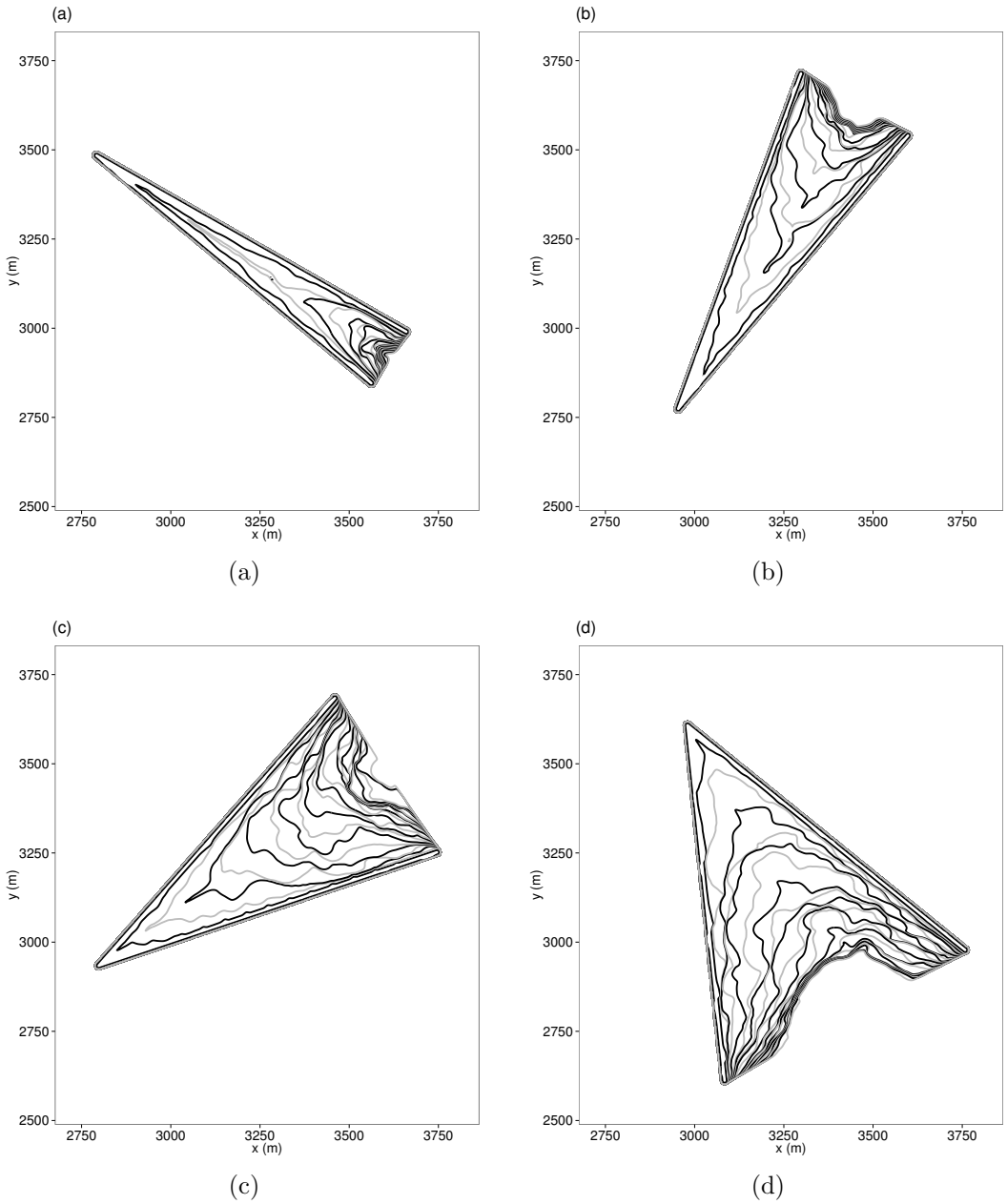

Figure 4.1: Simulated isochrones of fire spread for one member each of the (a) 10°, (b) 20°, (c) 30°, and (d) 45° angular configurations tested. Firelines, depicted alternately in black and grey, are shown at 2-minute intervals. X and Y axes show locations of the burn within the simulation grid, which was necessarily considerably larger than the experimental fire area. Each fire was started with both arms of the initial junction ignited simultaneously along their entire length. Simulations for each angle were repeated five times using randomly chosen orientations. Fire advance and burn duration are shown in Figure 4.2 for all examples of each angular configuration.

departures from symmetry which can be attributed to numerical instability and noise in the simulations. In addition, a slight systematic asymmetry in the evolving firelines is evident, particularly during the initial time steps in panels (c) and (d). These simulations were performed assuming no ambient wind, and we attribute this asymmetry to an effect of the discretisation of the model; the branch that is more closely aligned with the grid seems to spread more rapidly during the early period of the simulations. There is no systematic asymmetry in model output when the initial firelines are oriented symmetrically with respect to the grid. This slight asymmetry occurs to varying degrees in the simulations that we have performed. Because it is slight, and to maintain some consistency between the current analysis and that of Viegas et al. (2012), we summarise the advance of the front by the location of its central point, i.e. its intersection with the axis of symmetry of the initial 'V'. In the simulation depicted in Figure 4.1(c), for example, this central point advances more than 690 metres in the first 15 minutes after ignition, and only approximately 170 metres in the subsequent 10-minute interval. Fire advance as a function of burn duration is shown in Figure 4.2 for all examples of each angular configuration. The black lines in Figure 4.2 depict the advance of the (centre of the) fire front for all 20 of the simulations in which both firelines were ignited. The rapid initial acceleration, and subsequent slowing, of the front are evident in all cases. The behaviour of the simulations with different configuration angles is qualitatively similar. However, from Figure 4.2, the smaller the configuration angle, the more rapid is the initial advance of the centre of the front. An effect like this is to be expected on purely geometric grounds: if the angle between the fronts is θ then, in a perfectly uniform situation, the centre of the front will advance by a factor of $\csc\theta$ faster than the normal rate of spread of the merging fronts. A comparison of the black and grey lines in Figure 4.2 shows that this geometric effect does not entirely account for the rapid initial fire spread.

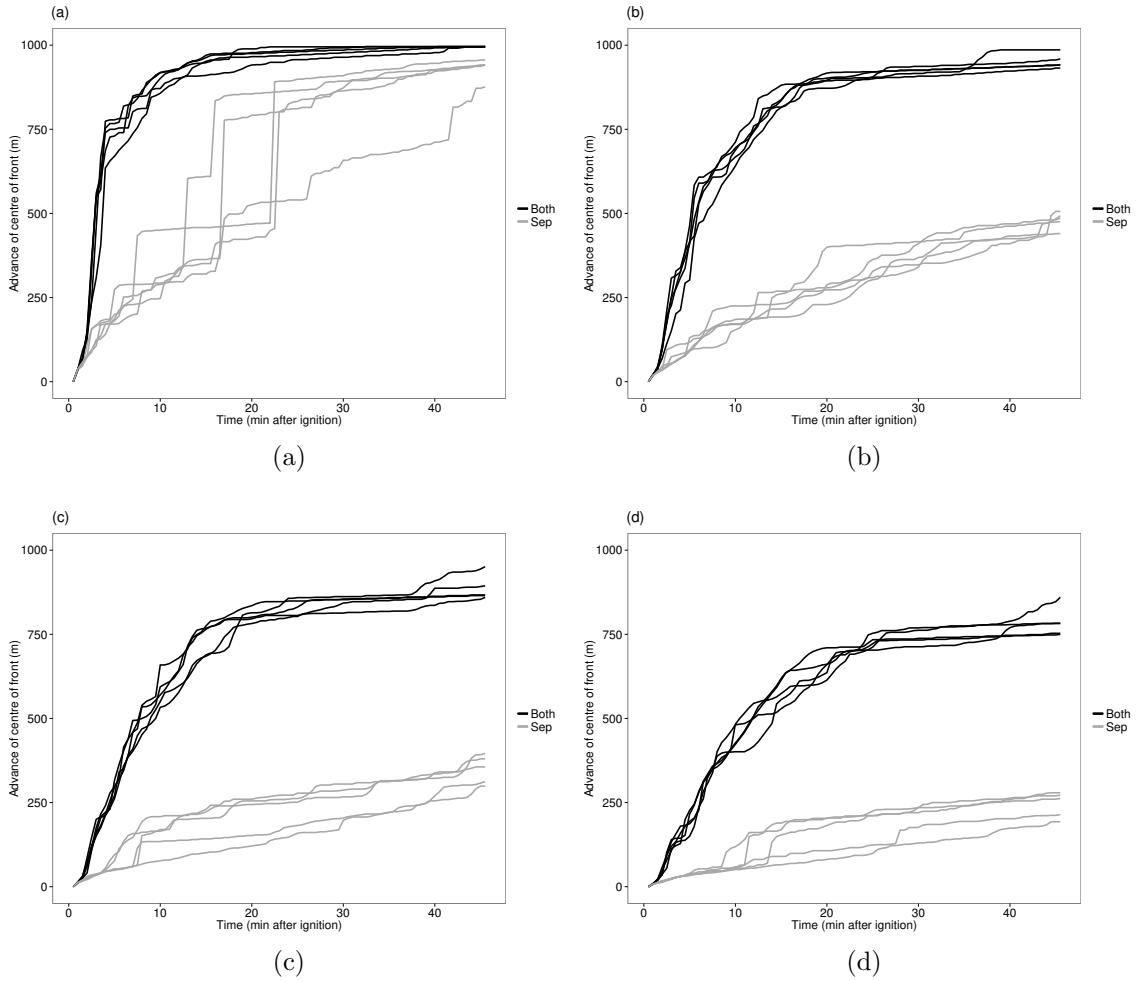

Figure 4.2: Fire front advance over time for all ensemble members for the four geometric configurations: (a) 10°, (b) 20°, (c) 30°, and (d) 45°. Distance advanced is measured along the axis of symmetry of the junction. Black lines (labelled 'Both') represent spread when both arms of the junction are ignited simultaneously; grey lines (labelled 'Sep') indicate spread when each arm is ignited separately (see Figure 4.4).

4.3.2 Comparison with previous experimental and analytical work

In their study of this phenomenon, Viegas et al. (2012) treated the merged fire front as a pair of straight firelines evolving from the initial 'V'-shape by a rotation about the endpoints of the 'V'. Figure 4.1 indicates that this is a reasonable first-order approximation in the case of these simulations; the results of the other simulations (not shown here) also indicate that this is a reasonable first-order approximation. Thus, to make comparisons with the work of Viegas et al. (2012), we approximate

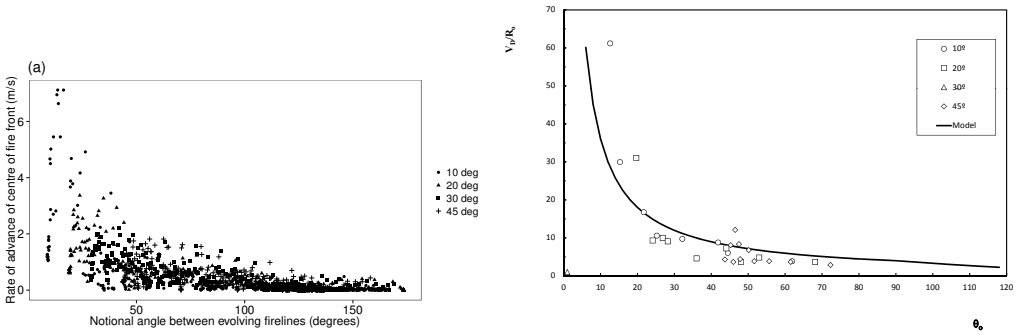

(a) (b)

Figure 4.3: (a) Rate of advance of the centre of the modelled fire front versus the notional angle between evolving firelines for all simulations, output at 30-second intervals. The centre of the fire front is determined as the intersection of the front with the axis of symmetry of the initial junction configuration. The notional angle between firelines is the angle at the centre of the front subtended by the endpoints of the initial junction. (b) Fig. 18 from Viegas et al. (2012): non-dimensionalised velocity of centre of front versus angle between the firelines. The points represent experimental results; the solid line represents the results of the analytical model (reproduced with permission from CSIRO Publishing).

the evolving fire front as a pair of straight line segments extending from the endpoints of the initial 'V' to the central point of the simulated front. Figure 4.3(a) is a plot of the rate of advance of the centre of the fire front against the angle formed by the approximating straight firelines; Figure 4.3(b) is reproduced from Viegas et al. (2012). There is good qualitative agreement between the two, however they do not agree quantitatively. The vertical axis of Figure 4.3(b) represents a non-dimensionalised velocity obtained by dividing by the base rate of fire spread without wind or slope. Even if we were to non-dimensionalise the rate of advance in Figure 4.3(a) in the same fashion, we would not have quantitative agreement with Figure 4.3(b). This is not surprising given the considerable difference in scale between the experiments of Viegas et al. (2012) and our numerical modelling.

4.3.2.1 Effects of fire-fire interaction

Figure 4.4 is a composite plot of three simulations with the same configuration, showing the difference in the evolution of the firelines when both arms of the junc-

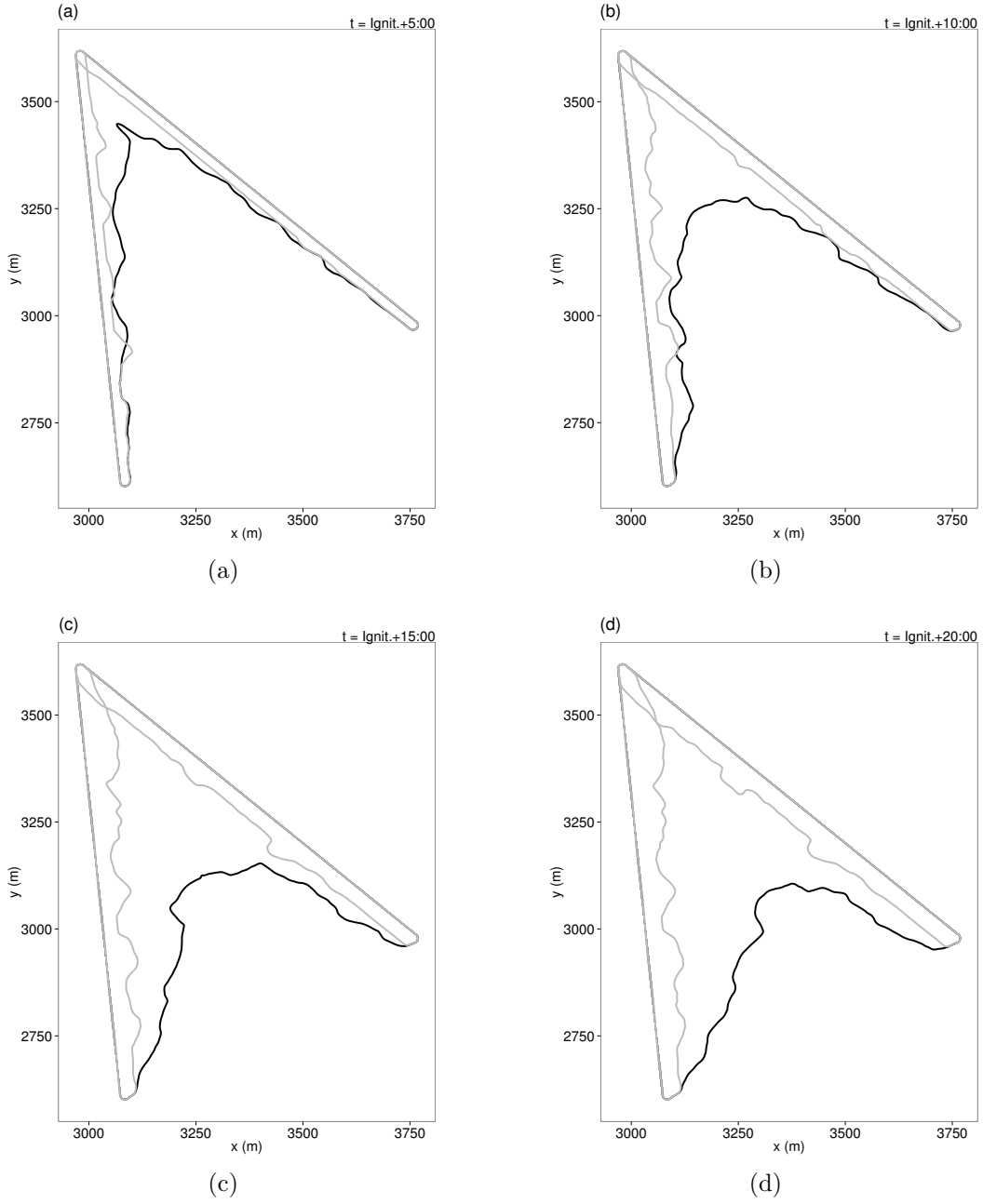

Figure 4.4: Composite plot of three model runs with a 45°configuration, shown (a) 5, (b) 10, (c) 15, and (d) 20 minutes after ignition. The grey lines show the evolution of the front when only one arm of the junction is ignited; together they show how the front would evolve without interaction between the two firelines. The black line shows the evolution when both arms are ignited simultaneously.

tion are ignited compared with when they are ignited separately. This figure illustrates the effects of the interactions between the two firelines on the rate of spread

(alternatively, this can be interpreted as the influence that the geometry of the fireline has on the rate of spread). The behaviour illustrated in Figure 4.4 is typical of all simulations; the grey lines in Figure 4.2 show the advance of the central point of the front for all ensemble members in which the firelines are ignited separately, as is the case for the grey firelines in Figure 4.4. The contrast between the black and grey lines of Figure 4.2 shows the dramatic effects of the interactions between the two firelines.

4.3.3 Sensitivity of the simulations to initial orientation

Figure 4.2 shows that when both firelines are ignited (the black lines), the results are not particularly sensitive to the initial orientation of the firelines. The noise in the grey lines is an artefact of the way that the advance of the front is summarised as its intersection with the axis of symmetry of the initial junction. When ignited separately, the firelines in the simulations do not evolve in a perfectly regular way; see for example the bulges in the grey lines in Figure 4.4. When these bulges intersect the axis of symmetry, they result in sudden jumps in the location of the intersection point. This is particularly evident in Figure 4.2(a), where the small initial angle amplifies this effect. An alternative way of displaying the advance of the fire front is displayed in Figure 4.5, which shows area burnt versus time for all the ensemble members. This way of displaying the advance of the fireline is not as noisy as using the location of the centre of the front.

4.3.4 Underlying mechanism

What is the mechanism that drives this dynamic fire behaviour? Viegas et al. (2012) made an analytical study of it in terms of the 'concentration of energy near the intersection point' of the two firelines, arising from radiative and convective heat transfer. The Rothermel model, the basis of the fire-spread sub-model in WRF-Fire, is derived using the all-encompassing notion of a 'propagating flux' to represent the

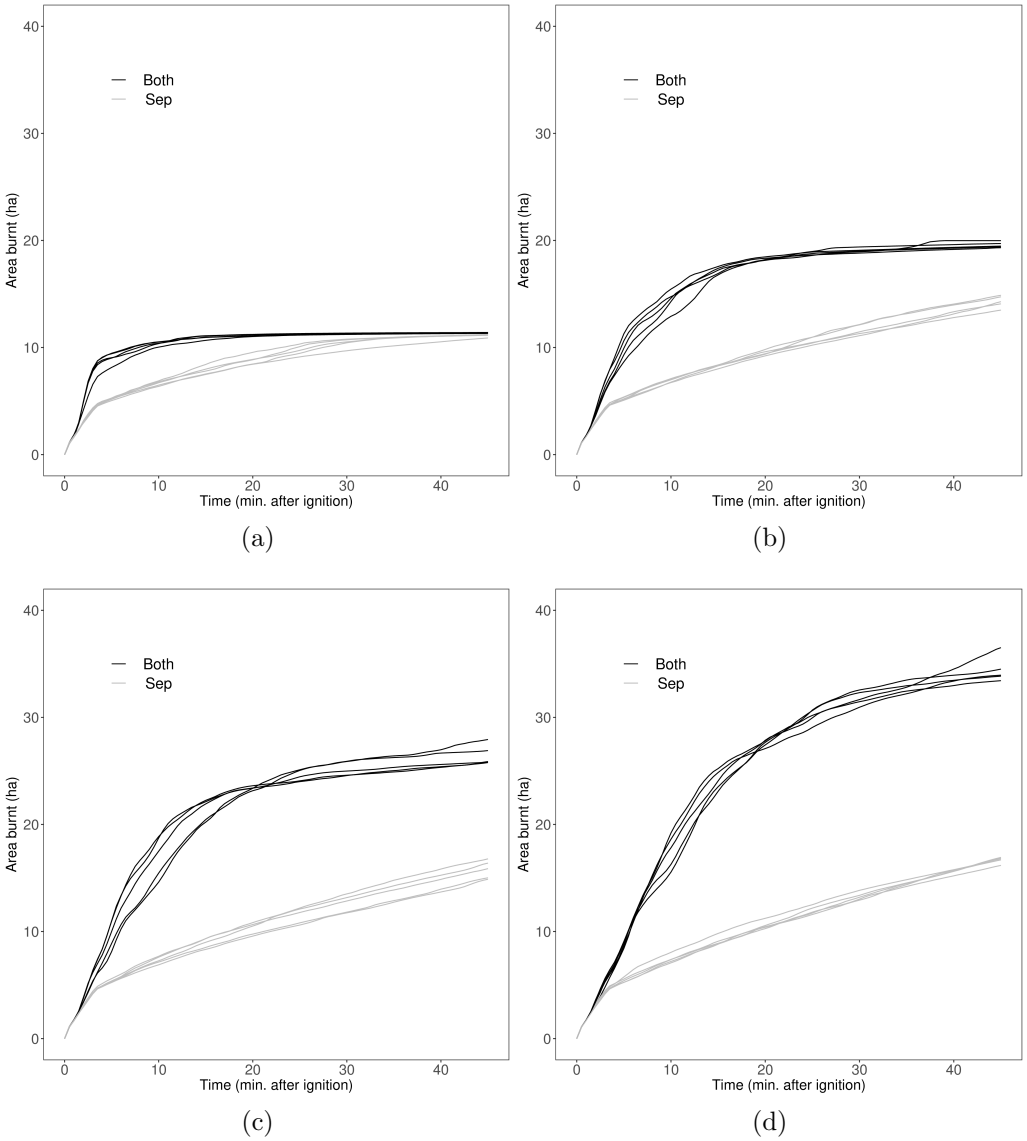

Figure 4.5: Area burnt versus time for all ensemble members for the four geometric configurations: (a) 10°, (b) 20°, (c) 30°, and (d) 45°. Black lines (labelled 'Both') represent burnt area when both arms ignited simultaneously; grey lines (labelled 'Sep') indicate burnt area when each arm is ignited separately (see Figure 4.4).

transmission of energy ahead of the front (Rothermel 1972). However, there is no explicit radiation component in the WRF-Fire model; under conditions of constant fuel and slope the modelled rate of spread depends only on the wind at a prescribed height (1 metre AGL in this case). Consequently, the dynamic behaviour observed in our numerical experiments can only be a result of the surface winds induced by the modelled pyro-convective processes. This accords with the analysis of Raposo et al.

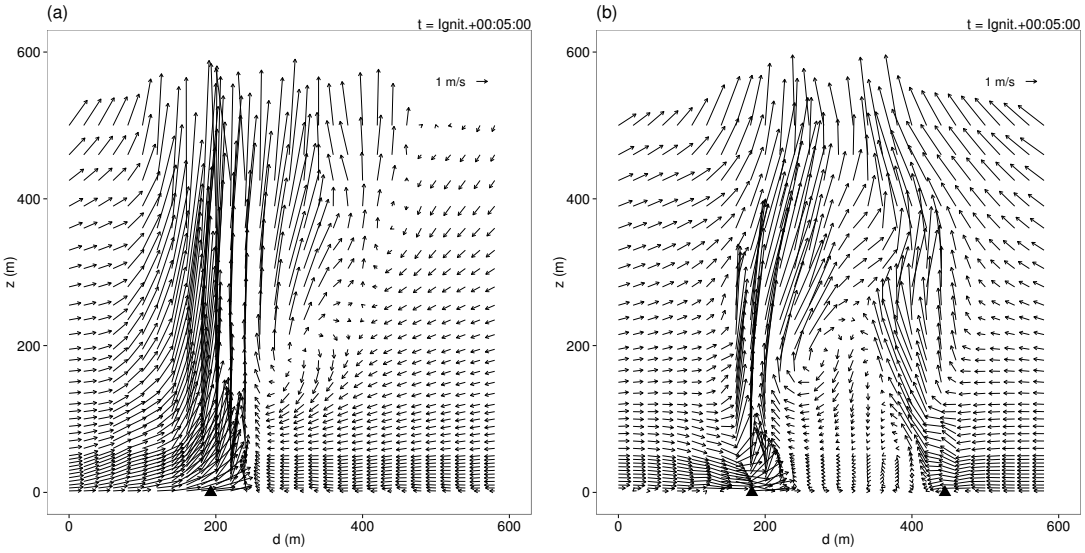

(a) (b)

Figure 4.6: Bottom 500 metres of the wind field along (a) transect L_1:R_1, and (b) transect L_2:R_2 shown in Figure 4.7. The arrows indicate the projection of the wind field onto the vertical plane of the transect. The location of the fireline on the transect is shown by the solid triangles.

(2018) who conclude that 'important convective processes are ... responsible for the dynamic behaviour of junction fires.' Figure 4.6 shows the component of the bottom 500 metre of the wind field for the ensemble member depicted in Figure 4.1(d), 5 minutes after ignition, along the transects indicated in Figure 4.7. (In the following discussion all references to winds refer to the component of the wind field in the vertical plane of the transect.) Figure 4.6(a) corresponds to the transect L_1:R_1; the location of the fireline is indicated by the solid black triangle. Apart from the region immediately ahead of the fireline, the near surface wind speeds in front of the fire are lower than those behind it (recall that the ambient wind speed is zero). Similarly, in Figure 4.6(b), corresponding to the transect L_2:R_2 of Figure 4.7, near surface wind speeds ahead of the firelines (i.e. between the firelines) are, for the most part, lower than those behind the firelines. Recent work of Hilton et al. (2018) shows that, under some simplifying assumptions, the bulk surface flow induced by a fire can be modelled with a simple analytical model, and that this surface flow is strongly influenced by the geometry of the fireline. This simple model indicates why the

near-surface wind speeds in Figure 4.6 are, for the most part, higher behind the fireline than they are ahead of it; it is a result of the shape of the fireline. Another feature of Figure 4.6 is of interest: the separation zone in Figure 4.6(a), where the near-surface wind field is entrained into the plume, is located ahead of the fireline, and at the fireline the surface wind speed in the direction of fire spread is higher than the near surface wind speeds behind the fireline. In Figure 4.6(b), the wind fields behind the left and right firelines are quite similar, however the surface wind fields at the firelines are very different. The left-hand separation zone is again advanced ahead of the fireline, with higher surface winds in the direction of fire spread, whereas on the right, the surface winds at the fireline are low.

More insight can be obtained by examining Figure 4.7, which shows the surface wind field and a smoothed representation of the vertical component of vorticity at 10 metres AGL of the ensemble member corresponding to Figure 4.1(d), 5 and 10 minutes after ignition. (Recall that the vorticity of a fluid with velocity field $\mathbf{w}$ is defined as $\boldsymbol{\omega} = \boldsymbol{\nabla} \times \mathbf{w}$; it is a measure of the rotation of the flow.) Among the notable features are the pairs of counter-rotating vortices (only the vertical component is shown) associated with those parts of the fireline with highest rates of spread. These lie on or just ahead of the fireline, and are oriented so as to induce surface winds that advance the fire front (negative vertical vorticity implies clockwise rotation in the diagram, positive implies counter-clockwise rotation). Note that the transect L_1:R_1 in Figure 4.7(a) passes through such a pair at the fireline, as does the left-hand part of the transect L_2:R_2. By contrast, the right-hand part of L_2:R_2 passes through a region of low vorticity at the fireline. The advancement of the separation zone ahead of the fireline, the increased surface winds in the direction of the rate of spread, and the consequent higher modelled rates of spread are associated with these vortex pairs.

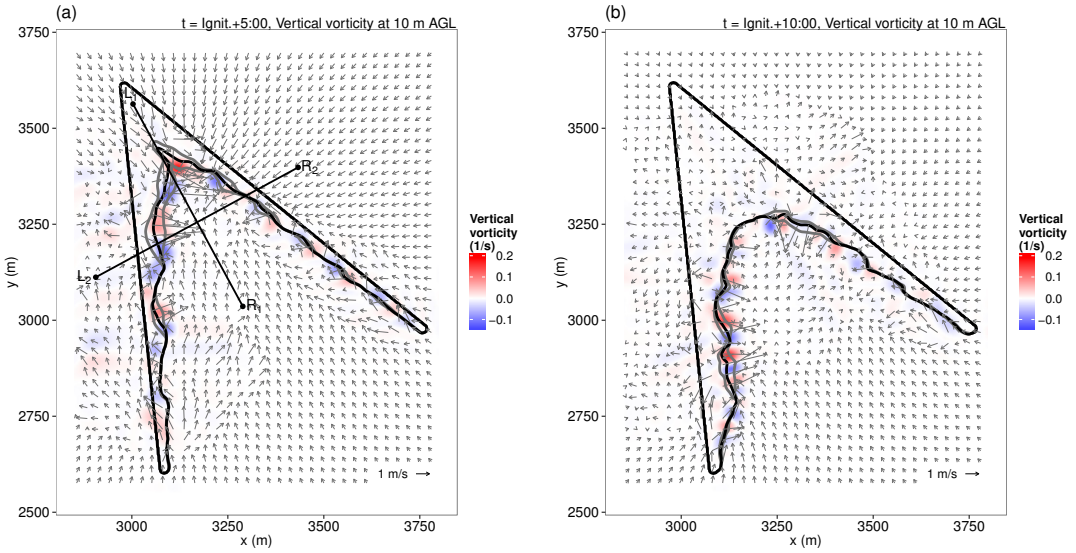

(a) (b)

Figure 4.7: Surface winds at 1 metre AGL (as input into the fire-spread model, but thinned to 28 metre resolution for plotting) and vertical component of vorticity at 10 metre AGL for one 45° ensemble member (a) 5 minutes, and (b) 10 minutes after ignition. The solid black line shows the location of the fireline. To indicate rate of spread, the grey lines (partially obscured) show the fireline 30 seconds earlier and later. The vorticity data have been smoothed to aid visualisation. The transects used in Figure 4.6 are shown in panel (a).

The pattern of vorticity seen in Figure 4.7 is typical of those seen in the other simulation results; regions of the fireline where the fastest spread is occurring are usually associated with pairs of counter-rotating vortices oriented so that they increase the wind speed in the direction of fire spread. Vortices form, merge, and dissipate in a complicated way; they may also migrate along the fireline towards the junction of the merged fronts, possibly advected by the (fire-induced) near-surface winds. This behaviour is illustrated by the vortex pairs in the rectangular region highlighted in Figure 4.8. As they move along the fireline, vortex pairs oriented in the fashion described above produce increased rates of spread in the adjacent region of the front.

To examine how this vertical vorticity is generated, an expression for the change in vertical vorticity of a moving fluid can be obtained by taking the curl of the conservation of momentum equation. In the case of the atmosphere, neglecting

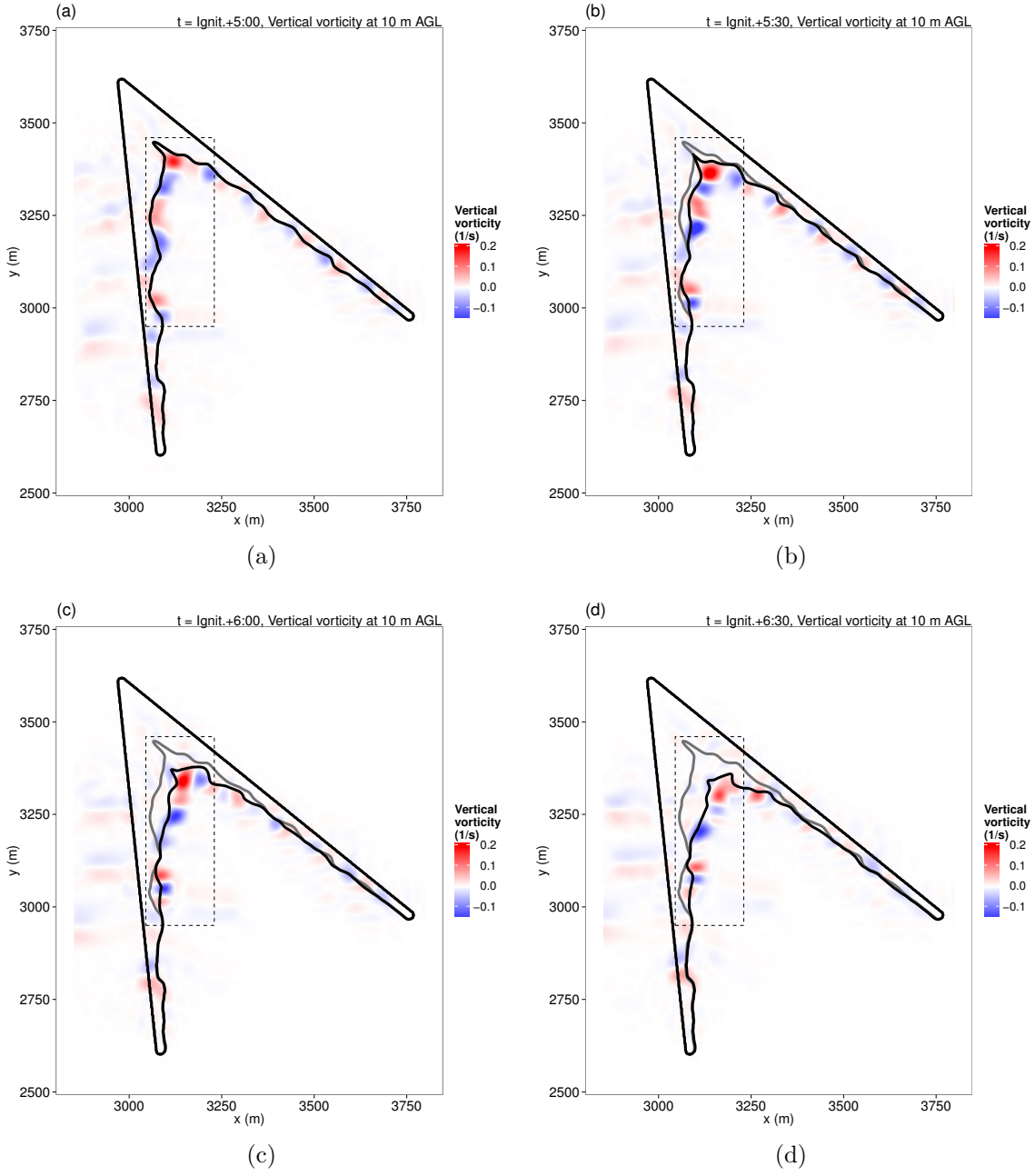

(a) (b) (c) (d)

Figure 4.8: Advection and merging of counter-rotating vortex pairs. The time sequence shows the fire-line location and vertical vorticity for one 45°ensemble member at 30-second intervals, beginning 5 minutes after ignition. The (stationary) grey line shows the location of the fireline at the initial time of the sequence.

viscosity and the Coriolis force, the conservation of momentum equation may be expressed as

$$\frac{\partial \mathbf{w}}{\partial t} + \mathbf{w} \cdot \boldsymbol{\nabla} \mathbf{w} = -\frac{1}{\rho} \boldsymbol{\nabla} p - \boldsymbol{\nabla} \Phi \tag{4.1}$$

where $\mathbf{w}$ is the wind field, p and ρ are pressure and density, and Φ is the geopotential. Using a standard identity from vector calculus, Eqn. (4.1) may be rewritten as

$$\frac{\partial \mathbf{w}}{\partial t} + \boldsymbol{\nabla} \left(\frac{\mathbf{w} \cdot \mathbf{w}}{2} \right) + \boldsymbol{\omega} \times \mathbf{w} = -\frac{1}{\rho} \boldsymbol{\nabla} p - \boldsymbol{\nabla} \Phi. \tag{4.2}$$

Taking the curl of Eqn. (4.2), and recalling that $\boldsymbol{\nabla} \times \boldsymbol{\nabla} = \mathbf{0}$, we obtain

$$\frac{\partial \boldsymbol{\omega}}{\partial t} + \boldsymbol{\nabla} \times (\boldsymbol{\omega} \times \mathbf{w}) = -\boldsymbol{\nabla} \times \frac{\boldsymbol{\nabla} p}{\rho}$$

which may be rewritten as

$$\frac{\partial \boldsymbol{\omega}}{\partial t} = -(\mathbf{w} \cdot \boldsymbol{\nabla}) \boldsymbol{\omega} - (\boldsymbol{\nabla} \cdot \mathbf{w}) \boldsymbol{\omega} + (\boldsymbol{\omega} \cdot \boldsymbol{\nabla}) \mathbf{w} - \boldsymbol{\nabla} \times \frac{\boldsymbol{\nabla} p}{\rho}. \tag{4.3}$$

The vertical component of Eqn. (4.3) is

$$\frac{\partial \omega_3}{\partial t} = -(\mathbf{w} \cdot \boldsymbol{\nabla}) \omega_3 - (\boldsymbol{\nabla} \cdot \mathbf{w}) \omega_3 + (\boldsymbol{\omega} \cdot \boldsymbol{\nabla}) w - \left(\boldsymbol{\nabla} \times \frac{\boldsymbol{\nabla} p}{\rho} \right) \cdot \mathbf{k}. \tag{4.4}$$

Expanding the second and third terms on the right hand side of Eqn. (4.4) gives

$$\begin{aligned}
-(\boldsymbol{\nabla}\cdot\mathbf{w})\omega_3 + (\boldsymbol{\omega}\cdot\boldsymbol{\nabla})w &= -\left(\frac{\partial u}{\partial x}+\frac{\partial v}{\partial y}+\frac{\partial w}{\partial z}\right)\omega_3 + \omega_1\frac{\partial w}{\partial x}+\omega_2\frac{\partial w}{\partial y}+\omega_3\frac{\partial w}{\partial z} \\
&= -\left(\frac{\partial u}{\partial x}+\frac{\partial v}{\partial y}\right)\omega_3 + \omega_1\frac{\partial w}{\partial x}+\omega_2\frac{\partial w}{\partial y} \\
&= -\left(\boldsymbol{\nabla}_\mathrm{h}\cdot\mathbf{w}_\mathrm{h}\right)\omega_3 + \left(\frac{\partial w}{\partial y}-\frac{\partial v}{\partial z}\right)\frac{\partial w}{\partial x}+\left(\frac{\partial u}{\partial z}-\frac{\partial w}{\partial x}\right)\frac{\partial w}{\partial y} \\
&= -\left(\boldsymbol{\nabla}_\mathrm{h}\cdot\mathbf{w}_\mathrm{h}\right)\omega_3 + \frac{\partial u}{\partial z}\frac{\partial w}{\partial y}-\frac{\partial v}{\partial z}\frac{\partial w}{\partial x} \\
&= -\left(\boldsymbol{\nabla}_\mathrm{h}\cdot\mathbf{w}_\mathrm{h}\right)\omega_3 + \left(\frac{\partial \mathbf{w}_\mathrm{h}}{\partial z}\times\boldsymbol{\nabla}_\mathrm{h}w\right)\cdot\mathbf{k} \qquad (4.5)
\end{aligned}$$

where the subscript h indicates a quantity or operation in the horizontal plane. Substituting Eqn. (4.5) into Eqn. (4.4) gives

$$\frac{\partial\zeta}{\partial t} = -(\mathbf{w}\cdot\boldsymbol{\nabla})\zeta - \left(\boldsymbol{\nabla}_\mathrm{h}\cdot\mathbf{w}_\mathrm{h}\right)\zeta + \left(\frac{\partial \mathbf{w}_\mathrm{h}}{\partial z}\times\boldsymbol{\nabla}_\mathrm{h}w\right)\cdot\mathbf{k} - \left(\boldsymbol{\nabla}\times\frac{\boldsymbol{\nabla}p}{\rho}\right)\cdot\mathbf{k} \qquad (4.6)$$

where we have written ζ for the vertical component ω_3 of the vorticity $\boldsymbol{\omega}$; see (Jenkins et al. 2001) for example. The first two terms on the right-hand side of Eqn. (4.6) represent the redistribution of existing ζ due to advection and horizontal divergence respectively. The third is the tilting term, which describes the production of ζ by the reorientation of vorticity toward the vertical; it may be rewritten as

$$\left(\frac{\partial \mathbf{w}_\mathrm{h}}{\partial z}\times\boldsymbol{\nabla}_\mathrm{h}w\right)\cdot\mathbf{k} = \frac{\partial u}{\partial z}\frac{\partial w}{\partial y}-\frac{\partial v}{\partial z}\frac{\partial w}{\partial x}.$$

The fourth term, the solenoidal term, represents the generation of vorticity when the gradients of pressure and density are not aligned. Its effect was analysed numerically

by Clark et al. (1996a) for their simulations, and found to be dominated by the tilting term. In the following analysis we ignore the effect of the solenoidal term.

We examine the formation of one vortex pair from the simulation depicted in Figure 4.1(d), chosen because the vertical vorticity is small in the region at the beginning of the time interval considered, and because the pair remains stationary over this time interval. Figure 4.9(a) shows the fireline 7:30 minutes after ignition, before the pair forms. In Figure 4.9(b) we have plotted the lowest 500 metres of the wind field along the transect L to R, 8:20 minutes after ignition. A region of horizontal vorticity has formed in the bottom 50 metres of the atmosphere, at or just ahead of the base of the plume. It appears that the vorticity is generated by the horizontal gradient in buoyancy. In Figure 4.9(c) we have plotted the tilting term, and Figure 4.9(d) shows the vertical vorticity 8:30 minutes after ignition; a counter-rotating vortex pair has formed, consistent with the tilting shown in Figure 4.9(c). Taken together, the four panels of Figure 4.9 indicate that the counter-rotating vortex pair is associated with the tilting of horizontal vorticity generated by the buoyancy gradient. The orientation of the horizontal vorticity is such that the resultant vortex pair induces a surface wind in the direction of the fire spread.

When just one of the firelines is ignited, i.e. when the fire evolves from an initial straight line, the fire-line evolution and the overall rate of spread is quite different to that exhibited when both firelines are ignited (see Figure 4.4). Figure 4.10(a) shows the fireline and vertical vorticity 12 minutes after ignition, when just one of the firelines of Figure 4.7 is ignited. The pattern of counter-rotating vortex pairs is present, but these features are, for the most part, much less intense, and they usually lie behind the fireline rather than on or ahead of it. Consequently, they do not have the same effect of increasing the modelled rates of spread. Similar comments apply to a junction fire later in its evolution, for example in Figure 4.10(b). In Figure 4.10 the only parts of the firelines with an elevated rate of spread are associated with

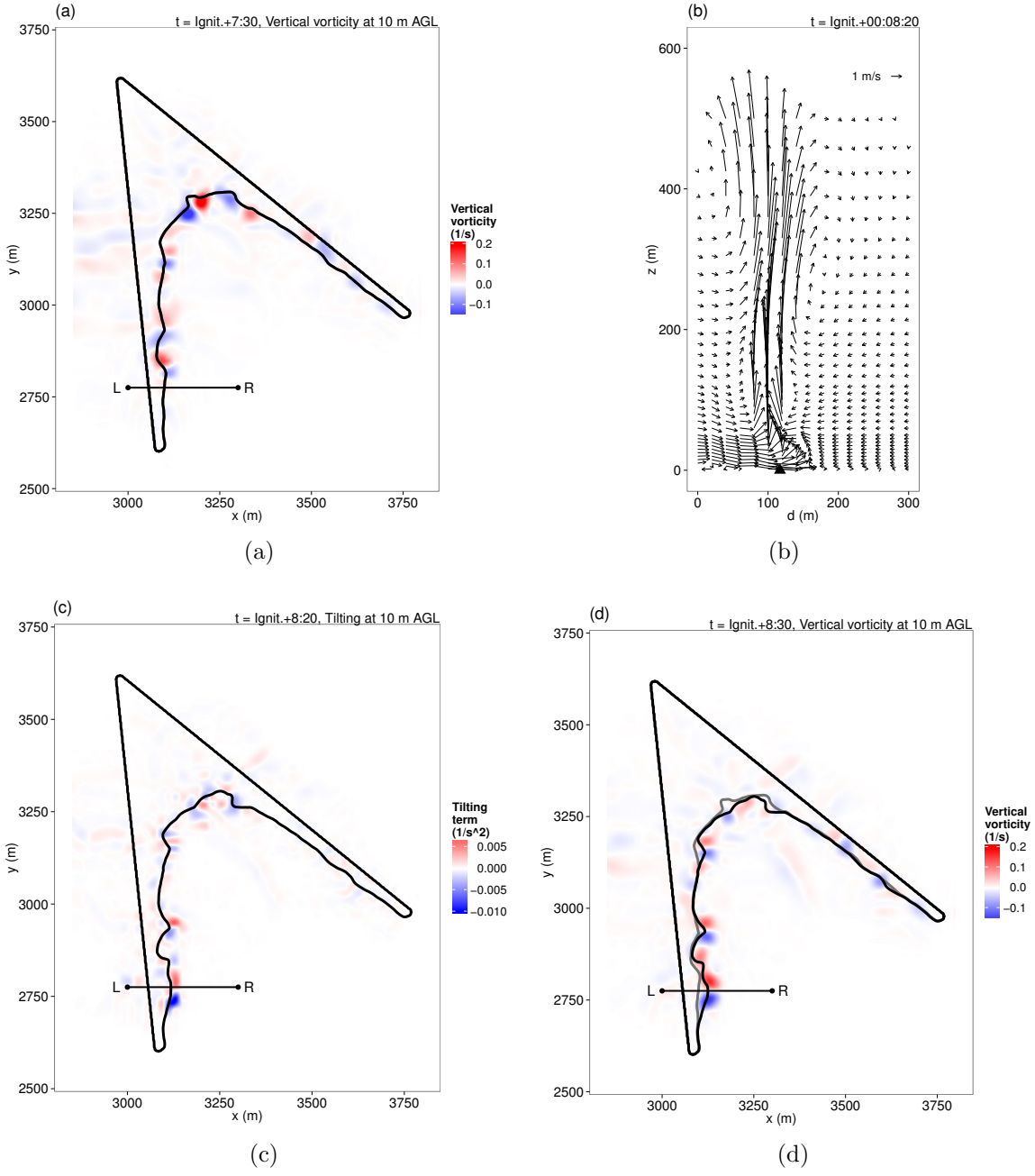

Figure 4.9: Production of vertical vorticity by tilting. (a) fireline and vertical component of vorticity 7:30 minutes after ignition, showing location of transect. (b) Component of wind field along transect (only the bottom 500 metres is shown). (c) Tilting term $\frac{\partial u}{\partial z}\frac{\partial w}{\partial y} - \frac{\partial v}{\partial z}\frac{\partial w}{\partial x}$ from Eqn. (4.6). (d) fireline and vertical component of vorticity 8:30 minutes after ignition (the grey line shows the fireline location 7:30 minutes after ignition).

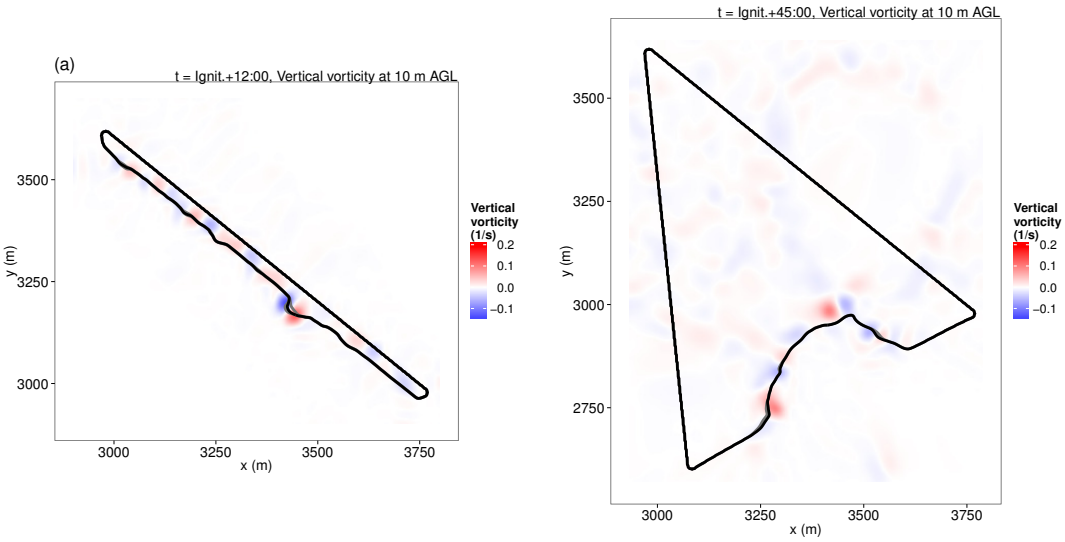

(a) (b)

Figure 4.10: fireline and vertical component of vorticity: (a) 12:00 minutes after ignition of straight fireline, and (b) 45 minutes after ignition of the same ensemble member shown in Figure 4.7. To indicate rate of spread, the grey lines (largely obscured) show the location of the fireline 30 seconds earlier and later.

pairs of more intense vortices that have formed above or ahead of the fireline. Such pairs occur in all the straight-line simulations that we have done; they are short lived, but they are the reason that these simulated fires do not evolve closer to a perfect straight line (see the grey lines in Figure 4.4).

The pattern of vertical vorticity seen in Figure 4.10(a) is typical of all the straight-line simulations performed for this study, just as the patterns in Figures 4.7, 4.8 and 4.10(b) are typical of all the junction fire simulations. The work of Hilton et al. (2018) indicates that it is the geometry of the fireline that influences the bulk surface flow. It is conjectured that it also influences the configuration of these patterns of vertical vorticity, perhaps because of its influence on the wind field, and that both the bulk surface flow and the vertical vorticity contribute to the dynamic fire propagation observed in the simulations.

4.3.5 Relationship to other studies of vorticity and fire-line dynamics

Clark et al. (1996a) used a coupled atmosphere-fire model to study small-scale fire-line dynamics at similar scales, and using the same horizontal atmospheric resolution, as the numerical experiments described here. They described a process they called 'dynamic fingering' in which horizontal vorticity is tilted toward the vertical, increasing the wind speed in the direction of fire spread. This tilting of horizontal vorticity is the process described by Eqn. (4.3.4). Clark et al. (1996a) posited negative vertical wind shear as the mechanism generating the horizontal vorticity, and in their simulations they observed an instance of dynamic fingering which they attributed to a convective downdraught causing wind shear behind the fireline. In our case the generation of horizontal vorticity is driven by buoyancy; the process is illustrated by Figure 4.9.

Clark et al. (1999) performed image flow analysis on infrared imagery of a crown fire. Their results indicated the tilting of horizontal vorticity leading to counter-rotating pairs of vertical vortices oriented so as to increase the rate of spread, a process resembling that observed in the simulations presented here. Clark et al. (2005) used a similar procedure to process infrared imagery of experimental grass fires; they observed horizontal vortices form, tilt, and break apart to produce rotating columns. They simulated one of these experimental fires using a coupled atmosphere-fire model at high resolution (1 metre) and the model produced plumes whose sizes and spacing agreed well with the observations; convective columns a few metres wide with a separation of about 5 - 6 metres. While the processes described by Clark et al. (2005) and Clark et al. (1999) appear similar to those seen in our simulations, their observed and simulated convective structures are too small to be resolved by our simulations.

In wind-driven laboratory fires, Finney et al. (2015) observed counter-rotating vortex pairs oriented in the direction of the flow, which they likened to Taylor-Görtler

vortices seen in flow over concave surfaces and heated plates. Canfield et al. (2014) observed similar structures in high resolution simulations of wind-driven fires using the FIRETEC/HIGRAD coupled model (Linn et al. 2002). These are probably not related to the counter-rotating vortices seen in our simulations, in which horizontal vorticity produced by buoyancy gradients, and oriented perpendicular to the fire-induced flow, is tilted toward the vertical.

4.3.6 Sensitivity of results to model resolution

The main suite of 20 simulations considered in this chapter was performed with a horizontal resolution of 20 metres (atmosphere) and 2 metres (fire). To investigate the sensitivity of the results to model resolution we have performed additional simulations using horizontal atmospheric resolutions of 10 and 50 metres for one ensemble member each of the 30° and 45° configurations. The vertical resolution for the 50-metre simulations is the same as that of the 20-metre simulations. For the 10-metre simulations the number of vertical levels has been doubled, with an approximate doubling of the vertical resolution. The 10:1 refinement ratio between the spacing of the fire and the atmospheric grids was maintained in all simulations. Figure 4.11 compares the advance of the central points of the fronts over the full 45-minute period. In all cases, there is good agreement over the period of the simulations for which there is rapid spread, with some divergence at later times. The scatter is of the same order as that observed due to the random orientations (shown by the grey lines in Figure 4.11). At all three resolutions, plots of the individual firelines (not shown) show good agreement, and in each case the behaviour of the model is consistent with the experimental work of Viegas et al. (2012). This indicates that the broad features of the simulated dynamic behaviour will not be altered significantly by using a horizontal resolution smaller than 20 metres.

Figure 4.12 is the equivalent of Figure 4.7 but with the simulations performed at 10 metre resolution. The pattern of vorticity is similar to that in Figure 6, and

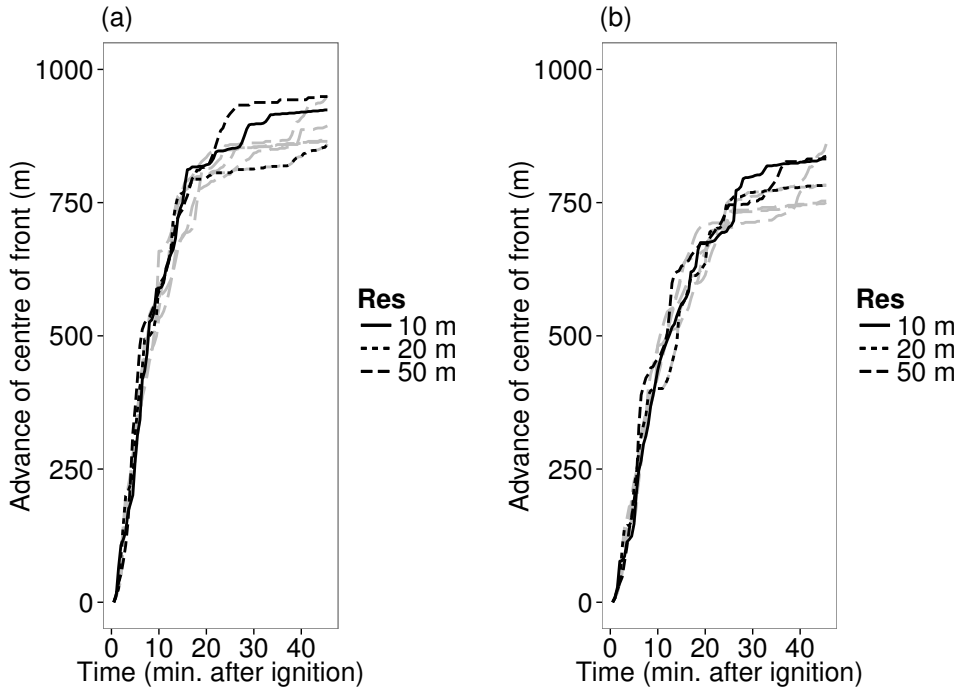

(a) (b)

Figure 4.11: Comparison of advance of centre of simulated front using horizontal atmospheric model resolutions of 10, 20 and 50 metres. One initial orientation of each of the (a) 30° configuration, and (b) 45° configuration was simulated. The grey dashed lines correspond to the other ensemble members (at 20 metre resolution) of the respective configuration.

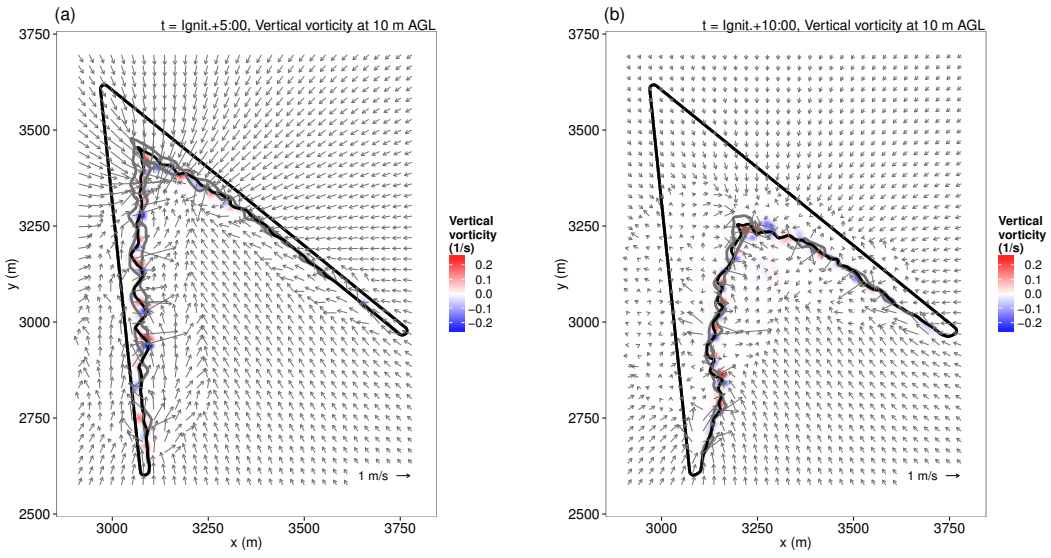

(a) (b)

Figure 4.12: As for Figure 4.7, but simulated using a horizontal atmospheric resolution of 10 metres, and with vertical atmospheric resolution approximately doubled. The fire grid has a resolution of 1 metre.

most regions of rapid spread are associated with a pair of counter-rotating vortices. However, the vortices are smaller and more intense. This indicates that the vorticity is not properly resolved in our simulations. For example, it was noted above that the rotating convective towers observed in infrared imagery by Clark et al. (1999, 2005) were only a few metres in diameter. Clearly, features of this size cannot be resolved with a model running at 20 (or even 10) metre horizontal resolution.

4.3.7 Experiments with ambient wind

A small number of numerical experiments have been performed with an initial ambient wind to determine if the interaction between the two arms of the junction fire increases rate of spread under these conditions. We have confined these experiments to the 45° configuration, and we have used the same random orientations as were used in the case of no ambient wind. Figure 4.13 is like Figure 4.4, but with a 2.5 $\mathrm{m\,s^{-1}}$ background wind in the direction indicated in Figure 4.13(a). As in the case with no ambient wind, when both arms of the junction fire are ignited simultaneously, the front advances more rapidly than the notional front obtained by igniting each arm separately. Figure 4.14 is like Figure 4.2, and shows the centreline advance for all 45° ensemble members with ambient wind speeds of 2.5 and 5 $\mathrm{m\,s^{-1}}$. The reason for the noise and sudden jumps in the plots in Figure 4.14 is the same as that discussed in Section 4.3.3. Another, smoother, indication of the advance of the fronts is given in Figure 4.15, which shows the time evolution of the burnt area. Comparing Figure 4.13 with Figure 4.4 we see that in Figure 4.13 the fire lines are more regular, and the differences between the black and grey lines are less pronounced. The behaviour simulated in Figure 4.4 is driven purely by convection with strong coupling between the fire and the atmosphere promoting the development of vorticity, whereas in Figure 4.13 the coupling between the fire and the atmosphere is reduced by the wind, and the behaviour of the fire is more stable. This is consistent with the simulations and discussion in (Clark et al. 1996a).

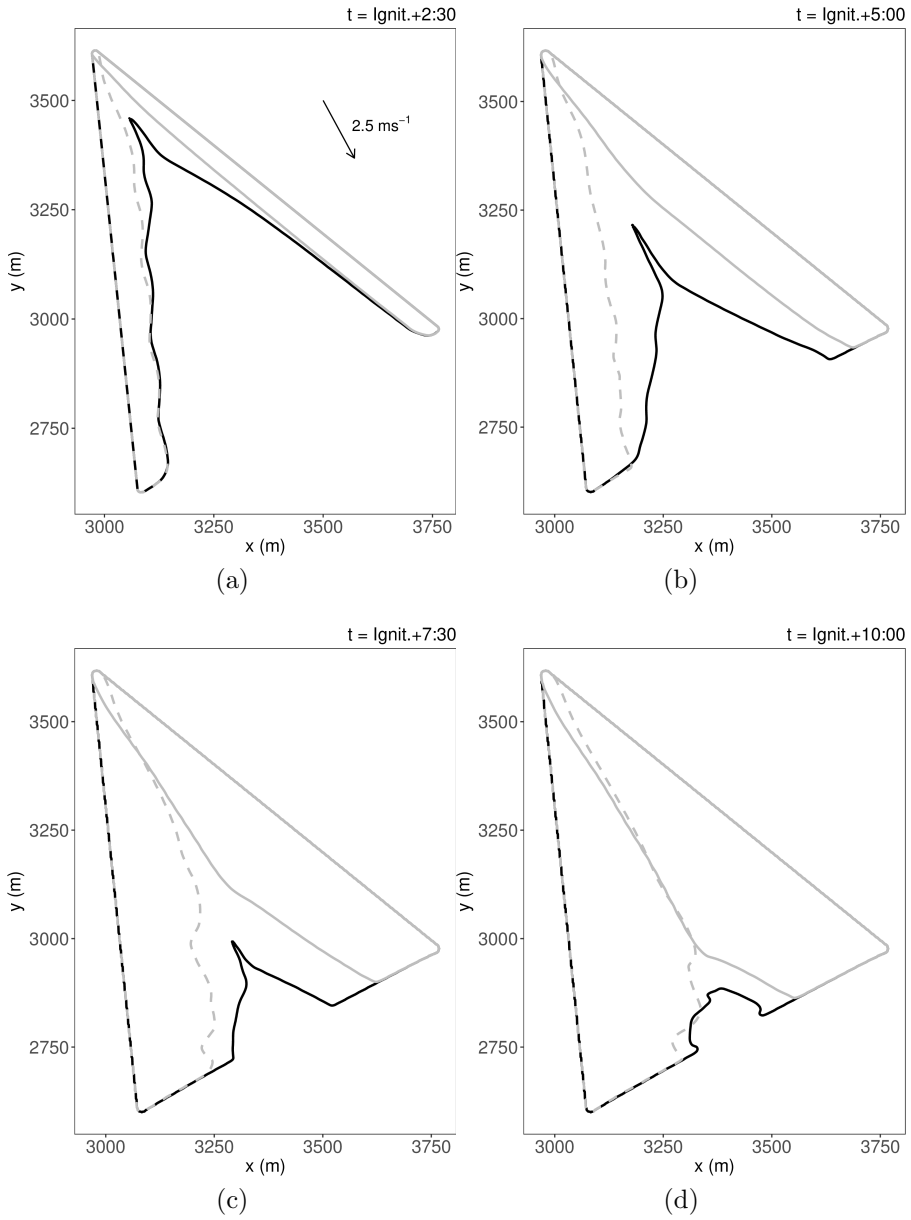

Figure 4.13: As for Figure 4.4, but with a 2.5 m s^{-1} background wind in the direction indicated in panel (a), and at times (a) 2:30, (b) 5:00, (c) 7:30, and (d) 10:00 minutes after ignition. The grey lines show the evolution of the front when only one arm of the V is ignited; together they show how the front would evolve without interaction between the two firelines. The black line shows the evolution when both arms are ignited simultaneously.

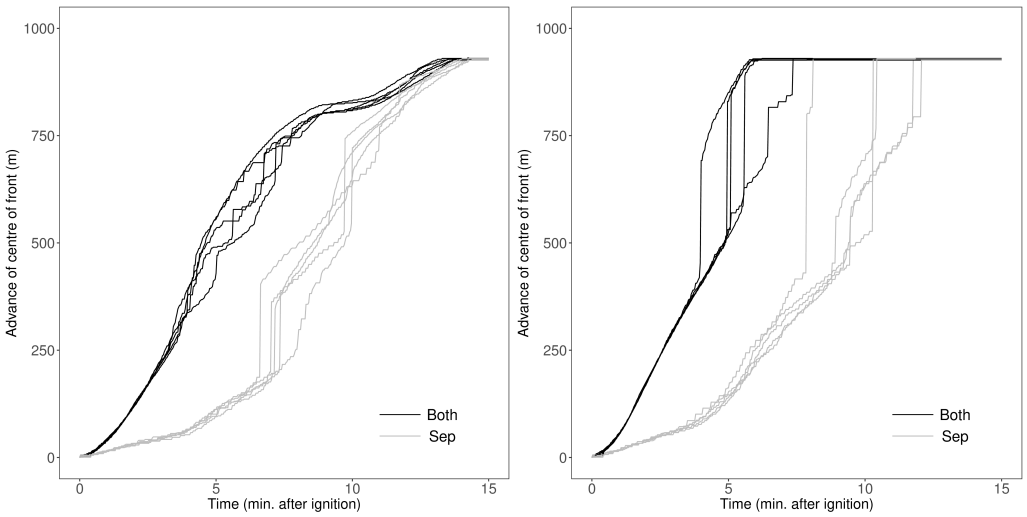

Figure 4.14: Fire front advance over time for junction fire simulations with ambient wind, for all 45° ensemble members, with ambient wind speeds of (a) 2.5 $\mathrm{m\,s^{-1}}$ and (b) 5 $\mathrm{m\,s^{-1}}$. In each case the ambient wind is directed along the axis of the junction fire as indicated, for example, in Figure 4.13(a). Distance advanced is measured along the axis of symmetry of the 'V'. Black lines (labelled 'Both') represent spread when both arms of the V-configuration are ignited simultaneously; grey lines (labelled 'Sep') indicate spread when each arm is ignited separately.

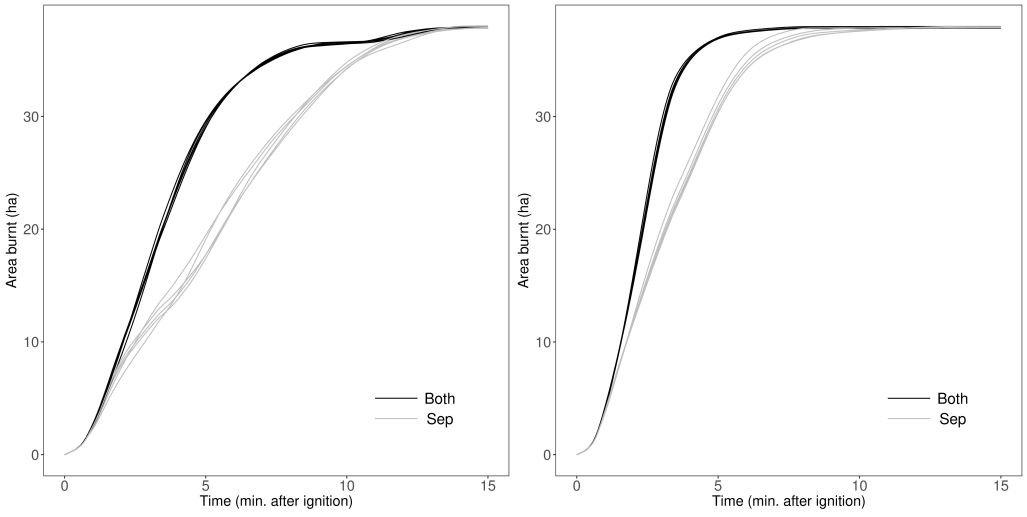

Figure 4.15: Area burnt over time for junction fire simulations of all 45° ensemble members, with ambient wind speeds of (a) 2.5 $\mathrm{m\,s^{-1}}$ and (b) 5 $\mathrm{m\,s^{-1}}$. In each case the ambient wind is directed along the axis of the junction fire as indicated, for example, in Figure 4.13(a). Black lines (labelled 'Both') represent spread when both arms of the V-configuration are ignited simultaneously; grey lines (labelled 'Sep') indicate spread when each arm is ignited separately.

4.4 Summary

The dynamic behaviour of junction fires is of interest to both researchers and operational personnel. It cannot be modelled in a systematic way using uncoupled simulation models based on empirical fire-spread models but coupled atmosphere-fire models can model this behaviour at landscape scales. In this chapter one such system, WRF-Fire, was used to model the experimental observations of Viegas et al. (2012). Junction fires were modelled under conditions of no wind and no slope, albeit at a different scale to that of the experiments. Qualitatively, the output of the model agreed well with the experimental results; a rapid initial acceleration of the front was observed, with a subsequent slowing of the rate of spread. A quantitative comparison was not possible because of the different scales considered; it is possible that there are different dominant mechanisms underlying the similar behaviour at the two scales. In both the experimental work of Viegas et al. (2012) and the WRF-Fire simulations, the observed dynamic fire behaviour arises through the interaction between the two lines of fire; equivalently, it may be thought of as resulting from the geometry of the merged firelines. In the case of the modelled fires, the mechanism for the rapid fire spread is pyro-convective; in addition to the bulk fire-induced surface flow, it includes the formation of counter-rotating pairs of vertical vortices lying on or ahead of the fireline. These vortex pairs also form in the case of a straight fireline but they usually lie behind the fire front and consequently do not influence the modelled rate of spread to the same extent. Simulations at higher horizontal resolution exhibit similar fireline evolution and rates of spread. They also exhibit similar patterns of vorticity; however, the vortices are smaller and more intense, indicating that the vortical structures are not well resolved at 20-metre resolution. Empirical and numerical studies by Clark et al. (2005) note similar features, but these are too small to be properly resolved by our simulations.

A small number of simulations were made with ambient wind speeds of 2.5 and 5 $\mathrm{m\,s^{-1}}$, but still with no slope. As in the zero-wind case, when both arms of the junction fire are ignited simultaneously then the fire progresses significantly faster than the notional fire front obtained by igniting each of the arms individually.

Chapter 5

Rate of spread and fireline geometry

5.1 Introduction

5.1.1 Definition of plane curvature

If $\boldsymbol{\gamma}(s)$ is a sufficiently smooth plane curve parametrised by arc length s, then its unit tangent vector $\hat{\mathbf{t}}(s)$ is given by $\hat{\mathbf{t}}(s) = \boldsymbol{\gamma}'(s)$. Differentiating both sides of the identity $\hat{\mathbf{t}}(s) \cdot \hat{\mathbf{t}}(s) = 1$ gives $2\hat{\mathbf{t}}(s) \cdot \hat{\mathbf{t}}'(s) = 0$. This shows that $\hat{\mathbf{t}}'(s)$ is perpendicular to $\hat{\mathbf{t}}(s)$, so that $\hat{\mathbf{t}}'(s) = \kappa(s)\hat{\mathbf{n}}(s)$ where $\hat{\mathbf{n}}(s)$ is the unit normal to $\boldsymbol{\gamma}(s)$. The *signed curvature* of $\boldsymbol{\gamma}(s)$ is defined to be $\kappa(s)$. If $\kappa(s) \neq 0$ then the *radius of curvature* $R(s)$ is defined to be $R(s) = 1/|\kappa(s)|$. $R(s)$ is in fact the radius of the osculating circle to the curve $\boldsymbol{\gamma}$ at $\boldsymbol{\gamma}(s)$.

If the curve is defined by the level set $\varphi = c$ of a function $\varphi(x, y)$ then at points on the level set the curvature is given by

$$\kappa = \frac{\varphi_{xx}\varphi_y^2 - 2\varphi_x\varphi_y\varphi_{xy} + \varphi_{yy}\varphi_x^2}{\left(\varphi_x^2 + \varphi_y^2\right)^{3/2}} \tag{5.1}$$

(see, for example, Sethian 1999).

5.2 Rate of spread versus curvature: junction fires

5.2.1 Introduction

In Chapter 4 the dynamic behaviour of junction fires was studied using the WRF-Fire coupled model. As noted there, the rapid advancement of the front observed in Section 4.3.1 when both initial firelines are ignited can be interpreted as an effect of the geometry of the front. Viegas et al. (2012) treated the merged front as two approximately straight firelines and analysed this geometric effect in terms of the angle between them. An alternative treatment was given by Sharples et al. (2013), who modelled the rate of spread in the normal direction to the front as a function of the fireline curvature, with regions of large negative curvature assumed to have a greater rate of spread. They were able to reproduce qualitatively the experimental results of Viegas et al. (2012) by assuming a rate of spread of the form $1-\varepsilon\kappa$, where κ is the curvature and ε is a tuning parameter. Since the output of the WRF-Fire model is also in good qualitative agreement with these experiments, it is natural to look there for a relationship between curvature and the simulated rate of spread.

5.2.2 Local rate of spread versus local curvature in WRF-Fire simulations of junction fires

WRF-Fire computes the evolution of the fire front using a level-set method, in which the fireline is specified by the zero level set, $\{(x, y) : \varphi(x, y) = 0\}$, of the level-set function φ (Section 3.3.3). A discrete version of φ is available as part of the WRF-Fire output, with values defined on the computational fire grid (Section 3.3.1). The curvature κ can be estimated from φ using Eqn. (5.1). The rate of spread is also available as an output of WRF-Fire, defined on the fire grid but valid only at the fire front.

Figure 5.1 shows rate of spread versus curvature for points on the fireline of the junction-fire simulations discussed in Chapter 4, at all output times and for all

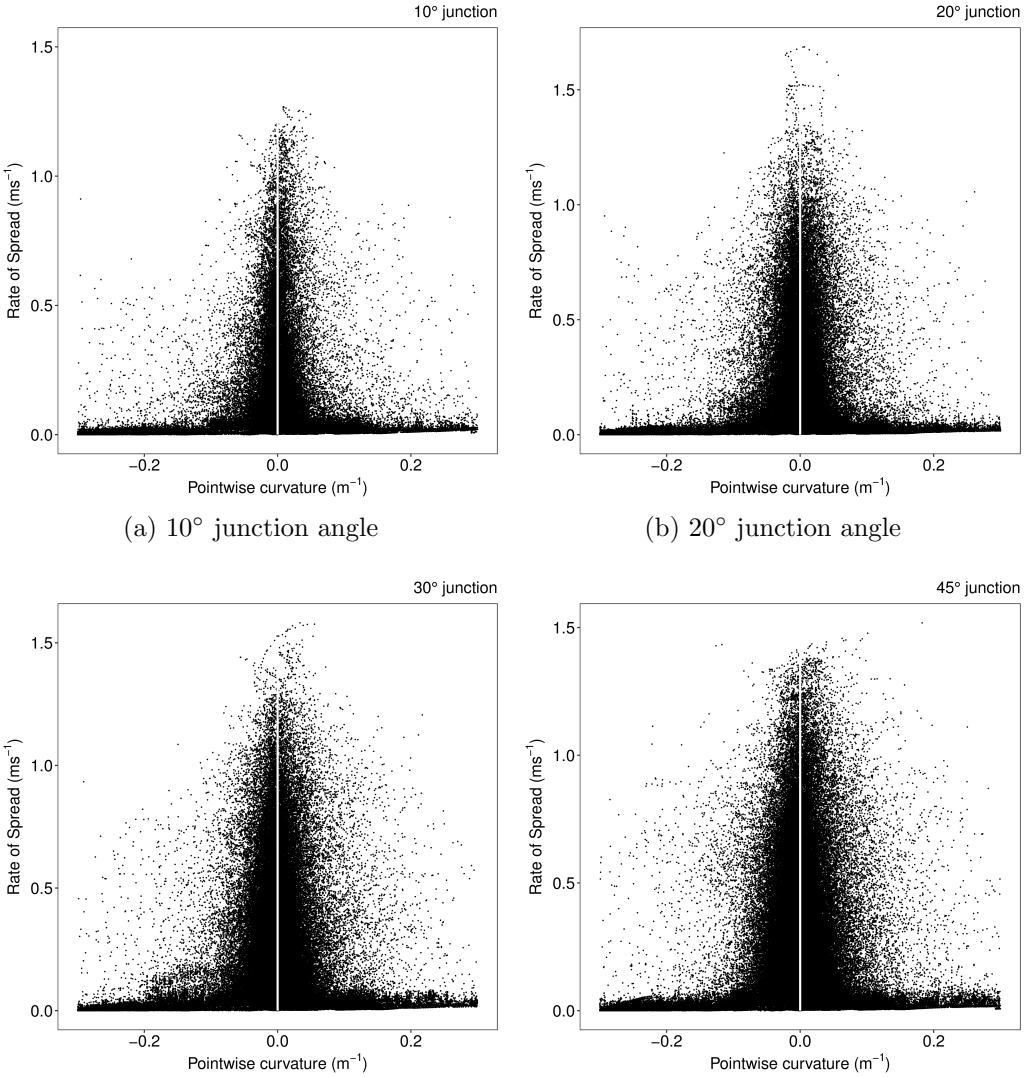

(a) 10° junction angle

(b) 20° junction angle

(c) 30° jvunction angle

(d) 45° junction angle

Figure 5.1: Instantaneous rate of spread versus local fireline curvature for points on the fireline of the junction-fire simulations from Chapter 4. All five of the ensemble members, and all output time steps are represented for each configuration. The curvature κ was computed using a discrete version of Eqn. (5.1). Only points on the front lying within the triangular region formed by the initial firelines are included. To aid visualisation a few outlying points have been removed by restricting κ to $(0.3, 0.3)$.

ensemble members in which both firelines were ignited. These are estimates of instantaneous pointwise rate of spread and local curvature, computed at locations on the front as follows: κ is estimated at grid points by approximating Eqn. (5.1) with finite differences; the location of the front, $\{(x, y) : \varphi(x, y) = 0\}$, is estimated

by interpolating linearly between grid nodes at which φ has opposite sign; κ and rate of spread are then interpolated linearly between their values at these nodes.

Figure 5.1 does not indicate a tendency for higher rates of spread in regions of the fireline with large negative curvature. In some ways this is not surprising; these are instantaneous pointwise rates of spread and local curvatures, yet the pyro-convective processes driving the increased rate of spread in the modelled output are clearly not local, and nor would they be expected to change instantaneously in response to changes in fireline geometry. Furthermore, one expects the values of fireline curvature computed from a discrete version of the level set function to be noisy. Notwithstanding this, it might be expected that a non-local relationship between curvature and rate of spread would be reflected to some extent in Figure 5.1; this does not seem to be the case. In Sections 5.2.3 and 5.3 we examine the data at larger scales, involving notions of average rates of spread and curvature, to attempt to reveal a relationship between these quantities.

5.2.3 Rate of spread versus average curvature in WRF-Fire simulations of junction fires

To compute the curvature from the discrete version of the level set function φ, the partial derivatives in Eqn. (5.1) are approximated at points on the fire grid by finite differences, and are interpolated linearly to a discrete approximation of the fireline, $\{(x, y) : \varphi(x, y) = 0\}$. Both of these approximations contribute to noise and small-scale variability in the computation of the fireline curvature. This is illustrated in Figure 5.2(a). On the other hand, in these simulations the rate of spread is dependent only on the component of the wind field normal to the fireline. The wind field is interpolated to the fire grid from the atmospheric grid, which has a horizontal resolution of 20 metres. Consequently, there is a mismatch in scales: the modelled rate of spread is computed at a larger scale than the local fireline curvature, and does not exhibit variability at such a fine scale (Figure 5.2(b)).

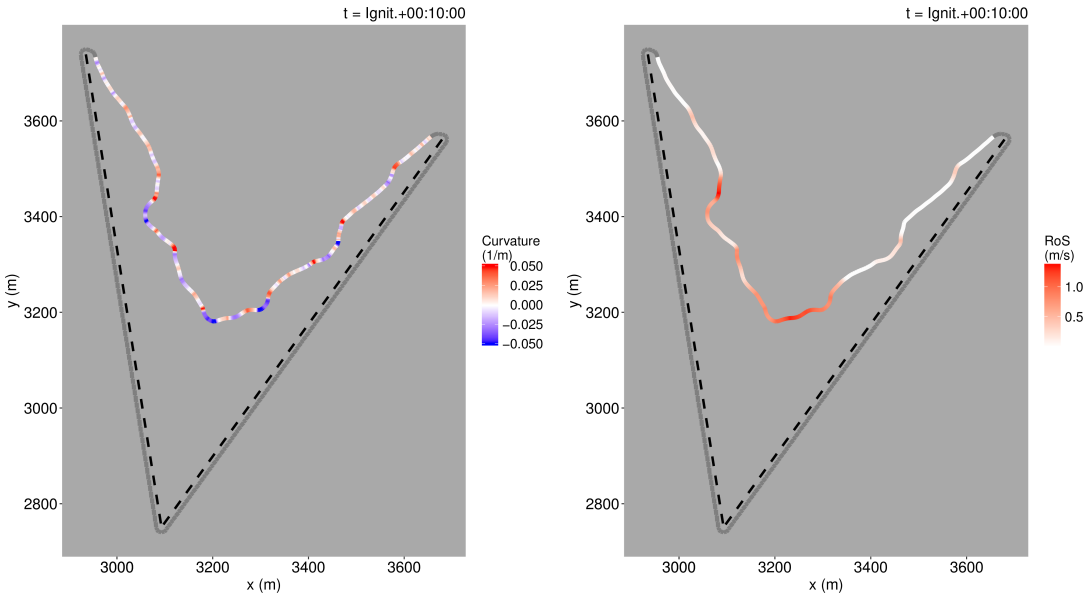

(a) Curvature (b) Rate of spread

Figure 5.2: Fireline showing curvature (a), and rate of spread (b), 10 minutes after ignition for one simulation with a 45° configuration. The curvature is computed using a discrete version of Eqn. (5.1). To aid visualisation, in (a) the full range of curvature, $\approx (-0.09, 0.09)$, is compressed to $(-0.05, 0.05)$. The dashed lines indicate the initial fireline. Curvature and rate of spread are not computed at those parts of the fireline depicted in grey, where fire spread is constrained by a lack of fuel.

To address these concerns, we look for a relationship between rate of spread and curvature at larger spatial scales, and this necessarily involves some form of averaging. The procedure that we have adopted in this case is to form centred, moving averages of the curvature over points of the fireline; at a point P on the fireline, and for a given 'radius' r, we compute the average value of curvature over points on the fireline within arc length r of P. We are working with a discrete version of the fireline which is represented by a series of points, each of which is on a line segment joining two nodes of the fire grid, and it is the value of the curvature at these points over which we take the average. Arc length is computed as the sum of the straight-line distances between pairs in a succession of such points. While the actual number of points involved in the average can vary, it is always at least $2r/(\sqrt{2}d_{\mathrm{f}}) = \sqrt{2}r/d_{\mathrm{f}}$, where d_{f} is the resolution of the fire grid (2 metres in the

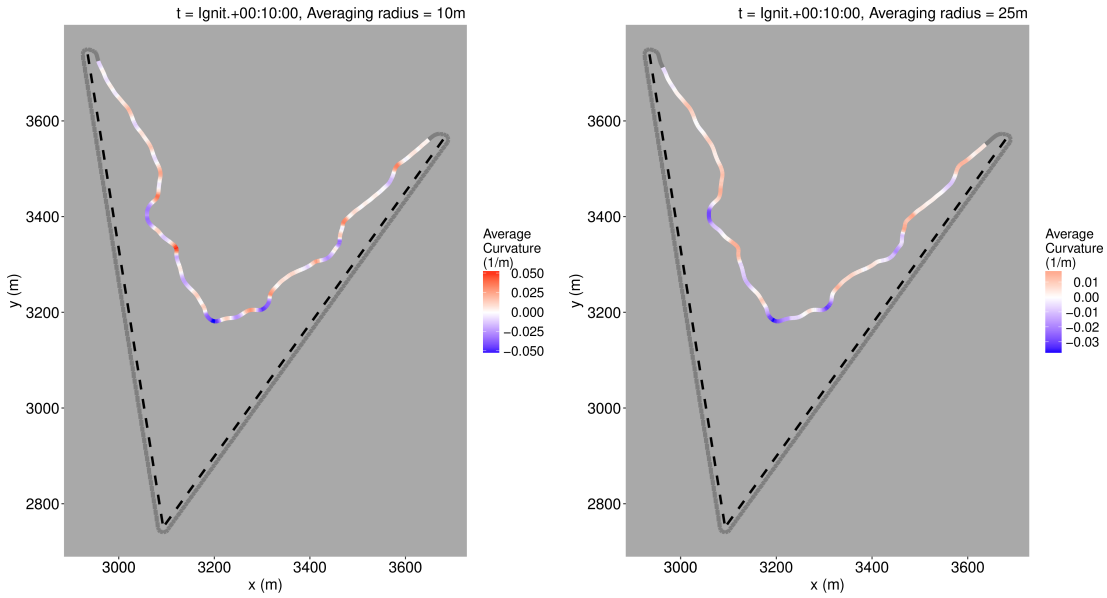

(a) 10 metre averaging radius

(b) 25 metre averaging radius

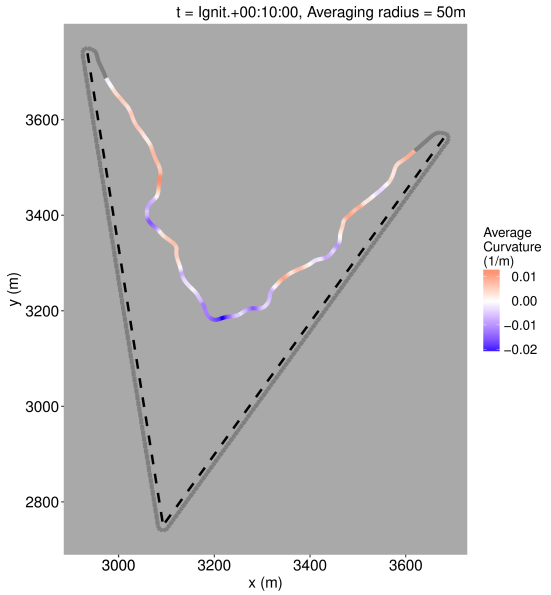

(c) 50 metre averaging radius

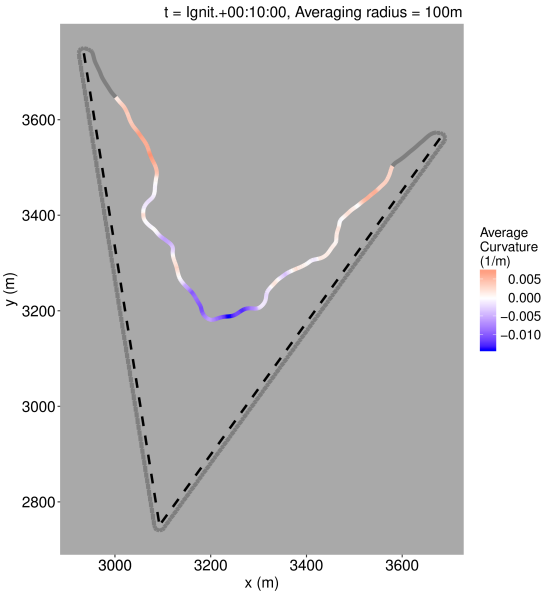

(d) 100 metre averaging radius

Figure 5.3: Fireline curvature averaged over various distances along the fireline for the same simulation depicted in Figure 5.2(a).

present case). This is because neighbouring points representing the fireline cannot be further apart than $\sqrt{2}d_{\mathrm{f}}$. The results of this averaging is illustrated in Figure 5.3, which shows the averaged curvature for various averaging radii for the same fireline that was depicted in Figure 5.2. Figure 5.4 shows rate of spread versus average curvature for all members of the 45° ensemble. While the distributions are skewed

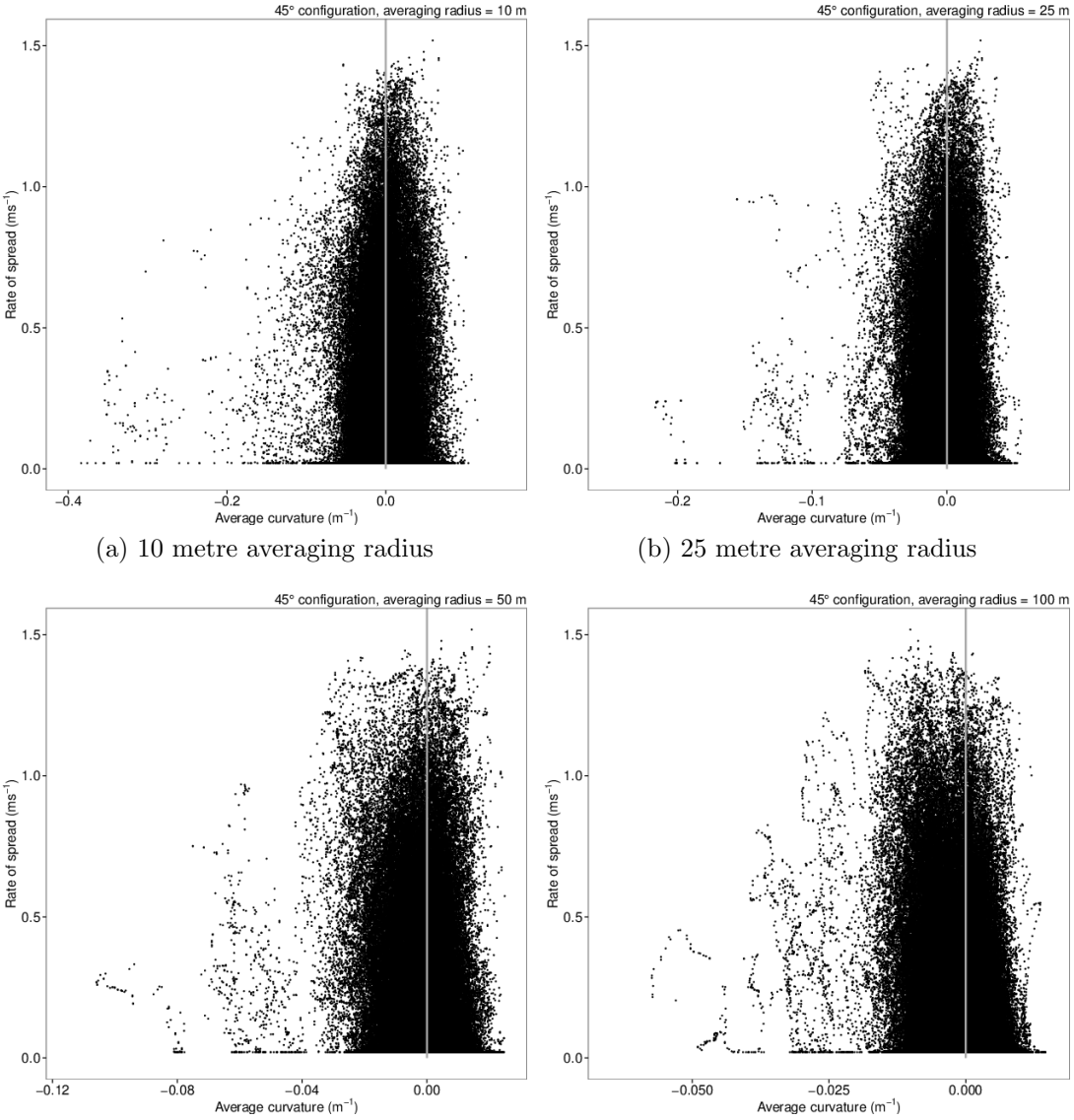

(a) 10 metre averaging radius

(b) 25 metre averaging radius

(c) 50 metre averaging radius

(d) 100 metre averaging radius

Figure 5.4: Rate of spread versus average curvature for points on the fireline of all five of the 45° simulations. All time steps commencing later than 02:00 min after ignition were included. For a given point on the fireline, the average curvature was computed as the average of the curvatures at the (discrete) points on the fireline within arc distance of (a) 10 m, (b) 25 m, (c) 50 m, and (d) 100 m of the given point.

more towards negative values of curvature than those in Figure 5.1, there is no indication that larger negative values of average curvature are associated with higher rates of spread. The results are similar for the other angles (not shown here).

5.3 Rate of spread versus curvature: arc fires

5.3.1 Introduction

In Section 5.2.3, the relationship between fireline curvature and rate of spread was examined at larger spatial scales by forming means of pointwise fireline curvature. Another way of increasing the scale of the analysis is to consider the curvature and rate of spread of some sort of mean fireline. One way of doing this might be to approximate the fireline locally with a higher-order polynomial (in a sense, the analysis in Section 5.2.2 amounts to an approximation with a quadratic). Instead, in this section we examine fires that are initially ignited along a circular arc. At least for a period of time, these fires continue to burn in an approximately circular arc, which simplifies the analysis and allows us to define the curvature of the fireline (as a whole) as the inverse of the radius of the approximating arc. This provides a systematic way of comparing fireline curvature and rate of spread for these simulated fires.

5.3.2 Model set up

In these simulations of arc fires, the computational domain and the initial atmospheric conditions were the same as that used in the numerical experiments described in Section 4.2. Fires were ignited along circular arcs, of radius 500 m and 1000 m, centred within the computational domain, with angular lengths of 60°, 120°, 180°, 240°, 300°, and 360° (a complete circle); in practice, these arcs were made up of a large number of small chords. The fuel used was 'long grass', which is Category 3 of the fuel model system of Albini (1976) and Anderson (1982)). The fuel was constrained to the region within the circle defined by the arc, plus a 30 metre buffer region. Because the results are to some extent sensitive to the initial orientation of the fireline, for each arc angle, a small ensemble of five simulation

were performed with randomly varying orientations (with the exception of a complete circle, where only one simulation was necessary). The atmospheric model was run for an arbitrary interval of 20 minutes, at which time the entire arc was ignited simultaneously, and the model was run for a further one hour.

5.3.3 Results

Figures 5.5 and 5.6 show fireline evolution for selected simulations, and are typical of all members of the respective ensembles.

Each of the initial arcs in Figure 5.5 has the same radius, and hence the same curvature. However the distances between the isochrones show that the rate of spread is quite different in each panel; the rate of spread increases with increased arc length, and does not appear to increase as the fireline evolves into arcs of smaller radii with larger (negative) curvature. The same is true of Figure 5.6.

To enable a more quantitative analysis of the results, this discussion can be made more precise as follows. For every ensemble member, the initial arc defines a pie-shaped region, indicated in Figures 5.5 and 5.6 by the solid arc and dashed radii. For that part of the fireline that lies within this region, we compute the average distance of the fireline from the centre of the arc, and approximate the fireline within this region by a circular arc whose radius is equal to this average distance. It is clear from Figures 5.5 and 5.6 that the validity of this approximation varies somewhat from case to case; it appears to be more valid for arcs with a 1000 metre radius. Nevertheless, it provides a systematic way of defining an average fireline within this region. In Figure 5.7, which summarises the results of this analysis, this average radius (normalised by dividing by the radius of the initial arc) has been plotted against time. Rates of spread do not increase with decreasing radius (i.e. increasing curvature). Furthermore, for initial arcs *with the same curvature*, rates of spread depend on the length of the arc, and are greater for longer arcs.

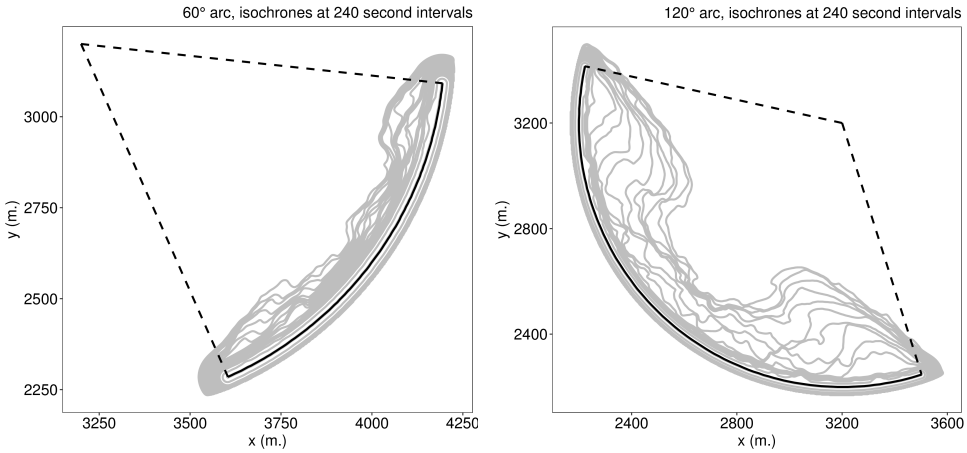

(a) 60° arc

(b) 120° arc

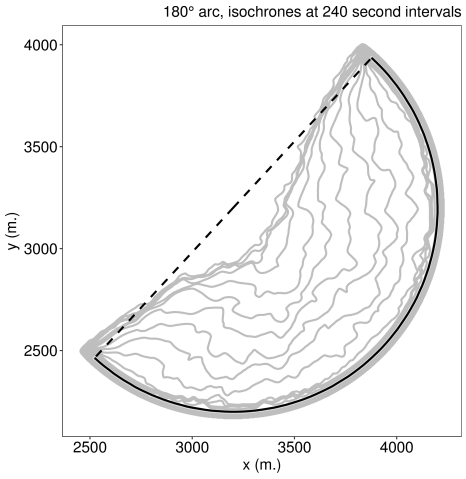

(c) 180° arc

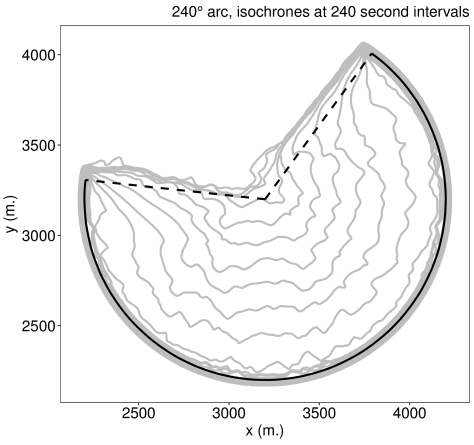

(d) 240° arc

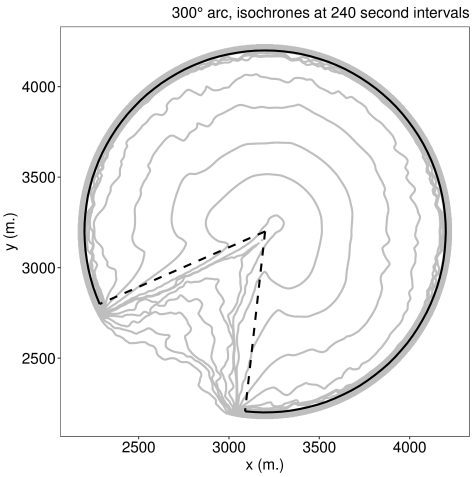

(e) 300° arc

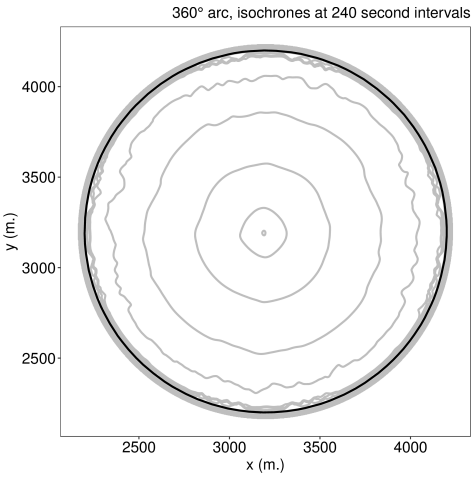

(f) 360° arc

Figure 5.5: Isochrones (grey lines) at 4 minute intervals for fires ignited on arcs of 1000 metre radius, and varying angular lengths. One member each of the (a) 60° (b) 120°, (c) 180°, (d) 240°, and (e) 300°, ensembles is shown. Only one run was done for the 360° arc (panel (f)). The solid black lines represent the arc that was initially ignited.

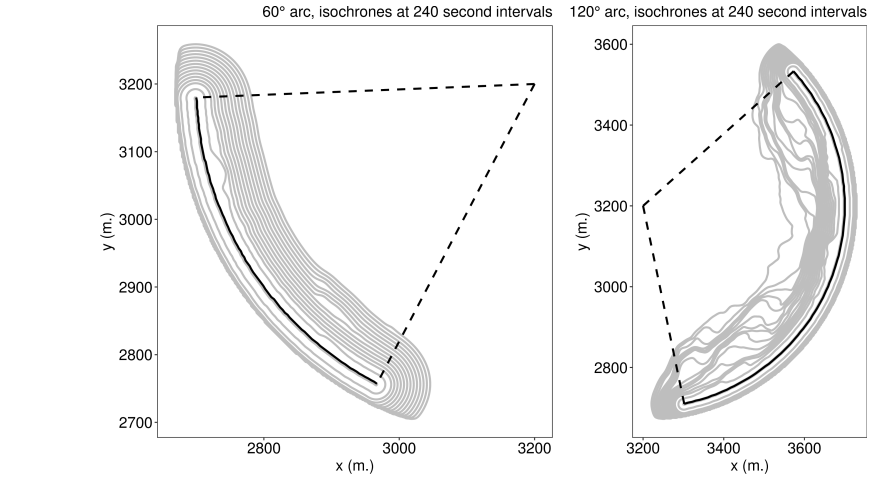

(a) 60° arc

(b) 120° arc

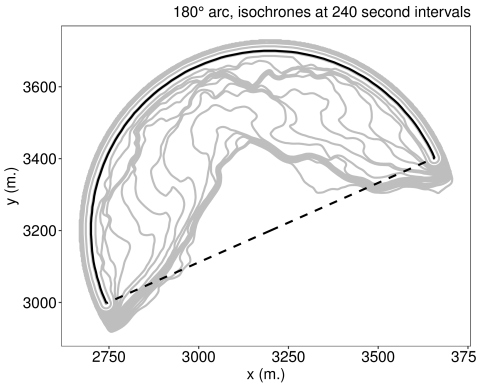

(c) 180° arc

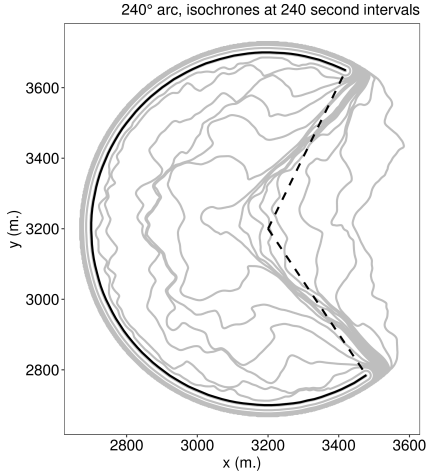

(d) 240° arc

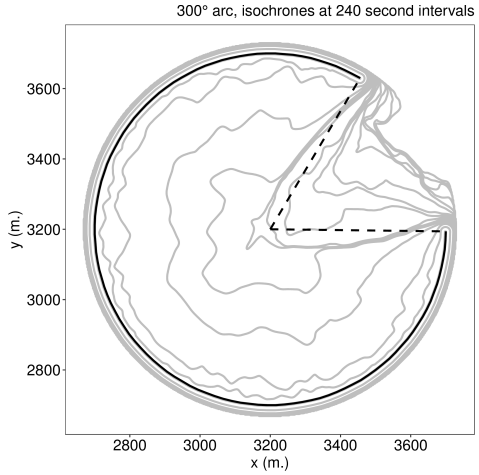

(e) 300° arc

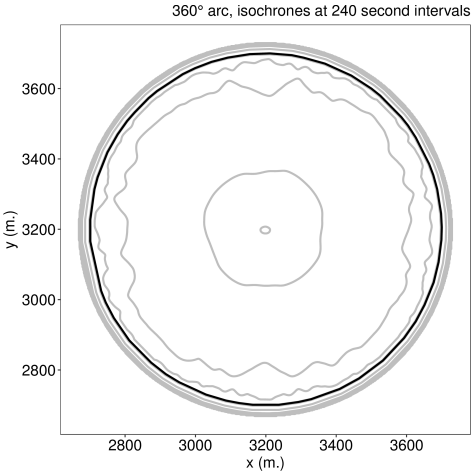

(f) 360° arc

Figure 5.6: As for Figure 5.5, but for arcs with radius 500 metre.

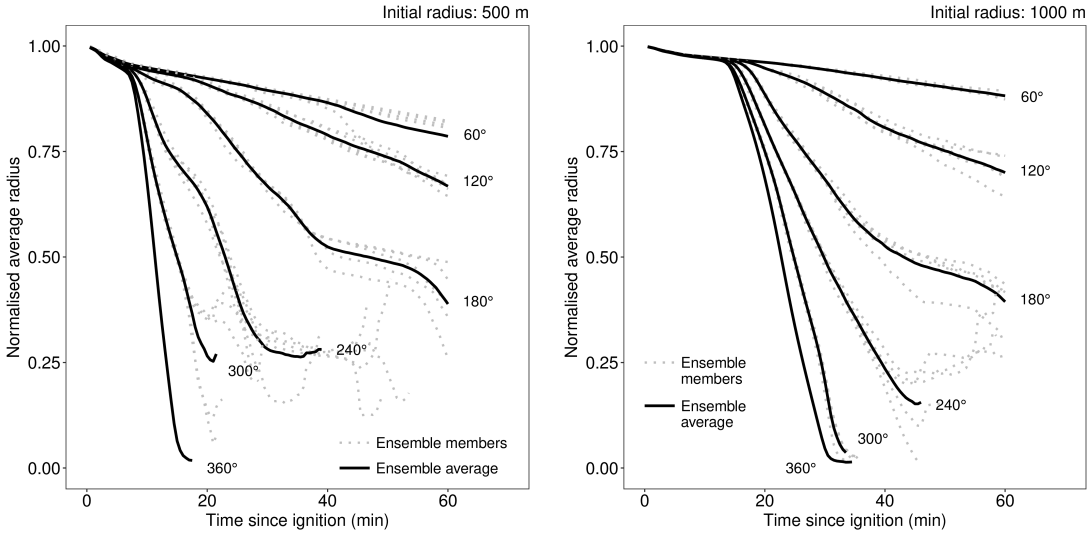

(a) 500 metre arcs (b) 1000 metre arcs

Figure 5.7: Normalised average radius versus time for arc-fire simulations with initial radius (a) 500 metre, and (b) 1000 metre. The dotted grey lines show the results for the individual ensemble members, the solid black lines show the ensemble averages. The average radius is computed as explained in the main body of the text, and is normalised by dividing by the initial radius (500 or 1000 metre).

5.4 Modelling arc fires with the pyrogenic-potential model

In this section we present simulations of arc fires using the pyrogenic-potential model (Section 3.5 and (Hilton et al. 2018)) implemented in the Spark modelling framework (Miller et al. 2015). The work presented in this section (Section 5.4) is joint work with Dr James Hilton of CSIRO, and the simulations presented here, using the pyrogenic-potential model, were carried out by him (James Hilton, personal communication).

5.4.1 Model setup

To enable comparison with the results of Section 5.3, the simple fire-spread model expressed in Eqn. (3.4) was replaced with one derived from the Rothermel model (Rothermel 1972), as implemented in WRF-Fire, using parameters for Category 3

(long grass) of the fuel classification system of Albini (1976) and Anderson (1982):

$$S = u_0 + u_1 \min(\max(\mathbf{w} \cdot \hat{\mathbf{n}}, 0), 30)^{\beta} \tag{5.2}$$

with $u_0 = 0.02048$, $u_1 = 0.18506$, and $\beta = 1.31076$. Here $\mathbf{w}$ is the wind generated by the pyrogenic model (no ambient wind was imposed), and S is the rate of spread in the normal direction $\hat{\mathbf{n}}$ of the fireline; all units are in $\mathrm{m\,s^{-1}}$.

The intensity I was modelled using (Eqn. (3.5)) with parameters obtained from the WRF-Fire code. Thus the fire intensity associated with a pixel at time t is

$$I(t) = \begin{cases} 0 & \text{if } t < t_{\mathrm{i}}, \\ \dfrac{HM_0}{\tau} e^{-(t-t_{\mathrm{i}})/\tau} & \text{if } t \geq t_{\mathrm{i}}, \end{cases} \tag{5.3}$$

where $M_0 = 0.675\ \mathrm{kg\,m^{-2}}$, $\tau = 8.235$ seconds, $H = 16.1 \times 10^6\ \mathrm{J\,kg^{-1}}$, and t_{i} is the time at which the pixel ignites. Eqn. (5.3) is consistent with the treatment of heat fluxes in WRF-Fire (Section 3.3.4).

To summarise the model:

$$\left.\begin{aligned} \frac{\partial \varphi}{\partial t} + (u_0 + u_1 \min(\max(\mathbf{w} \cdot \hat{\mathbf{n}}, 0), 30)^{\beta}) |\boldsymbol{\nabla} \varphi| = 0 \\ \mathbf{w} = \boldsymbol{\nabla} \psi \\ \boldsymbol{\nabla}^2 \psi = kI \end{aligned}\right\} \tag{5.4}$$

where φ is the level-set function and ψ is the pyrogenic potential. All other terms and parameters in Eqns. (5.4) have been defined above with the exception of k, which determines the strength of the forcing kI in the Poisson equation, and has units $\mathrm{J^{-1}}$. In this model, k is regarded as a free parameter, and was chosen to be

$k = 4 \times 10^{-6}$ J^{-1} in the simulations presented here. This value was chosen manually to provide a reasonable match with the results shown in Figure 5.5.

The simulations were carried out on a domain of 2555×2555 metres with a resolution of 5 metres. The fire was initialised along various arcs of radius 1000 metres with the same included angles used in Section 5.3, and were assumed to be initially burning with a speed S of 1 m s^{-1}.

5.4.2 Results and discussion

Figure 5.8 shows isochrones at four-minute intervals of the firelines simulated using the pyrogenic-potential model configured as described in Section 5.4.1. With the exception of the 360° arc, there is remarkably good agreement between the WRF-Fire simulations (Figure 5.5) and those produced using the pyrogenic-potential model. The pyrogenic-potential model is able to reproduce the essential behaviour of the WRF-Fire model when simulating arc fires. In particular, rates of spread increase with increased initial arc length, and do not increase with increasing curvature as the fireline evolves. These are features that a model based on a curvature-dependent rate of spread could not reproduce. Such a model would produce rates of spread that are independent of initial arc length, and that increase as the fireline evolves and curvature increases (becomes more negative).

Clearly, the geometry of the fireline affects the rate of spread predicted by the pyrogenic-potential model, via its influence on the spatial distribution of the intensity I, and therefore the source term kI, in the Poisson equation. However, this relationship between fireline geometry and rate of spread is not easily defined, and cannot be described simply in terms of fireline curvature.

In these simulations the source term ν in the Poisson equation was prescribed as $\nu = kI$, and the value of k was selected by hand. An appropriate choice of the form

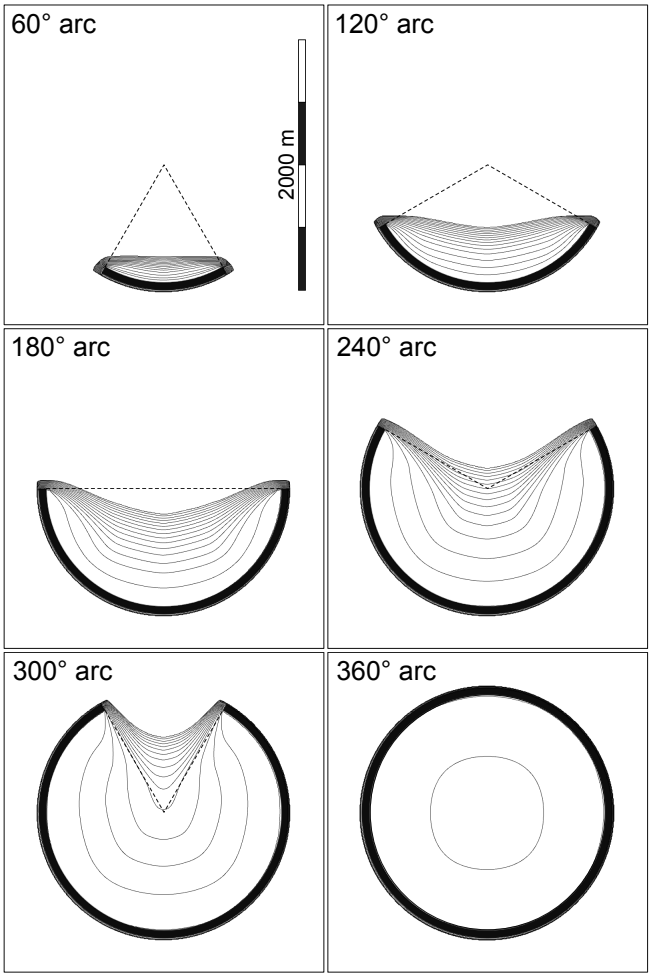

Figure 5.8: Isochrones at four-minute intervals of simulated firelines for fires ignited along arcs of indicated angular length, simulated using the pyrogenic-potential model configured as described in Section 5.4.1. The radius of the initial arcs is 1000 metres.

of $\nu = f(I)$ is critical to the future utility of the pyrogenic-potential model, and is the subject of current research.

5.5 Comparison of WRF and pyrogenic-potential models: static circular heat source

In Section 5.4 the pyrogenic-potential model was configured so that both the fire-spread model and the resulting release of heat are essentially identical to that implemented in WRF-Fire. Any differences between the models reside primarily in the way the modelled surface wind field responds to the release of heat. Therefore

it is instructive to look at a simple test case by examining the wind fields produced by WRF and the pyrogenic-potential model in response to a static heat source. The simplest conceivable static heat source is a constant heat source with the shape of a circular disc, and in this case it is possible to solve the Poisson equation analytically. In this section we do this, and make a comparison of the wind field produced by it with that produced by WRF simulations.

5.5.1 Analytical solution of Poisson equation

We assume that the heat source extends over a disc $B(\mathbf{0}, a)$ of radius $a > 0$ centred at the origin, and that it produces a constant forcing of ν in the Poisson equation. Thus we want to find the solution on $\mathbb{R}^2$ of

$$\boldsymbol{\nabla}^2 \psi = \nu \chi_{B(\mathbf{0},a)} \tag{5.5}$$

where $\chi_{B(\mathbf{0},a)}$ is the characteristic function of $B(\mathbf{0}, a)$. More particularly, we are interested in $\mathbf{w} = \boldsymbol{\nabla}\psi$.

We work in radial coordinates (r, θ) but, by radial symmetry, the potential $\psi = \psi(r)$ is a function of r only. In this case, the gradient operator $\boldsymbol{\nabla}$ and the Laplacian $\boldsymbol{\nabla}^2$ may be expressed as

$$\begin{aligned} \boldsymbol{\nabla}\psi &= \partial_r \psi \, \hat{\mathbf{r}}, \text{ and} \\ \boldsymbol{\nabla}^2 \psi &= \partial_{rr}\psi + \frac{1}{r}\partial_r \psi \\ &= \frac{1}{r}\partial_r (r \partial_r \psi), \end{aligned}$$

where $\hat{\mathbf{r}}$ is the unit vector in the (outward) radial direction. If $\boldsymbol{\nabla}^2\psi = \lambda$ for $\lambda \in \mathbb{R}$, then

$$\begin{aligned}
\boldsymbol{\nabla}^2\psi = \frac{1}{r}\partial_r(r\partial_r\psi) = \lambda \;&\Rightarrow\; \partial_r(r\partial_r\psi) = \lambda r \\
&\Rightarrow\; r\partial_r\psi = \frac{\lambda r^2}{2} + c \\
&\Rightarrow\; \partial_r\psi = \frac{\lambda r}{2} + \frac{c}{r} \\
&\Rightarrow\; \boldsymbol{\nabla}\psi = \left(\frac{\lambda r}{2} + \frac{c}{r}\right)\hat{\mathbf{r}}.
\end{aligned}$$

If ψ solves Eqn. (5.5) then, setting $\lambda = \nu$ in $B(\mathbf{0}, a)$, and $\lambda = 0$ elsewhere, we obtain

$$\boldsymbol{\nabla}\psi = \begin{cases} \left(\dfrac{\nu r}{2} + \dfrac{c_1}{r}\right)\hat{\mathbf{r}} & \text{if } r < a, \\ \dfrac{c_2}{r}\,\hat{\mathbf{r}} & \text{if } r \geq a. \end{cases} \tag{5.6}$$

We need to determine the constants c_1 and c_2. By the divergence theorem (e.g. Marsden and Tromba (2003)), for $R > a$,

$$\begin{aligned}
\nu\pi a^2 = \iint_{B(\mathbf{0},R)} \nu\chi_{B(\mathbf{0},a)}\mathrm{d}\mathbf{x} = \iint_{B(\mathbf{0},R)} \boldsymbol{\nabla}^2\psi\,\mathrm{d}\mathbf{x} &= \oint_{\partial B(\mathbf{0},R)} \hat{\mathbf{n}}\cdot\boldsymbol{\nabla}\psi\,\mathrm{d}s \\
&= \oint_{\partial B(\mathbf{0},R)} \hat{\mathbf{r}}\cdot(\partial_r\psi\,\hat{\mathbf{r}})\mathrm{d}s \\
&= 2\pi R\partial_r\psi(R) \\
&= 2\pi c_2 \text{ (by Eqn. (5.6))} \\
\Rightarrow\; c_2 &= \frac{\nu a^2}{2}
\end{aligned}$$

where we have used the fact that $\hat{\mathbf{n}} = \hat{\mathbf{r}}$ on $\partial B(\mathbf{0}, R)$. Using this value of c_2 in Eqn. (5.6), and requiring that $\boldsymbol{\nabla}\psi$ be continuous at $r = a$, implies that $c_1 = 0$, so

that

$$\boldsymbol{\nabla}\psi = \begin{cases} \dfrac{\nu r}{2}\,\hat{\mathbf{r}} & \text{if } r < a, \\ \dfrac{\nu a^2}{2r}\,\hat{\mathbf{r}} & \text{if } r \geq a. \end{cases} \tag{5.7}$$

5.5.2 Surface wind field produced by WRF: static circular heat source

The modified WRF code described in Section 3.4.2 was used to model the wind field produced by a static circular heat source. The model domain was $3200 \times 3200 \times 3000$ metres (length $\times$ width $\times$ height), with a horizontal resolution of 10 metres, and 61 vertical levels with an initial vertical spatial resolution of $\approx$ 4 metres near the surface. All WRF physics options were turned off and the model was run without turbulent diffusion. The model was initialised with no moisture and with a vertical temperature profile consisting of a 1000-metre-deep dry-adiabatic layer at a constant potential temperature of 300 K, topped by a stable layer with potential temperature increasing at 4.5 K per kilometre to the model top. A circular static sensible-heat flux with radius 100 metres and intensity $I = 5 \times 10^4$ W m^{-2} was introduced at the centre of the computational domain and the model was run for one hour to collect wind-field data.

5.5.3 Comparison of WRF and pyrogenic-potential solutions

Figure 5.9 shows the radial profiles of wind speed for the WRF solution at 2 metres AGL, and two analytical solutions with different values of ν. The WRF profile has the same general form as the analytic solutions, although it peaks at a radial distance very close to $r = a/2$, whereas the analytical solutions peak at $r = a$.

Figure 5.9 illustrates the critical role played by the parameter k in Eqns. (2.4) and (5.4) (in the current notation, $\nu = kI$), although clearly there is no choice of ν that would make the analytical solution match the WRF solution well over the entire profile. This is perhaps not too surprising, given the simplifying assumptions made in deriving the model (Section 3.5). For example, the three-dimensional flow

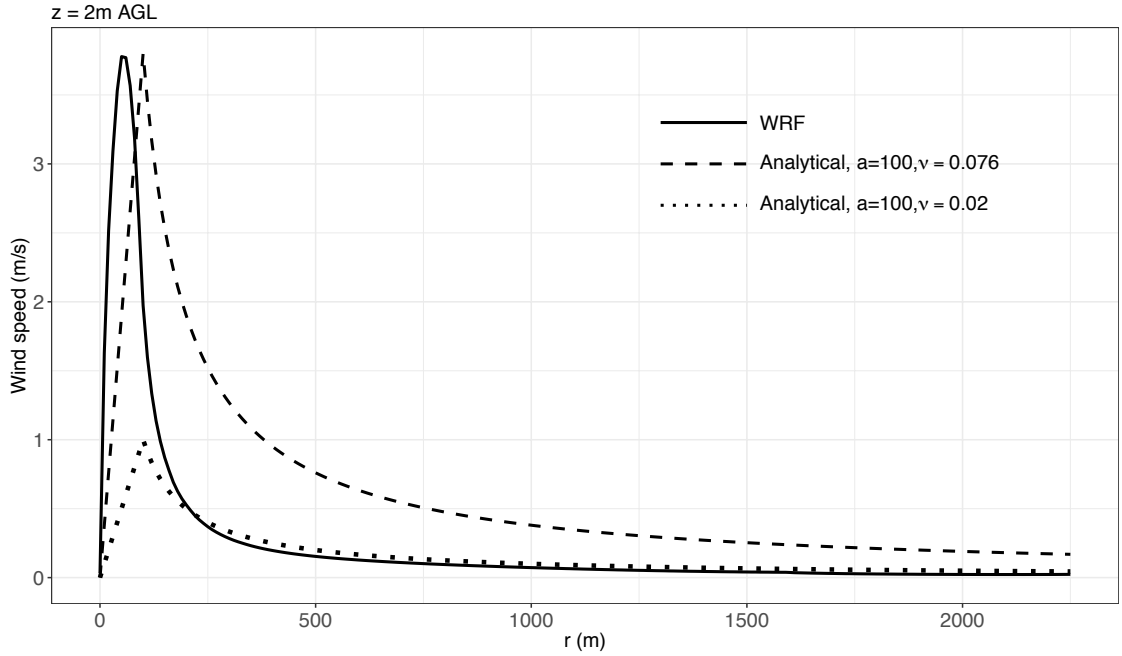

Figure 5.9: Comparison of radial profiles of near-surface wind speed resulting from static circular heat source of $a = 100$ metres radius (r is measured from the centre of the heat source). The solid line is the WRF solution at 2 metres AGL with $I = 5 \times 10^4$ W m^{-2}. The broken lines are analytical solutions (Eqn. (5.7)). The values of ν are arbitrary: $\nu = 0.076$ makes the peak of the analytical solution approximately equal to that of WRF, while $\nu = 0.02$ makes the analytical solution approximately match the WRF solution for $r > 200$ metres.

is assumed to be incompressible, so that $\boldsymbol{\nabla} \cdot \mathbf{w} = 0$, whereas the plume is driven by buoyancy, which derives from changes in density. Even in a steady flow, the continuity equation

$$\frac{\partial \rho}{\partial t} + \boldsymbol{\nabla} \cdot (\rho \mathbf{w}) = 0$$

reduces only to

$$\rho \boldsymbol{\nabla} \cdot \mathbf{w} + \mathbf{w} \cdot \boldsymbol{\nabla} \rho = 0.$$

Nevertheless, the model does a good job of reproducing the behaviour of arc fires simulated with a full coupled atmosphere-fire model, and further development is clearly warranted.

5.6 Conclusion

The results of Sections 5.2 and 5.3 do not indicate a relationship between fireline curvature and rate of spread in the output of the WRF-Fire coupled model at any scale. WRF-Fire does not explicitly represent radiation in its fire-spread model, but convective processes are represented, and in their analysis Raposo et al. (2018) found that it is convective processes that are responsible for the dynamic behaviour observed in junction fires. This conclusion is supported by the work presented in Chapter 4, with more detailed vortex dynamics also playing a role. It seems reasonable to conclude that fireline curvature cannot function as a proxy for these convective processes.

In Section 5.4 it was seen that for simple test cases involving fires ignited along circular arcs the pyrogenic-potential model produces results remarkably similar to those of the WRF-Fire coupled atmosphere-fire model. In these experiments both models used the same fire-spread submodel (with no explicit allowance for the effects of radiation). This indicates that, at least in the case of ring fires in still conditions, the convective effects on fire spread may be represented to first order by a model of the near-surface wind field induced by the pressure deficit resulting from the buoyant plume. The discussion in Section 5.5 shows the limitations of this representation and also highlights the critical role played by the relationship $\nu = f(I)$ between the forcing term ν and the fire intensity I. More work is required to find a suitable form for this relationship.

Chapter 6

The terminal-velocity assumption in simulations of ember transport

Our study of the modelling of junction fires in Chapter 4 was motivated in part by the role that the merging of multiple fires, and consequent dynamic fire behaviour, can play in the development of deep flaming, and large plume-driven fires. This may occur as two firelines merge, as in the Canberra fires of 2003 (Doogan 2006; Viegas et al. 2012), or during the coalescence of multiple spot fires (Cheney and Bary 1969; Wade and Ward 1973). The role of spot-fire coalescence in the development of large plume-driven fires leads naturally to questions about ember transport, and how it should be modelled.

6.1 Introduction

Much of the early work into ember transport discussed in 2.3 used the terminal-velocity assumption (Eqn. (2.13)). This greatly simplifies computations, and allows analytical solutions to various problems under suitable simplifying assumptions. More recently it has become possible to model numerically the atmospheric conditions associated with fires, and these models can resolve the larger turbulent processes involved. The wind fields generated in such models can change at time scales shorter than the time it takes for the solution of Eqn. (2.10) to relax to Eqn. (2.13),

and this calls into question the validity of the terminal-velocity assumption when modelling ember transport in this context. Thurston et al. (2017) made what may be the first numerical study of long-range ember transport, using a large eddy model (LEM) to simulate a turbulent plume, and modelling the transport of embers within that plume over distances of up to 20 kilometres. They used a strong form of the terminal-velocity assumption, using Eqn. (2.13) with a constant terminal fall speed u_∞ to model ember transport. Previously, Koo et al. (2012) found that, in numerical modelling of ember transport from grass fires, the use of the terminal-velocity assumption significantly underestimated the distance that embers were transported compared with modelling which accounted for the momentum of the embers (as does Eqn. (2.10)). These simulations were done at small-medium scales (the computational domain was $640 \times 320 \times 615$ metres). Koo et al. (2012) attributed their results to the fact that, due to their momentum, embers 'can fly faster than their immediate-surrounding winds'. While this is true, for the same reason they can also fly more slowly, or in the opposite direction. This quote cannot therefore be a complete explanation for their results in the case of short-range ember transport, and it is not clear whether the use of the terminal-velocity assumption results in a systematic bias in ember travel distances when modelling long-range transport.

In this chapter an investigation is made into whether the terminal-velocity assumption is appropriate when modelling ember transport in turbulent wind fields (Thomas et al. 2017a). A LEM is used to simulate a turbulent plume resulting from a static heat source in a turbulent boundary layer. This is similar to the simulations of Thurston et al. (2017). Using this simulated wind field, ember transport calculations are carried out with and without making the terminal-velocity assumption, and the results are compared. Individual ember trajectories are not examined; instead the focus is on the density of ember landings both because this allows a large number of embers to be treated ($\approx 3 \times 10^6$), and because this density is an important determinant of the likelihood of spot-fire ignition. There was no intention

to produce realistic ember-landing distributions; rather, this is an effort to assess whether the terminal-velocity assumption is justified when modelling long-range ember transport in turbulent wind fields. These simulations do not include the effects of in-flight combustion which will have a significant effect on ember trajectories but not on the conclusions of this study, since combustion occurs at time scales longer than those characteristic of the turbulent flow modelled here, and because we are assessing the differences between trajectories modelled with and without the terminal-velocity assumption. This is discussed further in Section 6.3.2. Much of the material presented in this chapter was published in (Thomas et al. 2017a).

6.2 The model

6.2.1 Large eddy simulation of turbulent boundary layer

In the first stage of the modelling, the WRF model (Skamarock et al. 2008) was used in LEM mode to spin up a turbulent boundary layer in a computational domain of $40 \times 16 \times 12$ kilometres ($x \times y \times z$). A horizontal resolution of 50 metres was used. This resolution was to a large extent dictated by limitations on computational time and data storage and at this resolution velocity gradients close to the fire may not be fully captured. This is a limitation of the study which may affect the results of this section, and the sensitivity of these results to horizontal resolution is worthy of future study. The vertical coordinate system consisted of 256 levels spaced at ≈ 10 metres at the surface, increasing to ≈ 50 metres at the model top (the modified code discussed in Section 3.4.3 was used to set the initial vertical resolution). In practice, the vertical spatial resolution may vary slightly during a simulation because of the pressure-based vertical coordinate system used by the WRF model (Skamarock et al. 2008). Periodic boundary conditions were used for the lateral boundaries, so that the developing turbulent eddies are recycled as they cross the downwind boundary during the spin-up phase. A 1000-metre-deep Rayleigh-damping layer was used

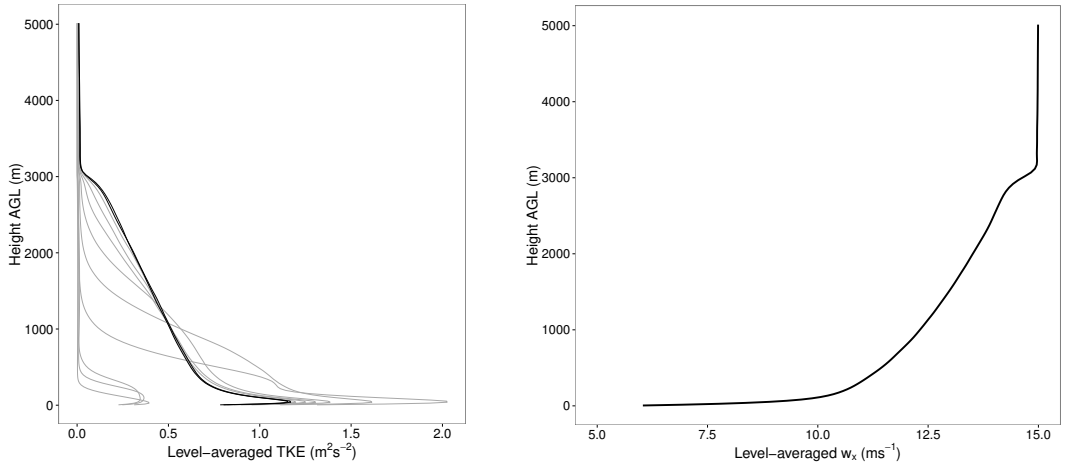

(a) Level-averaged TKE (b) Level-averaged w_x

Figure 6.1: (a) Evolution of total (subgrid scale + resolved) turbulence kinetic energy (TKE) during the spin-up phase of the simulation. The grey lines show the level-averaged TKE hourly for the first 9 hours. The black lines (almost identical) show the level-averaged TKE at $t = 10{:}00$ and $t = 11{:}00$ hours. (b) Level-averaged x-component of wind field w_x at $t = 10{:}00$ hours, immediately prior to application of sensible heat flux.

at the top of the model domain. Turbulence was parametrised using a 1.5 order turbulent kinetic energy (TKE) scheme (Deardorff 1980; Skamarock et al. 2008).

The model was initialised with a 3-kilometre-deep dry-adiabatic layer with an almost constant potential temperature of $\theta = 300$ K. Small random perturbations of θ were introduced in this layer to stimulate the development of turbulence. This dry-adiabatic layer was topped by a stable layer with a lapse rate of 3 K per kilometre. The initial wind profile consisted of a constant value of $w_x = 15\ \mathrm{m\,s^{-1}}$ over the entire model depth, with $w_y = w_z = 0$.

The model was run for 10 hours of model time, after which a turbulent boundary layer had developed; the vertical profile of TKE had stabilised (Figure 6.1(a)), and the level-averaged value of w_x had assumed the vertical profile seen in Figure 6.1(b), consistent with a shear-driven turbulent boundary layer (Moeng and Sullivan 1994).

6.2.2 Development of simulated plume

Once a turbulent boundary layer had developed, a plume was simulated by introducing a heat source at the lower boundary of the model domain. This was done by modifying the WRF-Fire code which, during a coupled atmosphere-fire simulation, inputs sensible and latent heat fluxes to the WRF atmospheric model (Section 3.3.4). In the full WRF-Fire model these fluxes are derived from a semi-empirical fire-spread submodel; the modified code simulates a static heat flux (Section 3.4.2). Following Thurston et al. (2013) (see also Thurston et al. 2017), a circular surface sensible-heat-flux anomaly was used, with intensity 10^5 $\mathrm{W\,m^{-2}}$, radius 250 metres, and located 2 kilometres inside the upwind boundary of the computational domain. No latent heat (i.e. moisture) flux was used. The simulation was restarted with this heat-flux anomaly and, to allow the plume to develop and stabilise, was continued for one hour of model time. The simulation was then continued for another hour during which data were collected at 5-second intervals. It is these data that were used to compute ember trajectories. Figure 6.2(a - c) shows cross sections of the turbulent wind field within the plume at the beginning of this period. The structure of the plume is consistent with that simulated by Thurston et al. (2017) (their Fig. 1). The leading edge exhibits a series of thermals which rise above the main part of the plume (Figure 6.2(c)), some of which extend above the mixed layer which ends at 3 kilometre. Vertically-oriented vortical structures are evident, for example at coordinates $(8, 8.5)$ in Figure 6.2(a), and $(10.5, 8.5)$ in Figure 6.2(b). Figure 6.2(d) shows the average vertical velocity $\overline{w}_z$ over the one-hour period for which ember trajectories were computed.

The choice of the shape of the heat-flux anomaly is to some extent arbitrary; a circular shape was used to enable a comparison of the results with those of Thurston et al. (2013). It might be argued that a lineal shape with a relatively shallow region of strong heating is more representative of many wildfires. However the importance

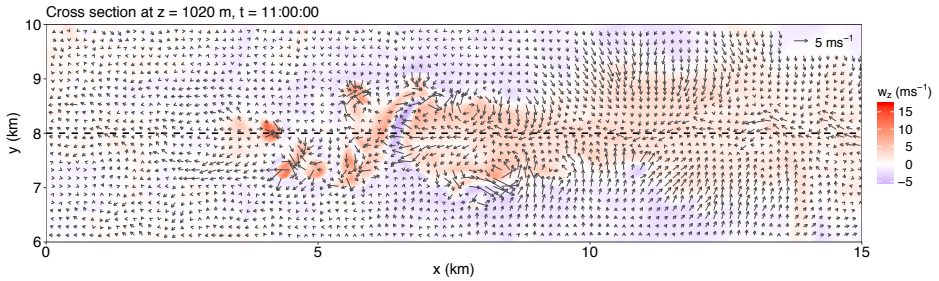

(a) **w**: horizontal cross section at $z = 1.020$ kilometres.

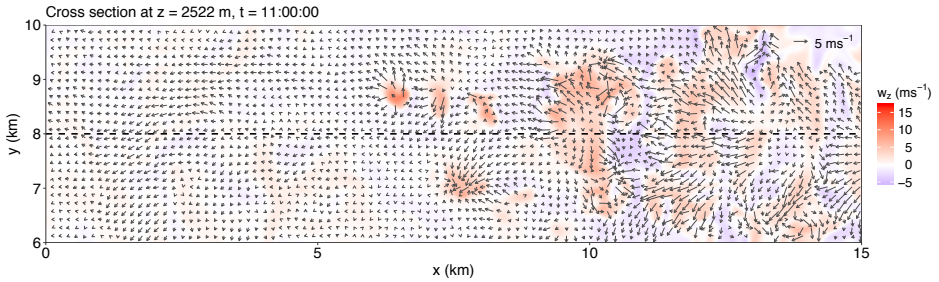

(b) **w**: horizontal cross section at $z = 2.522$ kilometres.

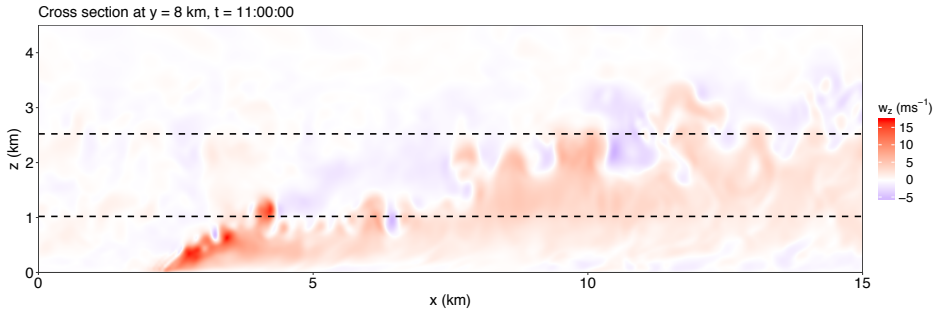

(c) w_z: vertical cross section at $y = 8$ kilometre.

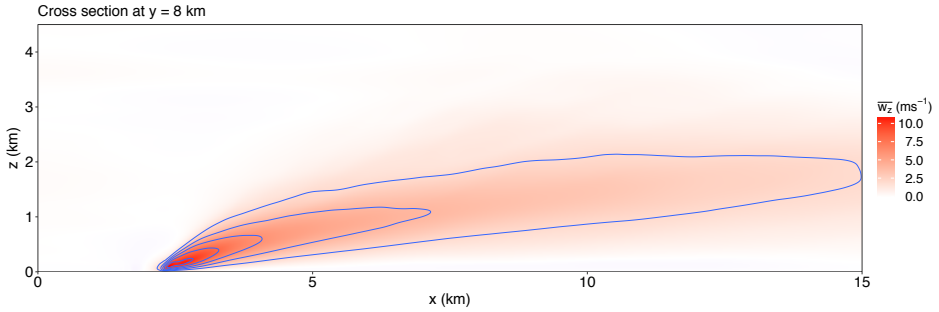

(d) $\overline{w}_z$: vertical cross section at $y = 8$ kilometres.

Figure 6.2: Horizontal and vertical cross sections through the plume. Panels (a) to (c) show instantaneous velocity **w** at $t = 11{:}00{:}00$ hrs, the time at which ember release begins. Vertical velocity is indicated by the colour scale, and the vectors represent the horizontal velocity perturbations from the level-averaged values of Figure 6.1(b). Panel (d) shows time-averaged vertical velocity $\overline{w}_z$ for the one-hour period starting at $t = 11{:}00{:}00$ hrs, with contours drawn at $\overline{w}_z = 2$, 4, 6, 8, and 10 $\mathrm{m\,s^{-1}}$.The locations of the cross sections are indicated by dashed lines.

of large areal regions of intensive heating in the development of very large wildfires has been discussed in Sections 1.3, 1.4 and 1.5. Further, Thurston et al. (2017) justify this choice of shape by pointing to the arguments of Bejan et al. (2014) which show that flat plumes evolve into round plumes within relatively short distances.

6.2.3 Equations of ember trajectories

In their work, Thurston et al. (2017) assumed ember velocities $\mathbf{u}$ were given by

$$\mathbf{u} = \mathbf{w} - \tilde{u}_\infty \mathbf{k} \tag{6.1}$$

where $\tilde{u}_\infty$ is a constant. Eqn. (6.1) will be referred to as the *constant terminal-velocity assumption*. This is a rather strong form of the terminal-velocity assumption because, according to Eqn. (2.12), the terminal fall speed u_∞ of an ember depends on the atmospheric density ρ. In this study the constant $\tilde{u}_\infty$ in Eqn. (6.1) is interpreted as the terminal fall speed of an ember at some reference atmospheric density ρ_0, so that

$$\tilde{u}_\infty = \sqrt{\frac{2m_\mathrm{e}g}{C_\mathrm{d}\rho_0 A_\mathrm{p}}}. \tag{6.2}$$

One might think of ρ_0 as the atmospheric density at the location of the experiments used to determine $\tilde{u}_\infty$, and in this study $\rho_0 = 1.16\ \mathrm{kg\,m^{-3}}$ is used, which is the approximate atmospheric density at sea level. This is a reasonable but arbitrary choice; changes in the value of ρ_0 are equivalent to a scaling of the value of $\tilde{u}_\infty$.

Using Eqn. (6.2), Eqn. (2.10) can be rewritten as

$$\frac{\mathrm{d}\mathbf{u}}{\mathrm{d}t} = g\frac{\rho}{\rho_0}\frac{1}{\tilde{u}_\infty^2}|\mathbf{w} - \mathbf{u}|(\mathbf{w} - \mathbf{u}) + \mathbf{g}. \tag{6.3}$$

The differences between motion under Eqn. (6.1) and Eqn. (6.3) are twofold: Eqn. (6.3) takes into account both the momentum of the embers, and changes in ρ. The term ρ/ρ_0 in Eqn. (6.3) can be significantly different from 1, both at higher altitudes and within the plume, and it is likely that this will be an important factor contributing to any differences in ember motion under Eqn. (6.1) and Eqn. (6.3). An intermediate formulation which isolates this effect can be found by substituting Eqn. (6.2) into Eqn. (2.13), giving

$$\mathbf{u} = \mathbf{w} - \sqrt{\frac{\rho_0}{\rho}}\tilde{u}_\infty \mathbf{k}. \tag{6.4}$$

This is the asymptotic solution of Eqn. (6.3) and we will refer to motion under Eqn. (6.4) as motion under the *variable terminal-velocity assumption*.

The only ember characteristic explicitly appearing in each of Eqns. (6.1), (6.3), and (6.4) is $\tilde{u}_\infty$, the terminal fall speed of the ember at the reference atmospheric density ρ_0. This makes it convenient to compare motion under these three equations since one need only specify a set of embers with initial positions $\mathbf{x}_0$ and terminal fall speeds $\tilde{u}_\infty$, and apply each of Eqns. (6.1), (6.3), and (6.4) to compute the trajectories of the embers in that set.

For non-spherical embers the quantities C_d and A in Eqn. (6.2) depend on the orientation of the ember with respect to the relative wind velocity $\mathbf{w} - \mathbf{u}$. In the formulation presented here it is implicitly assumed that these quantities remain constant during ember transport. This amounts to assuming that the ember always has the same orientation with respect to $\mathbf{w}-\mathbf{u}$, or that it adopts such an orientation over time scales much smaller than those over which $\mathbf{w}-\mathbf{u}$ changes. This assumption is similar in nature to the terminal-velocity assumption. The investigation of its validity for long range ember transport is beyond the scope of this thesis, however it should be noted that it is supported to some extent by the studies of Ellis (2010) and Tarifa et al. (1967); in drop tests, embers either assumed an orientation of maximum drag, or tumbled but fell at a speed as if they had assumed such an orientation.

Some numerical studies, including those of Koo et al. (2012) and Oliveira et al. (2014), include the rotational terms in the equations of motion.

6.2.4 Ember initialisation

Embers were released every 5 seconds for the first 30 minutes of the ember transport phase of the modelling. Embers were initialised at heights between 5 and 50 metres, at locations where $w_z > 5$ m s^{-1}. Within these constraints, the initial positions of embers were chosen randomly, with an average separation of 5 metres. These parameters are somewhat arbitrary however it should be remembered that the purpose of the current study is not to simulate realistic ember landing distributions but to compare the differences in simulated ember landing distributions using three different ember transport assumptions. That being said, the range of release heights (5 to 50 metres) seems reasonable having regard to the vertical grid resolution near the surface ($\sim$ 10 metres) and the height of tall eucalypt forests. The requirement of a minimum vertical wind velocity of 5 m s^{-1} for ember launch also seems reasonable given the range of terminal velocities considered (3 to 8 m s^{-1}). The parameter controlling average separation (set at 5 metres) does not represent a known empirical fact or reasonable estimate, but was used to control the number of embers released in the numerical experiments; with these settings 3,280,660 embers were released in the first 30 minutes of the simulation, and tests showed that increasing the number of embers by reducing the average separation did not substantially alter the results. Embers were assigned a terminal fall speed, $\tilde{u}_\infty$; values of $\tilde{u}_\infty = 3$, 6, and 8 m s^{-1} were used. These values are representative of those from previous experimental and numerical studies: Ellis (2010) measured terminal velocities in the range of 2.5 to 8 m s^{-1} for samples of eucalyptus bark; and Thurston et al. (2017) modelled ember transport for $\tilde{u}_\infty = 5, 6, 7, 8$ and 9 m s^{-1}. The same set of initial ember positions and starting times was used for each choice of $\tilde{u}_\infty$. The reader may refer to (Ellis 2010) for further details of the embers tested.

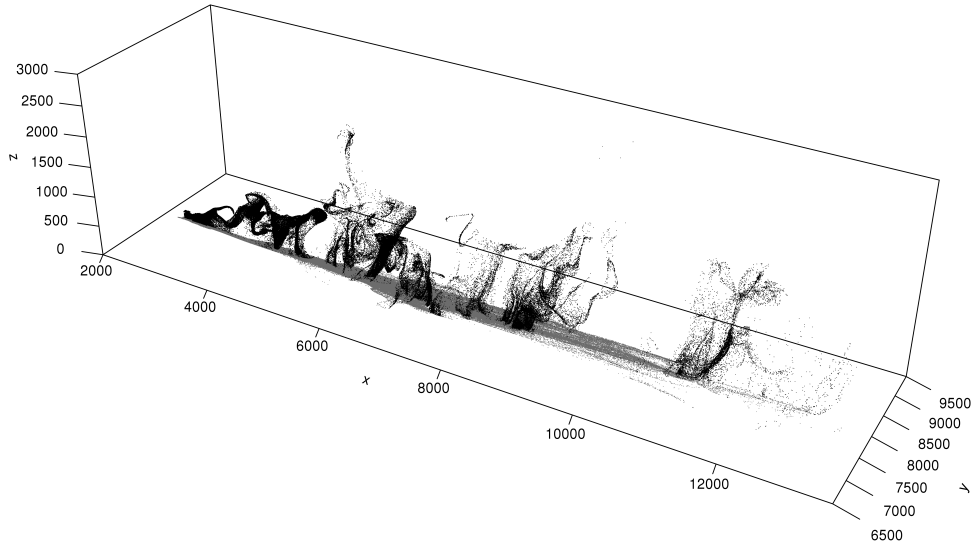

Figure 6.3: Modelled embers in flight (black points), and after landing (grey points), 15 minutes into the ember transport phase of the modelling. In this case trajectories were computed using Eqn. (6.3), with $\tilde{u}_\infty = 6\ \mathrm{m\,s^{-1}}$.

Figure 6.3 depicts embers in flight, modelled using Eqn. (6.3), with $\tilde{u}_\infty = 6\ \mathrm{m\,s^{-1}}$.

6.2.5 Numerical methods

The standard Runge-Kutta explicit second-order scheme (RK2) was used to compute trajectories under Eqns. (6.1), (6.3), and (6.4). Thus for Eqn. (6.4), if $\mathbf{x}_{t_0}$ is the estimate of the position of an ember at time t_0, one first computes a temporary estimate at time $t_0 + \delta t/2$,

$$\mathbf{x}^* = \mathbf{x}_{t_0} + \left(\mathbf{w}(\mathbf{x_{t_0}}, t_0) - \sqrt{\frac{\rho_0}{\rho(\mathbf{x}_{t_0}, t_0)}} \tilde{u}_\infty \mathbf{k} \right) \frac{\delta t}{2},$$

and then estimates $\mathbf{x}$ at time $t_0 + \delta t$ as

$$\mathbf{x}_{t_0+\delta t} = \mathbf{x}_{t_0} + \left(\mathbf{w}(\mathbf{x}^*, t_0 + \delta t/2) - \sqrt{\frac{\rho_0}{\rho(\mathbf{x}^*, t_0 + \delta t/2)}} \tilde{u}_\infty \mathbf{k} \right) \delta t.$$

Here, $\mathbf{w}(\mathbf{x},t)$ and $\rho(\mathbf{x},t)$ are interpolated linearly in time and space from the LEM output (Section 6.2.2). The method for Eqn. (6.1) is the same, but with $\rho_0/\rho \equiv 1$. Eqn. (6.3), which is of second order, was converted to a first-order system in the usual way:

$$\begin{aligned} \frac{\mathrm{d}\mathbf{x}}{\mathrm{d}t} &= \mathbf{u} \\ \frac{\mathrm{d}\mathbf{u}}{\mathrm{d}t} &= \mathbf{a}(\mathbf{u},\mathbf{x},t) \end{aligned}$$

where

$$\mathbf{a}(\mathbf{u},\mathbf{x},t) = g\frac{\rho(\mathbf{x},t)}{\rho_0}\frac{1}{\tilde{u}_\infty^2}|\mathbf{w}(\mathbf{x},t)-\mathbf{u}|(\mathbf{w}(\mathbf{x},t)-\mathbf{u})+\mathbf{g}. \tag{6.5}$$

If $\mathbf{x}_{t_0}$ and $\mathbf{u}_{t_0}$ are estimates of the position and velocity of an ember at time t_0, then one computes in turn:

$$\begin{aligned} \mathbf{x}^* &= \mathbf{x}_{t_0} + \mathbf{u}_{t_0}\frac{\delta t}{2} \\ \mathbf{u}^* &= \mathbf{u}_{t_0} + \mathbf{a}(\mathbf{u}_{t_0},\mathbf{x}_{t_0},t_0)\frac{\delta t}{2} \\ \mathbf{x}_{t_0+\delta t} &= \mathbf{x}_{t_0} + \mathbf{u}^*\delta t \\ \mathbf{u}_{t_0+\delta t} &= \mathbf{u}_{t_0} + \mathbf{a}(\mathbf{u}^*,\mathbf{x}^*,t_0+\delta t/2)\delta t. \end{aligned}$$

For Eqns. (6.1) and (6.4) the time step used was $\delta t = 0.05$ seconds, with $\delta t = 0.01$ seconds for Eqn. (6.3). This choice of numerical method and time step is discussed further in Section 6.3.4. The initial conditions for Eqns. (6.1) and (6.4) are simply $\mathbf{x}(t_0) = \mathbf{x}_0$, where t_0 is the ember release time and $\mathbf{x}_0$ is the initial position of the ember (Section 6.2.4). The initial conditions for Eqn. (6.3) were taken to be $\mathbf{x}(t_0) = \mathbf{x}_0$, $\mathbf{u}(t_0) = \mathbf{w}(\mathbf{x}_0,t_0) - \tilde{u}_\infty\mathbf{k}$. Thus in all cases the ember is assumed to be initially travelling at approximately its terminal velocity (neglecting

the factor ρ_0/ρ). In practice, because of the rapid approach to terminal velocity, the precise choice of initial velocity will have little effect on the results overall.

6.3 Results and discussion

Figure 6.4 shows the two-dimensional landing distributions under the three transport assumptions for embers with $\tilde{u}_\infty = 6\ \mathrm{m\,s^{-1}}$. The points are coloured according to the density of landings at each location, estimated using a Gaussian kernel density estimator. Travel distances, and the density of embers travelling long distances, are clearly higher under the constant-terminal-velocity assumption than those computed without any terminal-velocity assumption, with those computed using the variable-terminal-velocity assumption taking an intermediate position.

Figure 6.4 is difficult to interpret quantitatively, so we focus now on travel distances rather than two-dimensional landing distributions. Figure 6.5 shows the distributions of travel distances for embers with $\tilde{u}_\infty = 3$, 6, and 8 $\mathrm{m\,s^{-1}}$ under the three transport assumptions. In all three cases, motion under the constant terminal-velocity assumption (Eqn. (6.1)) results in a significantly higher density of embers flying longer distances than under either of Eqn. (6.3), no terminal-velocity assumption, or Eqn. (6.4), the variable terminal-velocity assumption. (When interpreting Figure 6.5 one should note the logarithmic scale on the vertical axis.) The differences between the constant and variable terminal-velocity assumptions are due solely to the variations in atmospheric density ρ: both in the plume, and at higher altitudes, ρ will be lower than the reference value of $\rho_0 = 1.16\ \mathrm{kg\,m^{-3}}$, resulting in higher terminal fall speeds and consequently shorter travel distances. For the cases $\tilde{u}_\infty = 6$ and 8 $\mathrm{m\,s^{-1}}$ (Figure 6.5(b) and (c)), motion under the variable terminal-velocity assumption results in significantly higher ember densities at longer distances than when no terminal-velocity assumption is made. For example, for $\tilde{u}_\infty = 6\ \mathrm{m\,s^{-1}}$ the density of embers travelling 15,000 metres is approximately 14

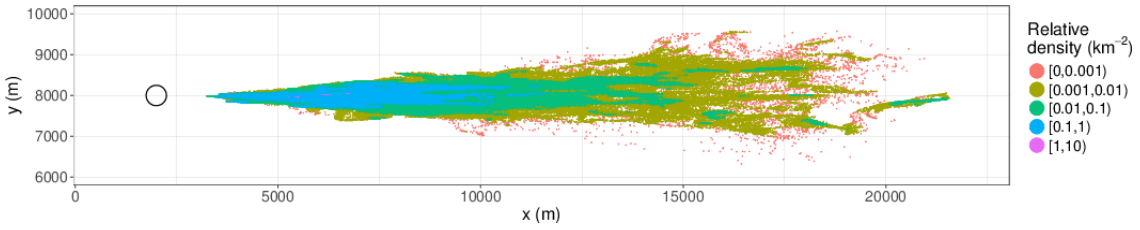

(a) Constant-terminal-velocity assumption

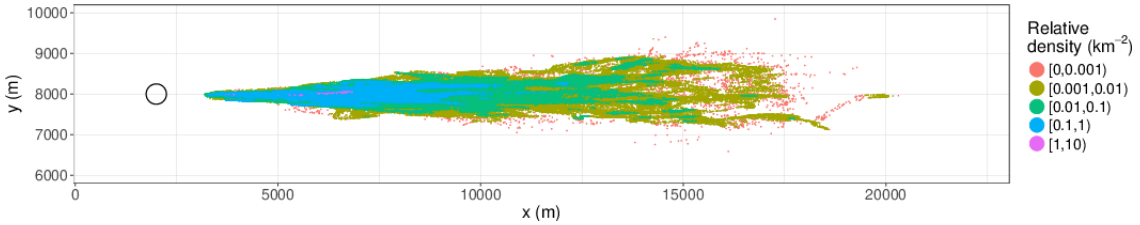

(b) Variable-terminal-velocity assumption

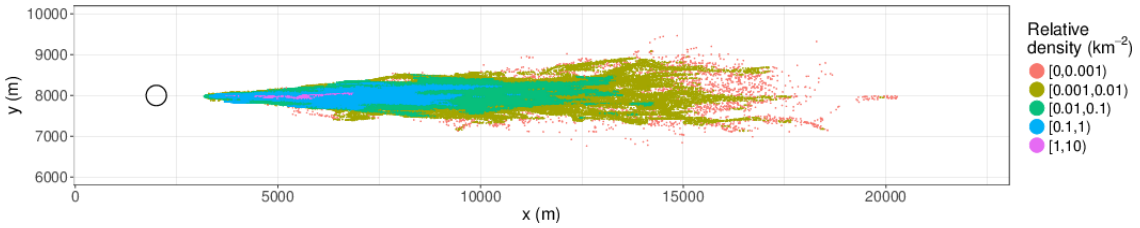

(c) No terminal-velocity assumption

Figure 6.4: Location and density of ember landings for embers with $\tilde{u}_\infty = 6$ m s^{-1} under: (a) Eqn. (6.1), the constant-terminal-velocity assumption; (b) Eqn. (6.4), the variable-terminal-velocity assumption; (c) Eqn. (6.3), no terminal-velocity assumption. Only embers that were transported at least 1 kilometre under all three assumptions are included, 875,108 in total. Colours represent the density of landings per km^2 as a proportion of the total landings, computed using a Gaussian kernel density estimator. The circle shows the location and extent of the heat source used to generate the plume.

times higher under the constant terminal-velocity assumption, and approximately 5 times higher under the variable terminal-velocity assumption, than it is if no terminal-velocity assumption is used. This is an important finding. In reality, not every ember that lands will ignite a spot fire so any modelling of spot-fire development will almost certainly be partly stochastic, with the probability of ignition dependent on, among other things, ember landing densities. If this type of direct simulation of ember trajectories was used to model spot-fire development then these results indicate that the use of the terminal-velocity assumption would result in a significantly higher modelled probability of long-range spot-fire ignition.

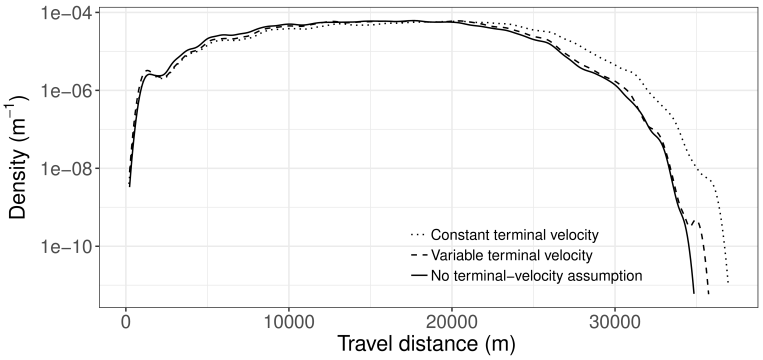

(a) $\tilde{u}_\infty = 3\ \mathrm{m\,s^{-1}}$.

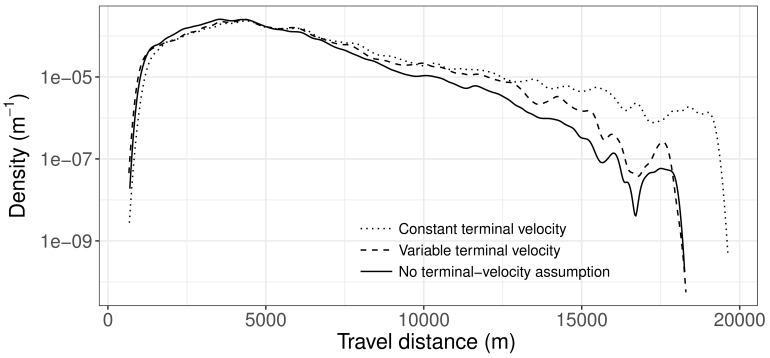

(b) $\tilde{u}_\infty = 6\ \mathrm{m\,s^{-1}}$.

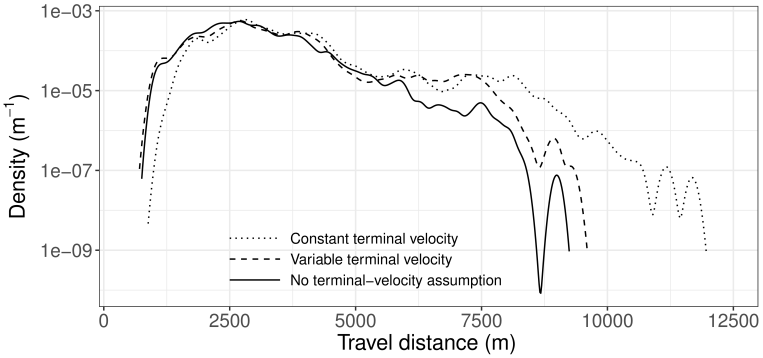

(c) $\tilde{u}_\infty = 8\ \mathrm{m\,s^{-1}}$.

Figure 6.5: Distributions of travel distances for embers with: (a) $\tilde{u}_\infty = 3\ \mathrm{m\,s^{-1}}$, (b) $\tilde{u}_\infty = 6\ \mathrm{m\,s^{-1}}$, and (c) $\tilde{u}_\infty = 8\ \mathrm{m\,s^{-1}}$. Only embers that have travelled further than 1 kilometre under all three assumptions are included.

How does the value of $\tilde{u}_\infty$ affect the results? For small values of $\tilde{u}_\infty$ the coefficient $1/\tilde{u}_\infty^2$ in Eqn. (6.3) is larger, so that the damping effect of the drag force is larger and the ember will approach its terminal velocity more quickly. Thus we expect smaller differences between motion under the variable terminal-velocity assumption (Eqn. (6.4)) and no terminal-velocity assumption (Eqn. (6.3)), both of which take into account varying atmospheric density ρ. This is in agreement with Figure 6.5(a),

which shows distributions of travel distances when $\tilde{u}_\infty = 3\ \mathrm{m\,s^{-1}}$. There are still significant differences between motion under Eqn. (6.3) and Eqn. (6.1); the latter neglects the effects of atmospheric density on the terminal fall speed. Ember travel densities for embers with $\tilde{u}_\infty = 8\ \mathrm{m\,s^{-1}}$ (Figure 6.5(c)) exhibit a similar pattern to Figure 6.5(b) for embers with long travel distances.

6.3.1 Proposed mechanism and comparison with earlier study

In their study of short-range ember transport, Koo et al. (2012) found that using the terminal-velocity assumption underestimated ember transport distances, and they attributed this to 'the notion of a firebrand being thrown by locally strong winds' when momentum is included in the equations of motion. This notion also explains our results which at first sight may appear at odds with those of Koo et al. (2012). In the present study embers are transported long distances because they are held aloft by the plume. When they leave the plume they fall to the ground, all the while being transported by the ambient wind. When modelled using Eqn. (6.3), embers have momentum and will not react instantaneously to changes in the turbulent wind field. This makes them more likely to leave the plume earlier, both because they are more likely to fall out if they don't respond quickly enough to an updraft that would keep them in the plume, or because they are thrown out by local turbulent motions. As noted earlier, turbulence and gradient changes at scales smaller than the grid resolution are not captured in these simulations and this is a limitation of the model.

6.3.2 Flight times and possible effects of combustion

Figure 6.6 shows flight times and travel distances for the case of $\tilde{u}_\infty = 6\ \mathrm{m\,s^{-1}}$ under the constant terminal-velocity assumption (Eqn. (6.1)) and no terminal-velocity assumption (Eqn. (6.3)) and further illustrates that many more embers are transported long distances under the former. Simulated flight times of some embers are

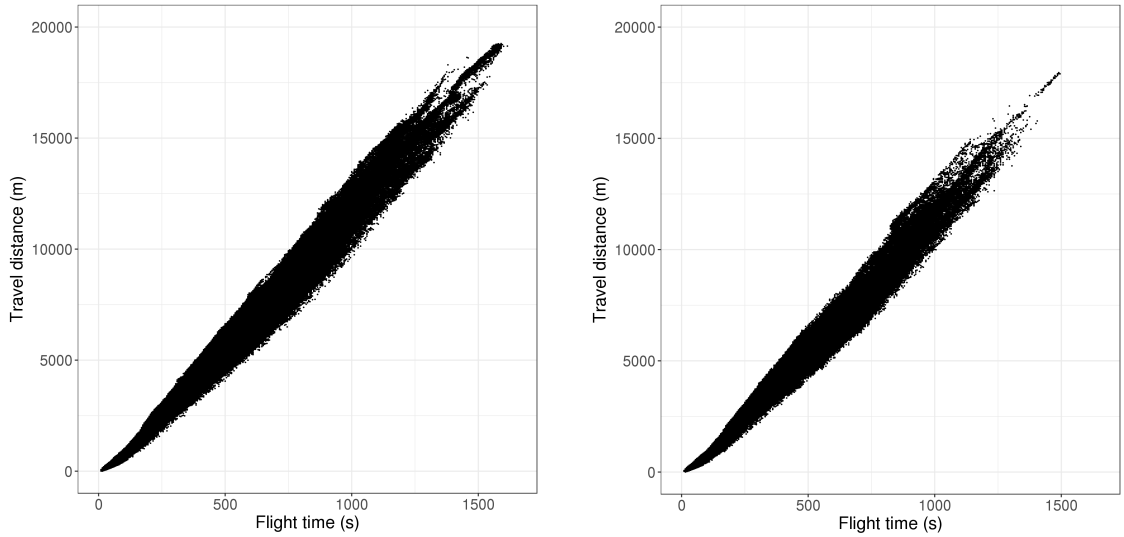

(a) Constant terminal-velocity assumption (b) No terminal-velocity assumption

Figure 6.6: Flight times and travel distances for embers with $\tilde{u}_\infty = 6\ \mathrm{m\,s^{-1}}$ under: (a) the constant terminal-velocity assumption, and (b) no terminal-velocity assumption.

25 minutes or longer, with travel distances approaching 20 kilometres. Real embers are capable of travelling these distances (and further) while remaining alight and retaining sufficient mass to ignite spot fires (see e.g. Tolhurst 2009). However such long flight times raise the question of whether incorporating combustion of embers into the model would significantly alter the results of this study, or its relevance. On the one hand changes to the aerodynamic characteristics of an ember occur on time scales longer than those associated with the turbulent motion of a plume so that, with the reasoning of Section 6.3.1, incorporating momentum into the modelling of the trajectory of an ember, burning or not, will increase the likelihood of it leaving the plume early. On the other hand, in the case of long-range spotting one need only consider embers which have sufficient mass to be able to sustain combustion for the period that they are aloft. This may constrain the values of $\tilde{u}_\infty$ that these embers can initially have; furthermore combustion is likely to alter these values during the flight of an ember. Further work needs to be done to see how this would affect the results presented here.

6.3.3 Adequacy of sampling rate: spectral analysis of plume data

The atmospheric model was run using a computational time step of 0.1 seconds but constraints on data storage dictate the use of a lower sampling rate for the data used to compute ember trajectories; a rate of 0.2 Hz was used (Section 6.2.2). To assess the adequacy of this sampling rate the vertical wind component w_3 was output at 1 Hz for the one-hour period over which the transport computations were made and these data were used to analyse the variation over time of the vertical component of the wind field within the plume. Various locations within the plume were analysed; Figure 6.7 shows the results at a location 1250 metres downwind of the downwind edge of the heat anomaly, at the pixel within this cross-section which had the greatest range over t of values of w_3. The results at other locations within the plume are similar. Figure 6.7(a) exhibits the puffing behaviour seen in buoyant plumes (see for example Cetegen and Ahmed 1993, and also Figure 6.2(c)). While Figure 6.7(b), does not indicate the existence of a dominant puffing frequency, it does show a rapid roll off in spectral density starting at approximately 0.03 Hz. This justifies the use of a 0.2 Hz sampling rate to capture the plume velocity. This is illustrated further by Figure 6.7(a): in computing ember trajectories the 0.2 Hz data are interpolated linearly in time; clearly, linear interpolation between the dots in Figure 6.7(a) provides a good representation of the 1 Hz sampled data (the solid line).

6.3.4 Stability and accuracy of numerical scheme

The RK2 scheme (Section 6.2.5) was found to be numerically unstable when attempting to integrate Eqn. (6.3) with $\tilde{u}_\infty = 2\ \mathrm{m\,s^{-1}}$ and $\delta t = 0.05$ second (results for $\tilde{u}_\infty = 2\ \mathrm{m\,s^{-1}}$ are not presented here). Eqn. (6.3) appears to be stiff and requires very small time steps for smaller values of $\tilde{u}_\infty$. It was possible to integrate Eqn. (6.3) with $\tilde{u}_\infty = 2\ \mathrm{m\,s^{-1}}$ using RK2 with $\delta t = 0.01$ seconds, however this raises questions as to the accuracy of this scheme. To assess this we compared the results

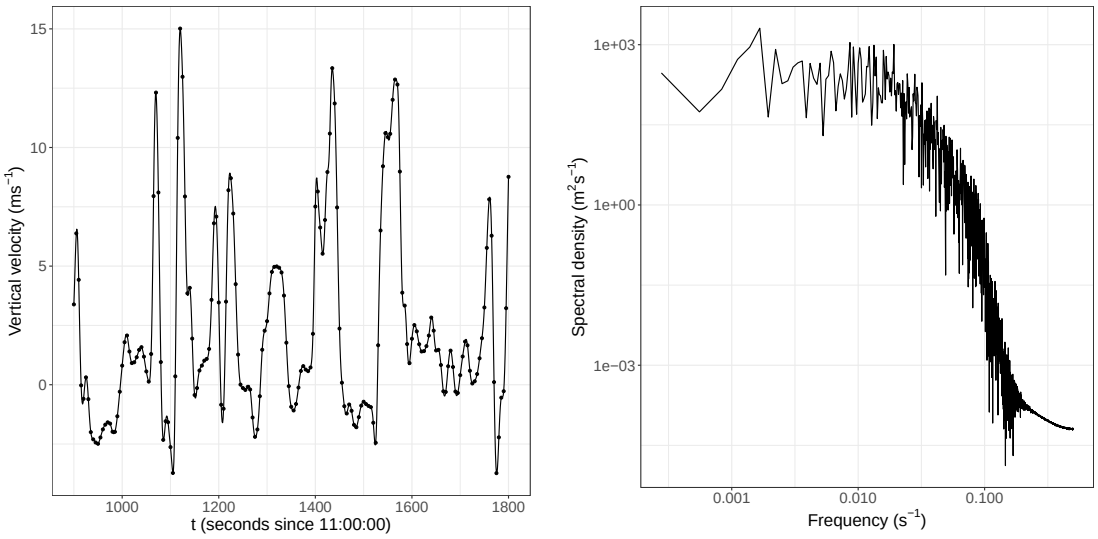

(a) Time domain (b) Frequency domain

Figure 6.7: Time variation of vertical velocity at a location in the plume 1250 metres downwind of the downwind edge of the heat anomaly: (a) 15 minute window of w_3; the dots show the data sampled at 0.2 Hz, the solid line shows the data sampled at 1 Hz. (b) Spectrum of 1 hour time series of w_3 starting at $t = 11{:}00{:}00$, computed using data sampled at 1 Hz.

for Eqn. (6.3) with those obtained using the standard fourth-order Runge-Kutta scheme (RK4), which was implemented as follows: if $\mathbf{x}_{t_0}$ and $\mathbf{u}_{t_0}$ are estimates of the position and velocity of an ember at time t_0 then, with $\mathbf{a}(\mathbf{u}, \mathbf{x}, t)$ as defined by Eqn. (6.5), we set $\mathbf{a}_0 = \mathbf{a}(\mathbf{u}_{t_0}, \mathbf{x}_{t_0}, t_0)$ and compute

$$\begin{aligned}
\mathbf{x}^* &= \mathbf{x}_{t_0} + \mathbf{u}_{t_0}\frac{\delta t}{2}, & \mathbf{u}^* &= \mathbf{u}_{t_0} + \mathbf{a}_0\frac{\delta t}{2}, & \mathbf{a}^* &= \mathbf{a}(\mathbf{u}^*, \mathbf{x}^*, t_0 + \frac{\delta t}{2}),\\
\mathbf{x}^{**} &= \mathbf{x}_{t_0} + \mathbf{u}^*\frac{\delta t}{2}, & \mathbf{u}^{**} &= \mathbf{u}_{t_0} + \mathbf{a}^*\frac{\delta t}{2}, & \mathbf{a}^{**} &= \mathbf{a}(\mathbf{u}^{**}, \mathbf{x}^{**}, t_0 + \frac{\delta t}{2}),\\
\mathbf{x}^{***} &= \mathbf{x}_{t_0} + \mathbf{u}^{**}\delta t, & \mathbf{u}^{***} &= \mathbf{u}_{t_0} + \mathbf{a}^{**}\delta t, & \mathbf{a}^{***} &= \mathbf{a}(\mathbf{u}^{***}, \mathbf{x}^{***}, t_0 + \delta t),
\end{aligned}$$

and finally

$$\begin{aligned}
\mathbf{x}_{t_0+\delta t} &= \mathbf{x}_{t_0} + \frac{1}{6}\left(\mathbf{u}_{t_0} + 2\mathbf{u}^* + 2\mathbf{u}^{**} + \mathbf{u}^{***}\right)\delta t,\\
\mathbf{u}_{t_0+\delta t} &= \mathbf{u}_{t_0} + \frac{1}{6}\left(\mathbf{a}_0 + 2\mathbf{a}^* + 2\mathbf{a}^{**} + \mathbf{a}^{***}\right)\delta t.
\end{aligned}$$

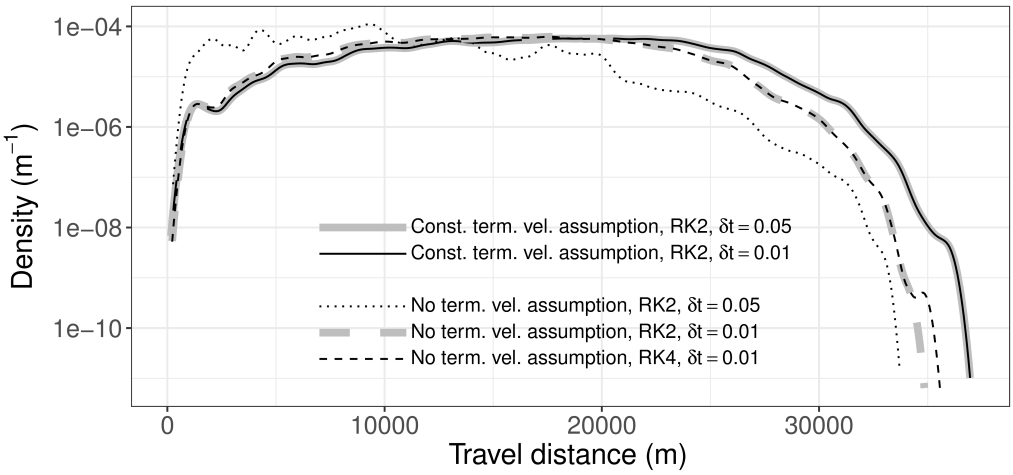

Figure 6.8: Comparison of results using various time steps and numerical schemes for embers with $\tilde{u}_\infty = 3\ \mathrm{m\,s^{-1}}$.

Results of the comparison for embers with $\tilde{u}_\infty = 3\ \mathrm{m\,s^{-1}}$ are depicted in Figure 6.8. For Eqn. (6.3), there was good agreement between RK2 and RK4, using $\delta t = 0.01$ second. There is a slight difference at the tail of the distributions; this region contains few landing positions and the kernel density estimator is sensitive to slight differences in that region. RK2 with $\delta t = 0.05$ second is clearly not accurate.

Numerical stability is not at issue when integrating Eqns. (6.1) and (6.4). To assess the accuracy of the RK2 scheme for these equations, the results using $\delta t = 0.05$ seconds and $\delta t = 0.01$ seconds were compared; the results appear identical (see Figure 6.8). In fact a larger value of δt could probably have been used with little loss of accuracy since, numerically, the right hand sides of Eqns. (6.1) and (6.4) are piecewise linear functions, because they are interpolated linearly from the LEM data.

The present study was concerned only with the differences between modelled ember transport using Eqns. (6.1), (6.3), and (6.4). The explicit, fixed-time-step Runge-Kutta schemes RK2 and RK4 were chosen primarily because of the ease with which they can be implemented. In a more comprehensive study they may not prove to be the best choice, particularly for Eqn. (6.3) where an adaptive time step scheme, or

an implicit scheme, may be more appropriate. Furthermore, the appropriate choices of δt are likely to depend on the values of δx, δy and δz used in the simulations.

6.4 Conclusion

In this chapter the validity of the terminal-velocity assumption was examined by simulating ember transport using data from a large eddy simulation of a turbulent plume. Two forms of the terminal-velocity assumption were studied: the constant terminal-velocity assumption, which neglects both ember momentum and variations in atmospheric density; and the variable terminal-velocity assumption, which neglects ember momentum but takes into account the atmospheric density at the location of the ember. Ember landing distributions computed under these assumptions were compared with those computed using the equations of motion derived from the quadratic drag law, in which both ember momentum and atmospheric density are accounted for. Rotational motion of the embers was not considered, nor were the effects of in-flight combustion. It was found that simulations using either version of the terminal-velocity assumption overestimated the density of long-range ember landings compared with simulations in which the terminal-velocity assumption is not made. This effect is greater for those embers with higher terminal fall speeds, and it is greater for the constant terminal-velocity assumption, which does not account for variations in atmospheric density.

In this study embers were transported long distances because they were held aloft for long periods of time by the turbulent plume. If the terminal-velocity assumption is not used, then the momentum of an ember increases the likelihood of it falling out, or being thrown out, of the plume because the ember does not react instantaneously to changes in the turbulent wind field; embers leave the plume earlier, and are not transported as far.

Although the effects of in-flight combustion on ember motion were not included in this study, it is likely that the conclusions would be similar if these effects were considered.

Chapter 7

Discussion and conclusion

Dynamic fire behaviour, such as that arising from fire-fire or fire-terrain interactions, is an important area of study, both because of its role in the development of large fires, and because it can cause rapid changes in fire behaviour which may be unexpected because they are not accompanied by changes in ambient conditions. This has obvious implications for operational personnel. In this thesis we have used a coupled atmosphere-fire model to study the dynamic behaviour resulting from the merging of two firelines at an acute angle (a junction fire). Similar enhanced fire behaviour also occurs when multiple spot fires coalesce, and junction fires play a role in the merging of spot fires; this has led us to an investigation of the modelling of ember transport in turbulent plumes.

Dynamic fire behaviour cannot be modelled with existing operational models which are predicated on assumptions of quasi-steady fire behaviour. In this thesis we have also used the the coupled atmosphere-fire framework to investigate the notion that fireline curvature might be used in computationally-efficient, operationally-capable fire-spread models as a proxy for some of the processes underlying dynamic fire behaviour.

7.1 Summary of results

In Chapter 4 a coupled atmosphere-fire model (WRF-Fire) was used to simulate the dynamic fire behaviour associated with junction fires. The model was able to reproduce the behaviour observed in laboratory-scale fires, despite the difference in scales of two orders of magnitude. The modelled dynamic behaviour was broadly attributed to two sources, which may be thought of as first- and second-order effects: the large-scale surface flow, influenced by the interaction between the two separate firelines (equivalently, by the geometry of the merged fireline); and small-scale vorticity, generated by the tilting of buoyancy-induced horizontal vorticity, causing sudden jumps in fire spread. This latter process is similar to that of dynamic fingering discussed by Clark et al. (1996a), who conjectured that it may be a major mechanism of fire spread at fine scales. Neither of these processes can be captured by current operational models which are based on empirical fire-spread models.

Since the geometry of the fireline influences fire behaviour, it is natural to look for geometric properties that might be used as proxies for the underlying causes of the dynamic behaviour, and fireline curvature has been suggested as one such property (Hilton et al. 2016; Sharples et al. 2013). In Chapter 5 this idea was investigated by looking for a relationship, at various scales, between curvature and rate of spread in the output of the coupled model. No such relationship was found at any scale in the simulations of junction fires or arc fires. WRF-Fire does not explicitly include radiation in its fire-spread model. However, convective processes are represented and in their analysis of experimental junction fires Raposo et al. (2018) concluded that the dynamic behaviour of junction fires is caused by pyroconvective mechanisms. Since WRF-Fire reproduces the junction-fire behaviour well, it seems reasonable to conclude that fireline curvature is not a satisfactory proxy for these convective processes. However, the investigation of these ideas has

led naturally to the pyrogenic-potential model of Hilton et al. (2018). While the pyrogenic-potential model was motivated by the work presented in Section 5.3, it was developed primarily by Dr James Hilton of the CSIRO (Hilton et al. 2018) and its original development does not form part of the work presented in this thesis.

In a sense, the pyrogenic-potential model is related to fireline-curvature-dependent models, since the Laplacian of a scalar field may be interpreted as a curvature. However, the pyrogenic-potential model has at least two advantages over a simple curvature-dependent model: it is a coupled model, albeit with a very simplified atmospheric component; and it has a physical basis. In Section 5.4 it was seen that the pyrogenic-potential model and the WRF-Fire coupled model behave in a similar fashion when used to model simple test cases involving fires ignited along circular arcs. It should be emphasised that the pyrogenic-potential model is a linear model, and can only be used to model first-order effects. If used to model junction fires, for example, it will reproduce the bulk characteristics of the fire-induced surface flow, but it will not reproduce the sudden jumps caused by small-scale vorticity, which can be captured by full atmosphere-fire coupled models like WRF-Fire.

In Chapter 6 we investigated the modelling of the transport of embers in a turbulent plume. It was found that if ember transport was modelled using the terminal velocity assumption then the density of long-range ember landings was significantly overestimated when compared with modelling using the full equations of motion of the ember. This difference was attributed to the increased likelihood that an ember will be ejected from the plume earlier if it is modelled as having momentum. This is significant for spot-fire modelling because such modelling will inevitably have a stochastic element, and the probability of spot-fire ignition will be directly related to ember-landing densities.

7.2 Conclusion and future work

7.2.1 Dynamic fire behaviour

The work presented in this thesis has significantly improved our understanding of dynamic fire behaviour and how to model it by:

- Isolating the mechanisms responsible for the dynamic fire behaviour of junction fires,
- Determining that fireline curvature is not a suitable proxy for these processes,
- Motivating the pyrogenic-potential model and making a comparison between it and a coupled atmosphere-fire model (WRF-Fire) when simulating arc fires, and
- Comparing wind fields from WRF simulations of static heat sources with those obtained from analytic solutions of the equations that govern the pyrogenic-potential model.

A critical issue for the pyrogenic-potential model is the determination of an appropriate form for the source term. In simulations performed so far, the source term has been defined to be $\nu = kI$ with I being some form of intensity, defined either by (3.5) or (3.6), and k being treated as a free parameter. It is possible that this is not the most appropriate form for $\nu = f(I)$. Preliminary simulations, not presented in this thesis, indicate that $\nu = kI^{\beta}$ might be a more appropriate form, possibly with $\beta = 1/3$ (this may be supported by results from plume theory; see e.g. (Morton et al. 1956)). Future research will include a calibration of the pyrogenic-potential model against a coupled atmosphere-fire model, with particular attention to the relationship between ν and I. The work in Section 5.5 is a preliminary step in that direction.

7.2.2 Modelling ember transport

The research presented in this thesis improved our understanding of the modelling of ember transport by showing that the use of the terminal-velocity assumption overestimates the modelled density of embers travelling medium to long distances in turbulent plumes. This has important implications for the stochastic modelling of spot-fire development.

The modelling of ember transport was carried out by the post-processing of a wind field obtained from a large eddy model. Future work could include the incorporation of a spot-fire sub-model into a coupled atmosphere-fire model, either by explicitly modelling ember release and transport, or by some form of parametrisation of ember-landing distributions. The former is very computationally intensive, and the latter would be highly dependent on atmospheric and fire conditions. A combination of the two approaches might work well; the transport of a few representative embers could be modelled explicitly, and a parametrisation used to convert the results of this into a full ember-landing distribution. Another direction for future work is an analysis of the sensitivity of the results of Chapter 6 to the resolution of the model, since velocity gradients close to the fire may not be well captured by a horizontal resolution of 50 metres.

7.2.3 Concluding remarks

Large, plume-driven fires are among the most unpredictable and destructive natural hazards that we face. There is some evidence that, at least in Australia, they are becoming more common (Sharples et al. 2016b). Dynamic fire behaviour and intense spot-fire development both play an important role in the occurence of many such fires, and it is important to understand these processes, and how to model them. The research presented in this thesis represents a part in the forming of this understanding.

Bibliography

Albini, F. A. (1976). *Estimating Wildfire Behavior and Effects*. General Technical Report INT-30. Ogden, Utah: US Department of Agriculture Forest Service, Intermountain Forest and Range Experiment Station.

— (1979). *Spot Fire Distance from Burning Trees - a Predictive Model*. General Technical Report INT-56. Ogden, Utah: US Department of Agriculture Forest Service, Intermountain Forest and Range Experiment Station.

— (1981a). "A Model for the Wind-Blown Flame from a Line Fire". *Combustion and Flame* 43, pp. 155–174.

— (1981b). *Spot Fire Distance from Isolated Sources - Extensions of a Predictive Model*. Research Note INT-309. Ogden, Utah: US Department of Agriculture Forest Service, Intermountain Forest and Range Experiment Station.

— (1982). "Response of Free-Burning Fires to Nonsteady Wind". *Combustion Science and Technology* 29.3-6, pp. 225–241.

— (1983a). *Potential Spotting Distance from Wind-Driven Surface Fires*. Research Paper INT-309. Ogden, Utah: US Department of Agriculture Forest Service, Intermountain Research Station.

— (1983b). "The Variability of Wind-Aided Free-Burning Fires". *Combustion science and technology* 31.5-6, pp. 303–311.

— (1983c). "Transport of Firebrands by Line Thermals". *Combustion Science and Technology* 32.5-6, pp. 277–288.

Anderson, H. E. (1982). *Aids to Determining Fuel Models For Estimating Fire Behavior*. General Technical Report INT-122. Ogden, Utah: US Department of Agriculture Forest Service, Intermountain Research Station.

Anthenien, R. A., S. D. Tse, and A. Carlos Fernandez-Pello (2006). "On the Trajectories of Embers Initially Elevated or Lofted by Small Scale Ground Fire Plumes in High Winds". *Fire Safety Journal* 41.5, pp. 349–363.

Arnold, R. K. and C. C. Buck (1954). "Blow-Up Fires—Silviculture or Weather Problems?" *Journal of Forestry* 52.6, pp. 408–411.

Badlan, R. L., J. J. Sharples, J. P. Evans, and R. H. D. McRae (2017). "The Role of Deep Flaming in Violent Pyroconvection". In: *MODSIM17, 22nd International Congress on Modelling and Simulation*. Ed. by G. Syme, D. Hatton MacDonald, B. Fulton, and J. Piantadosi. Hobart, Tasmania, Australia: The Modelling and Simulation Society of Australia and New Zealand Inc., pp. 1090–1096.

Batchelor, G. K. (1967). *An Introduction to Fluid Dynamics*. Cambridge University Press.

Baum, H. R. and B. J. McCaffrey (1989). "Fire Induced Flow Field–Theory and Experiment". In: *Fire Safety Science–Proceedings of the Second International Symposium*. Tokyo, Japan: Hemisphere Publishing Corporation, pp. 129–148.

Bejan, A., S. Ziaei, and S. Lorente (2014). "Evolution: Why All Plumes and Jets Evolve to Round Cross Sections". *Scientific Reports* 4, p. 4730.

Byram, G. (1959). "Combustion of Forest Fuels". In: *Forest Fire: Control and Use*. Ed. by K. P. Davis. 1st ed. New York: McGraw-Hill: New York, pp. 61–89.

Canfield, J. M., R. R. Linn, J. A. Sauer, M. Finney, and J. Forthofer (2014). "A Numerical Investigation of the Interplay between Fireline Length, Geometry, and Rate of Spread". *Agricultural and Forest Meteorology* 189–190, pp. 48–59.

Cetegen, B. M. and T. A. Ahmed (1993). "Experiments on the Periodic Instability of Buoyant Plumes and Pool Fires". *Combustion and Flame* 93.1, pp. 157–184.

Cheney, N. and G. Bary (1969). "The Propagation of Mass Conflagrations in a Standing Eucalypt Forest by the Spotting Process". In: *Mass Fire Symposium*. Defense Standards Laboratory Melbourne, pp. 10–12.

Clark, T. L., M. J. Reeder, M. Griffiths, D. Packham, and N. Krusel (2005). "Infrared Observations and Numerical Modelling of Grassland Fires in the Northern Territory, Australia". *Meteorology and Atmospheric Physics* 88.3-4, pp. 193–201.

Clark, T. L., M. A. Jenkins, J. L. Coen, and D. R. Packham (1996a). "A Coupled Atmosphere-Fire Model: Role of the Convective Froude Number and Dynamic Fingering at the Fireline". *International Journal of Wildland Fire* 6.4, pp. 177–190.

Clark, T. L., M. A. Jenkins, J. Coen, and D. Packham (1996b). "A Coupled Atmospher-Fire Model: Convective Feedback on Fire-Line Dynamics". *Journal of Applied Meteorology* 35.6, pp. 875–901.

Clark, T. L., L. Radke, J. Coen, and D. Middleton (1999). "Analysis of Small-Scale Convective Dynamics in a Crown Fire Using Infrared Video Camera Imagery". *Journal of Applied Meteorology* 38.10, pp. 1401–1420.

Coen, J. L. (2013). *Modeling Wildland Fires: A Description of the Coupled AtmosphereWildland Fire Environment Model (CAWFE)*. NCAR Technical Notes TN-500. Boulder, Colorado, USA: National Centre for Atmospheric Research.

Coen, J. L., M. Cameron, J. Michalakes, E. G. Patton, P. J. Riggan, and K. M. Yedinak (2013). "WRF-Fire: Coupled Weather–Wildland Fire Modeling with the Weather Research and Forecasting Model". *Journal of Applied Meteorology and Climatology* 52.1, pp. 16–38.

Countryman, C. M. (1964). *Mass Fires and Fire Behavior*. US Forest Service Research Paper PSW-19. Berkeley, California: US Department of Agriculture Forest Service, Forest and Range Experiment Station.

Crossland, B. (1992). "The King's Cross Underground Fire and the Setting up of the Investigation". *Fire Safety Journal*. Special Issue: The King's Cross Underground Fire 18.1, pp. 3–11.

Cruz, M. G., J. S. Gould, S. Kidnie, R. Bessell, D. Nichols, and A. Slijepcevic (2015). "Effects of Curing on Grassfires: II. Effect of Grass Senescence on the Rate of Fire Spread". *International Journal of Wildland Fire* 24.6, pp. 838–848.

Deardorff, J. (1980). "Stratocumulus-Capped Mixed Layers Derived from a Three-Dimensional Model". English. *Boundary-Layer Meteorology* 18.4, pp. 495–527.

Dold, J. W. (2010). "Flow Attachment in Eruptive Fire Growth". In: *Proceedings of the 6th International Conference on Forest Fire Research*. Coimbra, Portugal.

Dold, J. W. and A. Zinoviev (2009). "Fire Eruption through Intensity and Spread Rate Interaction Mediated by Flow Attachment". *Combustion Theory and Modelling* 13.5, pp. 763–793.

Doogan, M. (2006). *The Canberra Firestorm: Inquests into Four Deaths and Four Fires between 8 and 18 January*. Coroners Report. Canberra, Australia: ACT Coroners Court.

Dupuy, J.-L., R. R. Linn, V. Konovalov, F. Pimont, J. A. Vega, and E. Jiménez (2011). "Exploring Three-Dimensional Coupled Fire–Atmosphere Interactions Downwind of Wind-Driven Surface Fires and Their Influence on Backfires Using the HIGRAD-FIRETEC Model". *International Journal of Wildland Fire* 20.6, pp. 734–750.

Edgar, R., J. Sharples, and H. Sidhu (2015). "Revisiting the King's Cross Underground Disaster with Implications for Modelling Wildfire Eruption". In: *MODSIM15, 21st International Congress on Modelling and Simulation*. Gold Coast, Queensland, Australia: The Modelling and Simulation Society of Australia and New Zealand Inc., pp. 215–221.

Edgar, R. A., J. J. Sharples, and H. S. Sidhu (2016). "Examining the Effects of Convective Intensity on Plume Attachment in Threedimensional Trenches". In:

Chemeca 2016: Chemical Engineering - Regeneration, Recovery and Reinvention. Melbourne, Victoria, Australia: Engineers Australia, pp. 613–621.

Ellis, P. F. M. (2010). "The Effect of the Aerodynamic Behaviour of Flakes of Jarrah and Karri Bark on Their Potential as Firebrands". *Journal of the Royal Society of Western Australia* 93, pp. 21–27.

Fendell, F. E. and M. F. Wolff (2001). "Wind-Aided Fire Spread". In: *Forest Fires*. Ed. by E. A. Johnson and K. Miyanishi. Academic Press, pp. 171–223.

Filippi, J. B., F. Bosseur, C. Mari, C. Lac, P. Le Moigne, B. Cuenot, D. Veynante, D. Cariolle, and J.-H. Balbi (2009). "Coupled Atmosphere-Wildland Fire Modelling". *Journal of Advances in Modeling Earth Systems* 1.4.

Finney, M. A., J. D. Cohen, J. M. Forthofer, S. S. McAllister, M. J. Gollner, D. J. Gorham, K. Saito, N. K. Akafuah, B. A. Adam, and J. D. English (2015). "Role of Buoyant Flame Dynamics in Wildfire Spread". *Proceedings of the National Academy of Sciences* 112.32, pp. 9833–9838.

Finney, M. A. and S. S. McAllister (2011). "A Review of Fire Interactions and Mass Fires". *Journal of Combustion* 2011.Article ID 548328, pp. 14–14.

Finney, M. A. (2004). *FARSITE: Fire Area Simulator: Model Development and Evaluation*. Research Paper RMRS-RP-4 Revised. Ogden, Utah: US Department of Agriculture Forest Service, Rocky Mountain Research Station.

Frandsen, W. H. (1971). "Fire Spread through Porous Fuels from the Conservation of Energy". *Combustion and Flame* 16.1, pp. 9–16.

Hilton, J. E., C. Miller, J. J. Sharples, and A. L. Sullivan (2016). "Curvature Effects in the Dynamic Propagation of Wildfires". *International Journal of Wildland Fire* 25.12, pp. 1238–1251.

Hilton, J. E., J. J. Sharples, A. L. Sullivan, and W. Swedosh (2017). "Simulation of Spot fire Coalescence with Dynamic Feedback". In: *MODSIM17, 22nd International Congress on Modelling and Simulation*. Hobart, Tasmania, Australia: The

Modelling and Simulation Society of Australia and New Zealand Inc., pp. 1111–1117.

Hilton, J. E., A. L. Sullivan, W. Swedosh, J. Sharples, and C. Thomas (2018). "Incorporating Convective Feedback in Wildfire Simulations Using Pyrogenic Potential". *Environmental Modelling & Software* 107, pp. 12–24.

Himoto, K. and T. Tanaka (2005). "Transport of Disk-Shaped Firebrands in a Turbulent Boundary Layer". In: *Proceedings of the Eighth International Symposium on Fire Safety Science*. Ed. by D. T. Gottuk and B. Y. Latimer. International Association for Fire Safety Science.

Jenkins, M. A., T. Clark, and J. Coen (2001). "Coupling Atmospheric and Fire Models". In: *Forest Fires*. Ed. by E. A. Johnson and K. Miyanishi. Academic Press.

Jiménez, P. A., D. Muñoz-Esparza, and B. Kosović (2018). "A High Resolution Coupled Fire–Atmosphere Forecasting System to Minimize the Impacts of Wildland Fires: Applications to the Chimney Tops II Wildland Event". en. *Atmosphere* 9.5, p. 197.

Johansen, R. W. (1984). *Prescribed Burning with Spot Fires in the Georgia Coastal Plain [Pinus Elliottii, Sabal Etonia, Ilex Glabra].* Georgia Forest Research Paper 49. Georgia Forestry Commission.

Kepert, J. D., M. Peace, and H. Ye (2017). *Coupled Fire-Atmosphere Modelling Project*. Annual Project Report 2017. Melbourne: Bushfire and Natural Hazards CRC.

Koo, E., R. R. Linn, P. J. Pagni, and C. B. Edminster (2012). "Modelling Firebrand Transport in Wildfires Using HIGRAD/FIRETEC". *International Journal of Wildland Fire* 21.4, pp. 396–417.

Koo, E., P. J. Pagni, D. R. Weise, and J. P. Woycheese (2010). "Firebrands and Spotting Ignition in Large-Scale Fires". *International Journal of Wildland Fire* 19.7, pp. 818–843.

Lahaye, S., J. Sharples, S. Matthews, S. Heemstra, O. Price, and R. Badlan (2018). "How Do Weather and Terrain Contribute to Firefighter Entrapments in Australia?" *International Journal of Wildland Fire* 27.2, pp. 85–98.

Lee, S.-L. and J. M. Hellman (1969). "Study of Firebrand Trajectories in a Turbulent Swirling Natural Convection Plume". *Combustion and Flame* 13.6, pp. 645–655.

Lee, S.-l. and J. M. Hellman (1970). "Firebrand Trajectory Study Using an Empirical Velocity-Dependent Burning Law". *Combustion and Flame* 15.3, pp. 265–274.

Lin, J. C., D. Brunner, and C. Gerbig (2011). "Studying Atmospheric Transport through Lagrangian Models". *EOS, Transactions American Geophysical Union* 92.21, pp. 177–178.

Linn, R. R. (1997). *A Transport Model for Prediction of Wildfire Behavior*. Thesis LA–13334-T. Los Alamos, New Mexico: Los Alamos National Laboratory.

Linn, R., J. Reisner, J. J. Colman, and J. Winterkamp (2002). "Studying Wildfire Behavior Using FIRETEC". *International Journal of Wildland Fire* 11.4, pp. 233–246.

Mandel, J., S. Amram, J. D. Beezley, G. Kelman, A. K. Kochanski, V. Y. Kondratenko, B. H. Lynn, B. Regev, and M. Vejmelka (2014). "Recent Advances and Applications of WRF–SFIRE". *Natural Hazards and Earth System Science* 14.10, pp. 2829–2845.

Mandel, J., J. D. Beezley, and A. K. Kochanski (2011). "Coupled Atmosphere-Wildland Fire Modeling with WRF 3.3 and SFIRE 2011". *Geoscientific Model Development* 4.3, pp. 591–610.

Marsden, J. E. and A. Tromba (2003). *Vector Calculus*. Macmillan.

McArthur, A. G. (1966). *Weather and Grassland Fire Behaviour*. Leaflet No. 100. Forestry and Timber Bureau, Department of National Development, Commonwealth of Australia.

McArthur, A. G. (1967). *Fire Behaviour in Eucalypt Forests*. Leaflet No. 107. Forest Research Institute, Department of National Development, Commonwealth of Australia.

McRae, D. J., J.-Z. Jin, S. G. Conard, A. I. Sukhinin, G. A. Ivanova, and T. W. Blake (2005). "Infrared Characterization of Fine-Scale Variability in Behavior of Boreal Forest Fires". *Canadian Journal of Forest Research* 35.9, pp. 2194–2206.

McRae, D., B. Stocks, C. Ogilvie, et al. (1989). "Fire Acceleration on Large-Scale Convection Burns". In: *Proceedings of the 10th Conference on Fire and Forest Meteorology*. Ottawa, Ontario, Canada, pp. 101–107.

McRae, R. H. D., J. J. Sharples, and M. Fromm (2015). "Linking Local Wildfire Dynamics to pyroCb Development". *Nat. Hazards Earth Syst. Sci.* 15.3, pp. 417–428.

McRae, R. H. D., J. J. Sharples, S. R. Wilkes, and A. Walker (2013). "An Australian Pyro-Tornadogenesis Event". *Natural Hazards* 65.3, pp. 1801–1811.

McRae, R. and J. Sharples (2011). "A Conceptual Framework for Assessing the Risk Posed by Extreme Bushfires". *Australian Journal of Emergency Management* 26.2, p. 47.

Mell, W., M. A. Jenkins, J. Gould, and P. Cheney (2007). "A Physics-Based Approach to Modelling Grassland Fires". *International Journal of Wildland Fire* 16.1, pp. 1–22.

Miller, C., J. Hilton, A. Sullivan, and M. Prakash (2015). "SPARK – A Bushfire Spread Prediction Tool". In: *Environmental Software Systems. Infrastructures, Services and Applications*. Ed. by R. Denzer, R. M. Argent, G. Schimak, and J. Ȟrebíˇcek. Cham: Springer International Publishing, pp. 262–271.

Moeng, C.-H. and P. P. Sullivan (1994). "A Comparison of Shear- and Buoyancy-Driven Planetary Boundary Layer Flows". *Journal of the Atmospheric Sciences* 51.7, pp. 999–1022.

Morton, B., G. I. Taylor, and J. S. Turner (1956). "Turbulent Gravitational Convection from Maintained and Instantaneous Sources". *Proc. R. Soc. Lond. A* 234.1196, pp. 1–23.

Morvan, D., S. Méradji, and G. Accary (2009). "Physical Modelling of Fire Spread in Grasslands". *Fire Safety Journal* 44.1, pp. 50–61.

Morvan, D., C. Hoffman, F. Rego, and W. Mell (2011). "Numerical Simulation of the Interaction between Two Fire Fronts in Grassland and Shrubland". *Fire Safety Journal* 46.8, pp. 469–479.

Muraszew, A. (1974). *Firebrand Phenomena*. Aerospace Report ATR-74(8165-01)-1. El Segundo, California: The Aerospace Corporation.

Muraszew, A., J. Fedele, and W. Kuby (1975). *Firebrand Investigation*. Aerospace Report ATR-75(7470)-1. El Segundo, California: The Aerospace Corporation.

Noble, I. R., G. A. V. Bary, and A. M. Gill (1980). "McArthur's Fire-Danger Meters Expressed as Equations". *Australian Journal of Ecology* 5, pp. 201–203.

Oliveira, L. A., A. G. Lopes, B. R. Baliga, M. Almeida, and D. X. Viegas (2014). "Numerical Prediction of Size, Mass, Temperature and Trajectory of Cylindrical Wind-Driven Firebrands". *International Journal of Wildland Fire* 23.5, pp. 698–708.

Pierce, D. (2017). *Ncdf4: Interface to Unidata netCDF (Version 4 or Earlier) Format Data Files*. R package version 1.16.

R Core Team (2017). *R: A Language and Environment for Statistical Computing*. Vienna, Austria.

Raposo, J. R., S. Cabiddu, D. X. Viegas, M. Salis, and J. Sharples (2015). "Experimental Analysis of Fire Spread across a Two-Dimensional Ridge under Wind Conditions". en. *International Journal of Wildland Fire* 24.7, pp. 1008–1022.

Raposo, J. R., D. X. Viegas, X. Xie, M. Almeida, A. R. Figueiredo, L. Porto, and J. Sharples (2018). "Analysis of the Physical Processes Associated with Junction

Fires at Laboratory and Field Scales". *International Journal of Wildland Fire* 27.1, pp. 52–68.

Rothermel, R. (1991). *Predicting Behavior and Size of Crown Fires in the Northern Rocky Mountains*. Research Paper INT-438. Ogden, Utah: US Department of Agriculture Forest Service, Intermountain Research Station.

Rothermel, R. C. (1972). *A Mathematical Model for Predicting Fire Spread in Wildland Fuels*. Research Paper Research Paper INT-115. Ogden, Utah: US Department of Agriculture Forest Service.

Sardoy, N., J. L. Consalvi, A. Kaiss, A. C. Fernandez-Pello, and B. Porterie (2008). "Numerical Study of Ground-Level Distribution of Firebrands Generated by Line Fires". *Combustion and Flame* 154.3, pp. 478–488.

Sardoy, N., J.-L. Consalvi, B. Porterie, and A. C. Fernandez-Pello (2007). "Modeling Transport and Combustion of Firebrands from Burning Trees". *Combustion and Flame* 150.3, pp. 151–169.

Sethian, J. A. (1999). *Level Set Methods and Fast Marching Methods: Evolving Interfaces in Computational Geometry, Fluid Mechanics, Compute Vision, and Materials Science*. 2nd ed. New York: Cambridge University Press.

Sharples, J. J. and J. E. Hilton (2017). "Modelling the Dynamic Behaviour of Small Scale Junction Fires Using Curvature Flows". In: *MODSIM2017, 22nd International Congress on Modelling and Simulation*. Ed. by G. Syme, D. Hatton MacDonald, B. Fulton, and J. Piantadosi. Hobart, Tasmania, Australia: The Modelling and Simulation Society of Australia and New Zealand Inc., pp. 1166–1172.

Sharples, J. J., J. E. Hilton, and A. L. Sullivan (2016a). *Fire Coalescence and Mass Spot Fire Dynamics: Experimentation, Modelling and Simulation.* Annual Project Report 2015-2016. Melbourne, Victoria, Australia: Bushfire and Natural Hazards Cooperative Research Centre.

Sharples, J. J., I. N. Towers, G. Wheeler, V.-M. Wheeler, and McCoy (2013). "Modelling Fire Line Merging Using Plane Curvature Flow". In: *MODSIM2013, 20th International Congress on Modelling and Simulation*. Ed. by J. Piantadosi, R. S. Anderssen, and J. Boland. Adelaide, Australia, pp. 256–262.

Sharples, J. J., G. J. Cary, P. Fox-Hughes, S. Mooney, J. P. Evans, M.-S. Fletcher, M. Fromm, P. F. Grierson, R. McRae, and P. Baker (2016b). "Natural Hazards in Australia: Extreme Bushfire". en. *Climatic Change* 139.1, pp. 85–99.

Sharples, J. J., A. M. Gill, and J. W. Dold (2010a). "The Trench Effect and Eruptive Wildfires: Lessons from the King's Cross Underground Disaster". In: *Proceedings of Australian Fire and Emergency Service Authorities Council 2010 Conference*, pp. 8–10.

Sharples, J. J., R. H. D. McRae, and S. R. Wilkes (2012). "Wind-Terrain Effects on the Propagation of Wildfires in Rugged Terrain: Fire Channelling". *International Journal of Wildland Fire* 21.3, pp. 282–296.

Sharples, J. J., D. X. Viegas, C. G. Rossa, and R. H. McRae (2010b). "Small-Scale Observations of Atypical Fire Spread Caused by the Interaction of Wind, Terrain and Fire". In: *Proceedings of the VI International Conference on Forest Fire Research*. Coimbra, Portugal, pp. 15–18.

Sharples, J., A. Kiss, J. Raposo, D. Viegas, and C. Simpson (2015). "Pyrogenic Vorticity from Windward and Lee Slope Fires". In: *MODSIM15, 21st International Congress on Modelling and Simulation*. Gold Coast, Queensland, Australia: Model. Simul. Soc. Aust. NZ Canberra, Aust., pp. 291–97.

Simpson, C. C., J. J. Sharples, J. P. Evans, and M. F. McCabe (2013). "Large Eddy Simulation of Atypical Wildland Fire Spread on Leeward Slopes". *International Journal of Wildland Fire* 22.5, pp. 599–614.

Skamarock, W. C., J. B. Klemp, J. Dudhia, D. O. Gill, D. M. Barker, M. Duda, X. Y. Huang, W. Wang, and J. G. Powers (2008). *A Description of the Advanced*

Research WRF Version 3. NCAR Technical Note NCAR/TN–475+STR. Boulder, Colorado, USA: National Centre for Atmospheric Research.

Sullivan, A. L. (2009a). "Wildland Surface Fire Spread Modelling, 1990–2007. 1: Physical and Quasi-Physical Models". *International Journal of Wildland Fire* 18.4, pp. 349–368.

— (2009b). "Wildland Surface Fire Spread Modelling, 1990–2007. 2: Empirical and Quasi-Empirical Models". *International Journal of Wildland Fire* 18.4, pp. 369–386.

— (2009c). "Wildland Surface Fire Spread Modelling, 1990–2007. 3: Simulation and Mathematical Analogue Models". *International Journal of Wildland Fire* 18.4, pp. 387–403.

Tarifa, C. S. and P. P. del Notario (1962). *Open Fires and Transport of Firebrands*. Tech. rep. Madrid: Instituto Nacional de Tecnica Aeronautica "Esteban Terradas".

Tarifa, C. S., P. P. del Notario, and F. G. Moreno (1965a). "On the Flight Paths and Lifetimes of Burning Particles of Wood". In: *Tenth Symposium (International) on Combustion*. The Combustion Institute, pp. 1021–1037.

Tarifa, C. S., P. P. del Notario, F. G. Moreno, A. L. Martinez, and A. B. Sanchez (1963). *Open Fires and Transport of Firebrands*. Tech. rep. Madrid, Spain: Instituto Nacional de Tecnica Aeronautica "Esteban Terradas".

— (1964). *Open Fires and Transport of Firebrands*. Tech. rep. Madrid, Spain: Instituto Nacional de Tecnica Aerospacial "Esteban Terradas".

Tarifa, C. S., P. P. del Notario, F. G. Moreno, and A. R. Villa (1967). *Transport and Combustion of Firebrands*. Tech. rep. Madrid, Spain: Instituto Nacional de Tecnica Aerospacial "Esteban Terradas".

Tarifa, C. S., P. P. del Notario, A. R. Villa, A. L. Martinez, and E. Mezquida (1966). *Open Fires and Transport of Firebrands*. Tech. rep. Madrid, Spain: Instituto Nacional de Tecnica Aerospacial "Esteban Terradas".

Tarifa, C. S., P. P. del Notario, A. R. Villa, A. L. Martinez, and M. O. Perez (1965b). *Open Fires and Transport of Firebrands*. Tech. rep. Instituto Nacional de Tecnica Aerospacial "Esteban Terradas".

Thomas, C. M., J. J. Sharples, and J. P. Evans (2015). "Pyroconvective Interaction of Two Merged Fire Lines: Curvature Effects and Dynamic Fire Spread". In: *MODSIM2015, 21st International Congress on Modelling and Simulation*. Ed. by T. Weber, M. J. McPhee, and R. S. Anderssen. Gold Coast, Queensland, Australia: The Modelling and Simulation Society of Australia and New Zealand Inc., pp. 312–318.

— (2017a). "Evaluating the Terminal-Velocity Assumption in Simulations of Long-Range Ember Transport". In: *MODSIM2017, 22nd International Congress on Modelling and Simulation*. Ed. by G. Syme, D. Hatton MacDonald, B. Fulton, and J. Piantadosi. Hobart, Tasmania, Australia: The Modelling and Simulation Society of Australia and New Zealand Inc., pp. 1187–1193.

— (2017b). "Modelling the Dynamic Behaviour of Junction Fires with a Coupled Atmosphere–Fire Model". *International Journal of Wildland Fire* 26.4, pp. 331–344.

Thurston, W., K. J. Tory, R. J. B. Fawcett, and J. D. Kepert (2013). "Large-Eddy Simulations of Bushfire Plumes in the Turbulent Atmospheric Boundary Layer". In: *MODSIM2013, 20th International Congress on Modelling and Simulation*. Ed. by J. Piantadosi, R. S. Anderssen, and J. Boland. Modelling and Simulation Society of Australia and New Zealand, pp. 284–289.

Thurston, W., J. D. Kepert, K. J. Tory, and R. J. B. Fawcett (2017). "The Contribution of Turbulent Plume Dynamics to Long-Range Spotting". *International Journal of Wildland Fire* 26.4, pp. 317–330.

Tolhurst, K. (2009). *Report on the Physical Nature of the Victorian Fires Occurring on 7th February 2009*. Tech. rep. Creswick, Victoria: The University of Melbourne.

Tolhurst, K., B. Shields, D. Chong, et al. (2008). "Phoenix: Development and Application of a Bushfire Risk Management Tool". *Australian Journal of Emergency Management* 23.4, p. 47.

Tse, S. D. and A. Fernandez-Pello (1998). "On the Flight Paths of Metal Particles and Embers Generated by Power Lines in High Winds - a Potential Source of Wildland Fires". *Fire Safety Journal* 30, pp. 333–356.

Viegas, D. X. (2006). "Parametric Study of an Eruptive Fire Behaviour Model". *International Journal of Wildland Fire* 15.2, pp. 169–177.

Viegas, D. X., L. P. Pita, L. Ribeiro, and P. Palheiro (2005). "Eruptive Fire Behaviour in Past Fatal Accidents". In: *Eighth International Wildland Firefighter Safety Summit*. Ed. by B. W. Butler and M. E. Alexander. Missoula, MT: The International Association of Wildland Fire.

Viegas, D. X. and A. Simeoni (2011). "Eruptive Behaviour of Forest Fires". *Fire Technology* 47.2, pp. 303–320.

Viegas, D. X., J. R. Raposo, D. A. Davim, and C. G. Rossa (2012). "Study of the Jump Fire Produced by the Interaction of Two Oblique Fire Fronts. Part 1. Analytical Model and Validation with No-Slope Laboratory Experiments". *International Journal of Wildland Fire* 21, pp. 843–856.

Viegas, D. X. (2005). "A Mathematical Model For Forest Fires Blowup". *Combustion Science and Technology* 177.1, pp. 27–51.

Viegas, D. (2004). "On the Existence of a Steady State Regime for Slope and Wind Driven Fires". *International Journal of Wildland Fire* 13.1, pp. 101–117.

Wade, D. D. and D. E. Ward (1973). *An Analysis of the Air Force Bomb Range Fire*. Research Paper SE-105. Asheville, North Carolina: US Department of Agriculture Forest Service, Southeastern Forest Experiment Station.

Weber, R. O. (1989). "Analytical Models for Fire Spread Due to Radiation". *Combustion and Flame* 78, pp. 398–408.

Weihs, D. and R. D. Small (1986). *Interactions and Spreading of Adjacent Large Area Fires*. Technical Report DNA-TR-86-214. Los Angeles, CA: Pacific-Sierra Research Corp.

Weil, J. C., P. P. Sullivan, and C.-H. Moeng (2004). "The Use of Large-Eddy Simulations in Lagrangian Particle Dispersion Models". *Journal of the Atmospheric Sciences* 61.23, pp. 2877–2887.

Wheeler, V.-M., J. A. McCoy, G. E. Wheeler, and J. J. Sharples (2013). "Curvature Flows and Barriers in Fire Front Modelling". In: *MODSIM2013, 20th International Congress on Modelling and Simulation*. Ed. by J. Piantadosi, R. S. Anderssen, and J. Boland. Adelaide, Australia: The Modelling and Simulation Society of Australia and New Zealand Inc., pp. 297–303.

Wickham, H. (2009). *Ggplot2: Elegant Graphics for Data Analysis*. Springer-Verlag New York.

Wieringa, J. (1992). "Updating the Davenport Roughness Classification". *Journal of Wind Engineering and Industrial Aerodynamics* 41.1, pp. 357–368.

Williams, F. A. (1965). *Combustion Theory: The Fundamental Theory of Chemical Reacting Flow Systems*. Addison-Wesley.

Woycheese, J. P., P. J. Pagni, and D. Liepmann (1998). "Brand Lofting above Large-Scale Fires". In: *Proceedings of Second International Conference of Fire Research and Engineering*. The Society of Fire Protection Engineers, pp. 137–150.

— (1999). "Brand Propagation from Large-Scale Fires". *Journal of Fire Protection Engineering* 10.2, pp. 32–44.